Enhanced Radiation Cooling

Design of an Active Thermal Protection System

Wouter Dubois

Technische Universiteit Delft

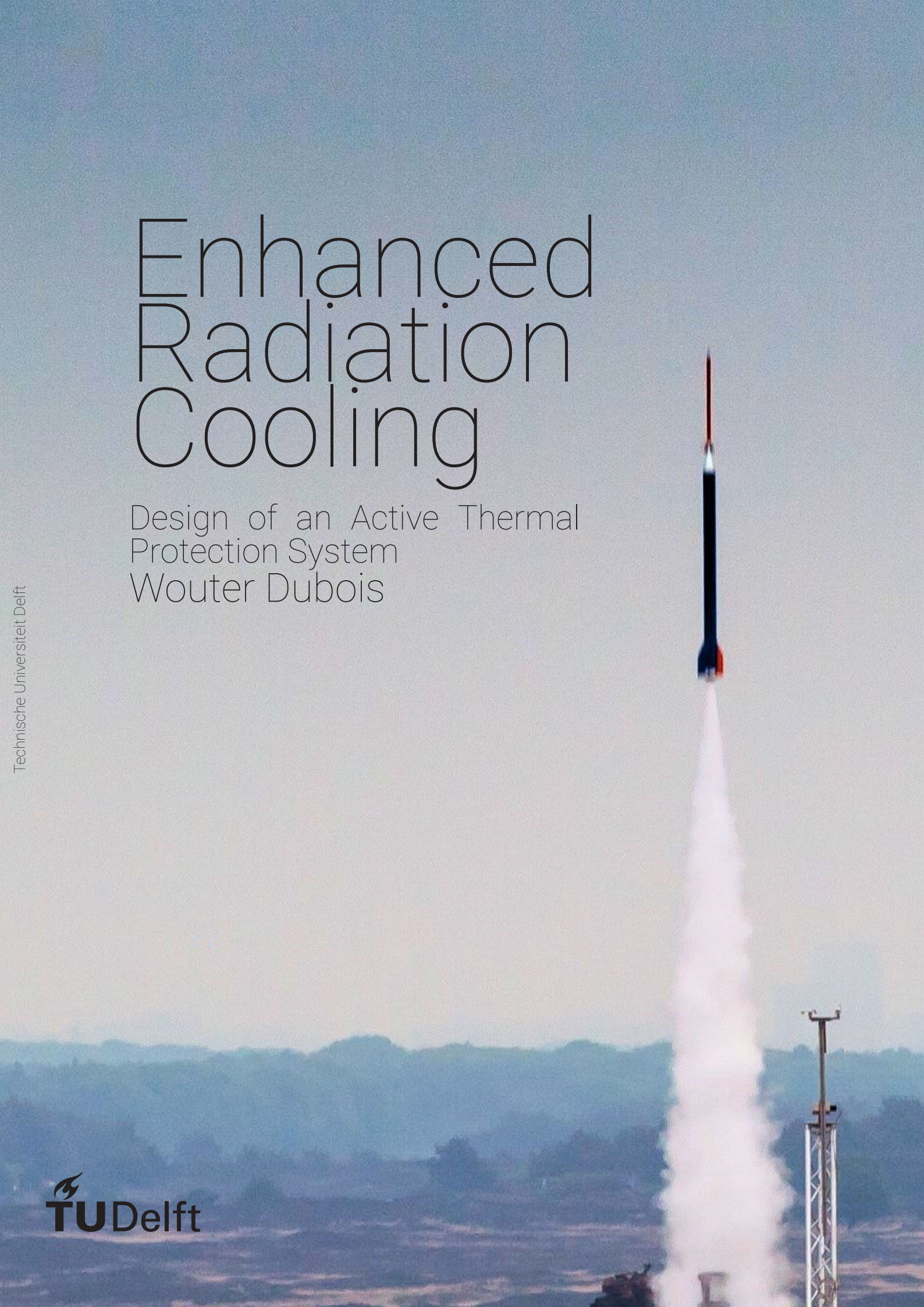

TU Delft

Enhanced Radiation Cooling

Design of an Active Thermal Protection System

by

Wouter Dubois

to obtain the degree of Master of Science
at Delft University of Technology,
to be defended publicly on Thursday December 21, 2017 at 13:00.

Student number:	1379429	
Project duration:	April 24, 2017 – December 21, 2017	
Thesis committee:	Dr. ir. E. Mooij,	TU Delft, supervisor
	Ir. K. J. Sudmeijer,	TU Delft, supervisor
	Prof. dr. ir. P. N. A. M. Visser,	TU Delft
	Dr. ir. F. F. J. Schrijer,	TU Delft

An electronic version of this thesis is available at `http://repository.tudelft.nl/`.

TU Delft

Preface

After a decade of studying, this is the final step in obtaining my masters degree in Aerospace Engineering. I would like to take this opportunity to thank my parents for allowing me to follow my own path during this time and providing me with continuous and seemingly unconditional support. I know at times it looked like it would be dragged on for still years to come, but their support and necessary pressure kept me on track. I cannot thank them enough, without them I would not be where I am at this moment.

A special thank goes to my supervisors at the TU Delft, Kees Sudmeijer and Erwin Mooij. Their support was more than I could wish for and helped me in successfully finishing this project. Kees, thank you for all the meetings (although we drifted more than once away from the research in our discussion) and your help. Erwin, thank you for your always useful input and feedback. A special thanks goes to Mark and Hein from T-Minus Engineering, without them this project would not have been the same. The availability of their rocket and time gave this project another dimension.

Lastly, I would like to thank all my friends. Without them I would probably finished earlier but the trip was worth it. 10 years feels like a lifetime and in a way it is. It has cost me blood, sweat and tears but this is finally the end. Tonight, we celebrate or like it is said in the beautiful West Flanders: loaten we 't zwien deur de bjèten joagen!

Wouter Dubois
Delft, December 2017

Abstract

Current-day space vehicle are equipped with a passive Thermal Protection System (TPS), but these systems operate at the edge of their capabilities. The research into the next generation reusable space vehicle demands the use of active TPS, these systems are not limited to the capabilities of the used material but depend on the active cooling mechanism. A system of cooled metallic TPS is developed at the TU Delft resulting in an increase in the maximum allowable thermal load for a given TPS temperature, this system is the enhanced radiation cooling TPS. The research question is: "Can an active thermal protection system improve the flying characteristics and the flight performance of a re-entry vehicle?". The first step in answering this question is to verify the process behind the active TPS. This thesis aims to design an experiment to verify this process.

To answer the research question two tools were developed: a flight simulator and a thermodynamic analyser. The flight simulator provides insight in the behaviour of the rocket and shows the consequences of implementing the enhanced radiation cooling TPS on the rocket. The thermodynamic analyser is used to estimate the wall temperature of the system and shows the effect of the sensitivity analysis of the design of the cooling subsystem. The enhanced radiation cooling system is designed to be mounted on the T-Minus Dart and an experiment to verify the impact of the active TPS is derived using the nominal mission of the rocket. Sensitivity analysis resulted in thin outer shell and a insulation sphere filled with the coolant. The outer shell needs to be as thin as possible in order to maximize the cooling effect. For an outer shell of 0.5 millimetres, the maximum allowable thermal load can be doubled in comparison with an non-cooled flight. If an identical thermal loading is assumed for two return vehicles, the active cooled vehicle can be designed with a nose radius of around 30 % smaller that the non-cooled vehicle. This will result in a vehicle with a higher lift-over-drag ratio, extending the return trajectory which increases the safety of the re-entry flight.

The validity of performing an enhanced radiation cooling experiment is shown by the use of the tools developed in this thesis. The incoming heat flux can be doubled while maintaining the same wall temperatures if the cooling system is applied. This opens the possibility of redesigning re-entry vehicles to achieve a high lift-to-drag ratio.

List of symbols

Roman

Symbol	Rationale	Unit
$\mathbf{a}$	acceleration	$m \cdot s^{-2}$
b	reference length	m
C	aerodynamic coefficient	-
$\mathbf{C}$	directional cosine matrix	-
C_p	pressure coefficient	$J \cdot kg^{-1} K^{-1}$
d	diameter	m
e	eccentricity	-
$\mathbf{F}$	force vector	N
g	gravitational acceleration	$m \cdot s^{-2}$
$\mathbf{h}$	angular momentum	$kg \cdot m^2 \cdot s^{-1}$
h	height	m
H	enthalpy	J
$\mathbf{H}$	angular momentum	$kg \cdot m^2 \cdot s^{-1}$
H_G	Greenwich hour angle	rad
H_{vap}	heat of vaporization	$KJ \cdot g^{-1}$
I	moment of inertia	$kg \cdot m^2$
k	coefficient of thermal conductivity	$W \cdot m^{-1} \cdot K^{-1}$
l	reference length	m
L	rolling moment	$N \cdot m$
m	mass	kg
$\dot{m}$	mass flow	$kg \cdot s^{-1}$
M	Mach number	-
M	pitching moment	$N \cdot m$
$\mathbf{M}$	torque	$N \cdot m$
N	yawing moment	$N \cdot m$
p	pressure	$N \cdot m^{-2}$
p	roll rate	$rad \cdot s^{-1}$
P_r	Prandtl number	-
q	pitch rate	$rad \cdot s^{-1}$
q	heat flux	$W \cdot m^{-2}$
$\bar{q}$	dynamic pressure	$N \cdot m^{-2}$
r	recovery factor	-
r	roll rate	$rad \cdot s^{-1}$
$\mathbf{r}$	position	m
$\mathbf{r_e}$	position vector for centre of mass flow	m
$\Re$	distance	
R	radius	m
s_m	local semi-span of vertical panel	m
s_d	Dynamic stability factor	-
s_g	Gyroscopic stability factor	-
S	surface	m^2
t	time	s
T	temperature	K
T	thrust	N
u	velocity in x direction in body-fixed reference frame	$m \cdot s^{-1}$
v	velocity in y direction in body-fixed reference frame	$m \cdot s^{-1}$
$\mathbf{V}$	velocity	$m \cdot s^{-1}$

w	velocity in z direction in body-fixed reference frame	$m \cdot s^{-1}$
x	position in x direction	m
y	position in y direction	m
z	position in z direction	m

Greek

Symbol	Rationale	Unit
α	angle of attack	rad
β	anlge of sideslip	rad
γ	ratio of specific heats	-
γ	flight path angle	rad
δ	fin cant angle	rad
δ	skin thickness	m
ε	emissivity coefficient	-
θ	pitch angle	rad
ρ	density	$kg \cdot m^{-3}$
λ	elevation	rad
λ	geographic latitude	rad
μ	dynamic viscosity	$kg \cdot m^{-1} \cdot s^{-1}$
μ	geocentric longitude	rad
ξ	complex angle of attack	rad
υ	kinematic viscosity	$kg \cdot m^{-1} \cdot s^{-1}$
φ	roll angle	rad
ϕ	body angle	rad
ψ	yaw angle	rad
ω	angular rate	$rad \cdot s^{-1}$

Indices

Symbol	Rationale
0	at zero (altitude, time, etc.)
1	conditions upstream of the normal shock wave
2	conditions downstream of the normal shock wave
A	axial
cm	with respect to the centre of mass
e	edge conditions
e	Earth
i	insulation conditions
l	rolling moment
L	left-hand side
m	pitching moment
n	yawing moment
N	normal
p	at point p
ref	reference
R	right hand
s	spheroid
st	stagnation point conditions
tower	launch tower
T	Total
S	sideforce
w	wall conditions
x	in x direction / around x axis
y	in y direction / around y axis
z	in z direction / around z axis

$]_t$	time rate of change
$\dot{(\,)}$	d( )/dt
$\tilde{(\,)}$	non-spinning aero-ballistic version of ( )

Reference frames

Symbol	Rationale
XYZ	inertial reference frame
$X_gY_gZ_g$	rotating geocentric reference frame
$X_vY_vZ_v$	vehicle-centred horizontal reference frame
$X_bY_bZ_b$	body-fixed reference frame

Constants

Parameter	Rationale	Value
e	eccentricity Earth	0.081818 [-]
g_0	standard gravitational acceleration Earth	9.80665 m $\cdot s^{-2}$
GM_e	standard gravitational parameter Earth	$3.98600441 \cdot 10^{14}$ $m^3 \cdot s^{-2}$
R_e	radius Earth	6378.136 km
ω_{cb}	rotational velocity Earth	$7.29220 \cdot 10^{-5}$ rad$\cdot s^{-1}$
σ	Stefan-Boltzmann constant	$5.670367 \cdot 10^{-8}$ W $\cdot$ m^{-2} $\cdot$ K^{-4}

Acronyms

AKTiV	Aktive Kühlung durch Transpiration im Versuch
BOR-4	Bespilotnyi Orbital'nyi Raketoplan 4
C/C-SiC	Carbon Fibre Reinforced Silicon Carbide Composites
DOF	Degrees Of Freedom
EXPERT	European eXPErimental Re-entry Testbed
GPS	Global Positioning System
IMU	Inertial Measurement Unit
KISS	Keep It Simple, Stupid
L/D	Lift-to-Drag ratio
NASP	National Aero-Space Plane
RKDP	Runge-Kutta Dormand-Prince method
TBD	To Be Determined
SHEFEX	Sharp Edge Flight Experiment
TPS	Thermal Protection System
VS	Veículo de Sondagem

Contents

1 Introduction

Ever since mankind first looked upon the stars, they were driven by the desire to explore and study the unknown. The first man-made object in space, the Bumper-WAC[1], opened the door to space exploration and research. In the late fifties and sixties, major milestones were achieved: the first satellite, Sputnik I, the first man in space, Yuri Gagarin and the first man on the Moon, Neil Armstrong. Over time, new technologies were developed to push the limits of space exploration and research even further, however one of the major constraints (among others) is the thermal loading. The ascent and descent phase of a space vehicle is subjected to large heat loads, this is due to the fact that the vehicle travels at high velocity in the atmosphere resulting in a large drag force which leads to an increase in the thermal loading. The longer the vehicle is subjected to this force, the higher the thermal loading will be. A Thermal Protection System (TPS) needs to be applied to protect the vehicle for the thermal loading. The TPS is vital component of the vehicle design: under-designing the system will results in failure during flight, over-designing will result in an increase in mass and cost and will have a negative impact on the feasibility of the design.

This chapter provides background on TPSs in Section 1.1. From this, the research goals are derived in Section 1.2 and lastly, the outline of the thesis is shown in Section 1.3.

1.1. Background

The design of a TPS is constrained to the mission and geometry of the vehicle, but each system must be able to withstand the thermal loading acting on the vehicle and meet the structural requirements. The main function of a TPS is to withstand the heat load and protect the underlying structure from high temperatures on the outside. Looking at TPSs, one can distinguish two categories: active and passive systems. Passive systems have no working fluid to remove the heat, the heat is absorbed in the structure or radiated away from the surface. Active systems have a working fluid removing heat, a coolant is circulated in or provided to the system the remove the heat. Another way of dividing the TPSs in categories is to look at their re-usability. Passive systems are often single use and active systems are multi use. Current-day missions use passive systems such as insulators or ablators, for instance Skylon uses corrugated reinforced glass ceramic sheets as insulator (Eggers et al., 2011), but these systems are limited by the use of the material. Their capability of withstanding heat load is dependent on the mass, specific heat capacity, maximum use temperature and initial temperature of the structural material exposed to aerodynamic heating (Blosser, 2000).

The limitations of the material used also reflects on the design of the vehicle. Existing space vehicles, more specifically re-entry vehicles, have a low to moderate lift-to-drag ratio (L/D). The choice for blunt bodies (low L/D) is clarified by looking at the heat rate and heat load. The heat rate is the instantaneous heat flux at a point on the vehicle and the heat load is the integration of the heat rate over time. Since the heat rate is inversely proportional to the square root of the nose radius, it is clear that a large nose radius reduces the heat rate. A low L/D also means a low ballistic coefficient, meaning that the vehicle is subjected to high deceleration by drag. As a consequence, the flight path will be steep minimizing the flight time and thus reducing the heat load. The combination of a large nose radius and a low ballistic coefficient defines the TPS in

[1] https://www.nasa.gov/mission_pages/explorer/bumper.html

terms of used material and thickness. Increasing the nose radius will result in a heat rate within the material capabilities and the flight path angle will be the defining parameter for the thickness of the TPS and its mass. Such missions are typically equipped with a passive TPS.

However, if one wants to increase the flight path and ensure a safer re-entry flight, the L/D needs to be increased. Increasing the L/D has the following advantages: Firstly, a higher L/D increases the (cross-)range of the vehicle. Global range can be reached with a hypersonic L/D of 3.23 (Buursink, 2005). From a given re-entry point, multiple landing sites are reachable and vice versa a landing site can be reached from multiple orbits. The increase in cross-range also reduces the dead zones, periods during ascent where no recovery in case of failure is possible (Tumino, 2003). Another advantage of increasing the L/D is the ability to postpone its re-entry into the dense atmosphere and decelerate the vehicle at higher altitude. Decelerating at high altitude results in a lower heating rate due to the the low density of the atmosphere. The increased L/D also means that the deceleration is distributed over a larger amount of time. The deceleration will be smaller by the heat load will increase due to the extended flight time. A higher L/D has the major disadvantage that the thermal loading will increase. Not only the heat load will increase due the extended flight time, but also the heat rate will increase. A higher L/D means a decrease in nose radius of the vehicle. As stated before, the heat rate is inversely proportional to the square root of the nose radius, decreasing the radius will result in a higher heat rate. Given the limitations of passive TPSs, active TPSs need to applied to cope with the increased thermal loading when designing a high L/D vehicle.

1.2. Research objectives

The question that rises when designing a new re-entry vehicle is the research question of this thesis:

Can an active thermal protection system improve the flying characteristics and the flight performance of a re-entry vehicle?

To answer this question, several steps need to be taken: from selecting a TPS to verify the process with an experiment to flight testing. This thesis research focusses on the first step, to study a TPS and designing a experiment to verify its process. This will be done by answering the following sub-questions:

1. Which active TPS is the most suited to be applied on a re-entry vehicle?
2. What is the effect on the behaviour of the vehicle when an active TPS is applied?
3. What is the effect on the thermal loading acting on the vehicle if an active TPS is applied?
4. Is the TPS a feasible alternative to current-day passive TPSs?
5. How can the TPS be validated using an flight experiment?

To answer these questions, several sub-objectives are set:

1. Selection of the most suited active TPS.
2. Development of a flight simulator capable of simulating the trajectory and stability of the reference vehicle.
3. Development of a thermodynamic analyser capable of estimating the wall temperature of the TPS.
4. Optimization of the TPS using the developed tools and a feasibility study of the proposed TPS.
5. Design of the experiment to validate the TPS.

In the development of the tools and the experiment, a reference vehicle is considered: the T-Minus Dart[2]. The sounding rocket is developed by the Delft based company, T-Minus Engineering and is capable of reaching altitudes between 50 and 120 km altitude. The rocket consist of a booster and a dart shaped payload module.

The selection of the TPS is critical for the development of the tools. It defines the shape of the nose of the vehicle and determines the impact of the system on the maximum temperatures and thermal loading.

[2] http://www.t-minus.nl/products/dart

Changing the nose of a vehicle results in a change of behaviour of the vehicle during flight, the flight simulator is developed to give insight in the behaviour of the vehicle and the whether the nose design will affect the stability of the vehicle. The nominal trajectory treated in this thesis is a launch trajectory: the ascent and descent phase of a sounding rocket is modelled. The trajectory of the rocket defines the heat load acting on the vehicle. With the outcome of the tools, the TPS can be subjected to a sensitivity analysis to obtain the most suited design. For the final design and selection of the optimal trajectory, the feasibility of the experiment is determined. The objective of this research is to determine the impact of applying an active TPS on a space vehicle and to show the feasibility of a validation experiment for this system.

1.3. Thesis outline

The steps taken in this research are described in this thesis, their theoretical approach and results are treated. In Chapter 2, active TPSs are treated. It starts with an overview of past mission followed by the selection of the TPS and the formulation of the requirements. Chapter 3 stated the theory behind the flight simulator tool and Chapter 4 gives the description of the tool together with a discussion of the reference vehicle. Chapter 5 describes the thermodynamic analyser tool from theory to results and sensitivity analysis. Chapter 6 answers the feasibility question and gives the design of the TPS and the experiment. Finally, Chapter 7 completes this thesis with conclusions and recommendations for future work.

2

Active Thermal Protection Systems

In this chapter, active TPSs will be treated. To obtain an overview of the work done in the past, the mission heritage will be discussed in Section 2.1 with an overview of the past missions equipped with an active TPS. Secondly, in Section 2.2 an in-depth discussion of the selected TPS will be given. Thirdly, a detailed mission and vehicle description is given in Section 2.3. The chapter is concluded with the requirements on the mission, TPS and experiment in Section 2.4.

2.1. Mission heritage

The heritage missions were selected using a literature survey where the focus lay on missions with an active and reusable thermal protection system. There were four concepts identified: transpiration, film, convective and enhanced radiation cooling. Transpiration and film cooling use a coolant ejected from the surface to block the heat laod from reaching the surface. The coolant is transported from a holding container to the surface and then ejected. Both systems are capable of accommodating large heat fluxes. Convective and enhanced radiation cooling remove the heat load by circulating the coolant trough the structure. The heating is transferred trough the outer skin into the coolant. The first three systems are schematically shown in Figure 2.1 and the enhanced radiation system is shown in Figure 2.2. Four heritage missions were selected where one of the active cooling concepts was implemented and/or tested during the mission: BOR-4 (convective cooling), NASP (film and convective cooling), SHEFEX II (transpiration cooling) and EXPERT (enhanced radiation cooling).

2.1.1. Mission overview

Bespilotnyi Orbital'nyi Raketoplan 4 (BOR-4)

The BOR-4 was a flying re-entry vehicle used as a test bed for the thermal protection components of the Buran. The trajectory of the BOR-4 was determined by the re-entry trajectory of the Buran and during its trajectory the TPS was put to the test. The TPS consisted of two parts: an ablative insulator at the lower surface using the same material and technology as the Buran and a convective cooling system at the wings. The latter was proposed since the thickness of the wings was relatively small and the insulator could not provide the necessary reliability without the maximum allowable thickness. Therefore, a convective cooling system was designed.

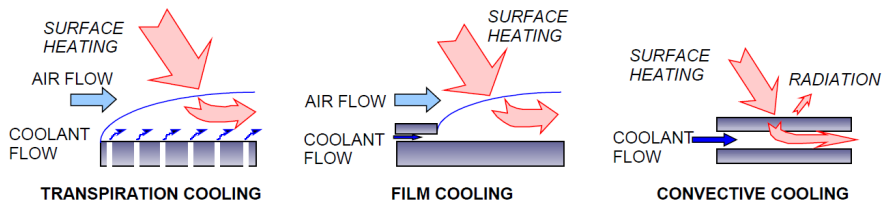

Figure 2.1: Types of active TPS (Blosser, 2000)

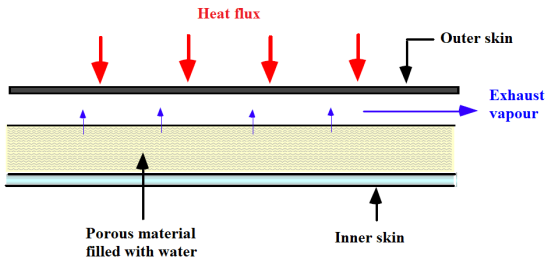

Figure 2.2: Enhanced radiation cooling concept (Sudmeijer et al., 2003)

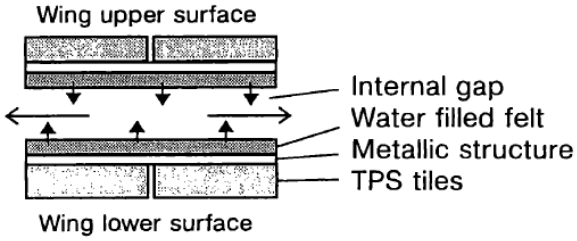

Figure 2.3: BOR-4 TPS at wings (Lozino-Lozinsky and Timoshenko, 1999)

The TPS is shown in Figure 2.3 and consists of an internal volume of the wing filled with porous felt material impregnated with a special water based composition. During flight, the water vaporised and provided effective cooling to the structure. This system proved to be successful in cooling down the wings to within the maximum allowable temperature.

National Aero-Space Plane (NASP)
The NASP program was intended to develop a single-stage-to-orbit vehicle using air-breathing engines. As a technology demonstrator project for future spacecraft, the Rockwell X-30 was developed. Active TPSs were developed to protect the vehicle and the internal components for the thermal loading. The external surfaces of the vehicle were protected by means of high-conductivity materials and heat pipes. Heat pipes operate under the same principle as convection cooling, but in a smaller scale. As a sensitivity analysis, the heat pipe was upgraded with film cooling, where the vapour is ejected in the boundary layer trough the stagnation point on the leading edge. It was shown that with the use of water and helium the temperature drops by 50% (Colwell and Modlin, 1992). Implementing the film cooling in the TPS would bring major design considerations and the heat pipes provided enough protection from the thermal loading that the film cooling was excluded from the design.

The engine of the vehicle needs to be cooled to cope with the high temperature gasses. To protect the engine and internal structure of the vehicle, a convective cooling TPS was developed. The operating principle is shown in Figure 2.4. The system makes use of the cryogenic hydrogen fuel as a heat sink. It pumps the fuel from the tank trough a panel cooling it as it passes trough to the engine.

Sharp Edge Flight Experiment II (SHEFEX II)
SHEFEX II is a mission conducted by Deutsches Zentrum für Luft- und Raumfahrt e.V. (DLR), to serve as a test bed for re-entry experiments. One of the main focus areas was the TPS, 8 single TPS or material experiments were designed. Most of the experiments focussed on the use of new material, but one experiment was a technology demonstrator for transpiration cooling: Aktive Kühlung durch Transpiration im Versuch (AKTiV). The transpiration cooling experiment uses a porous material at he outer surface trough which a coolant flows into the boundary layer. In the centre of a pair of TPS panels, a porous probe will be inserted. This porous probe is to be run through by the coolant and is pressed into the surrounding Carbon Fibre Reinforced Silicon Carbide Composites (C/C-SiC) TPS material by a compression ring. The pressure reservoir is flanged to the C/C-SiC ceramic by riveted ceramic fasteners. The reservoir itself is made of stainless steel (Weihs et al., 2008).

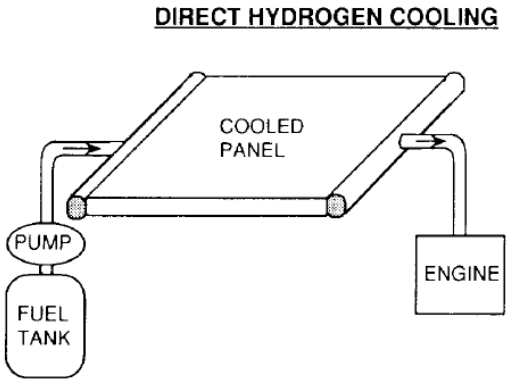

Figure 2.4: Convective cooling principle X-30 (Kelly and Blosser, 1992).

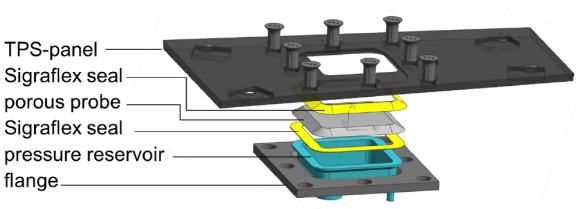

Figure 2.5: AKTiV experiment as mounted on SHEFEX II (Böhrk, 2014).

The system is shown in Figure 2.5. The influence of the cooling experiment is shown in Figure 2.6, where C7 is the uncooled and C3 is the cooled panel. An significant temperature drop of around 100 degrees of the wall temperature is obtained when the cooling system is used.

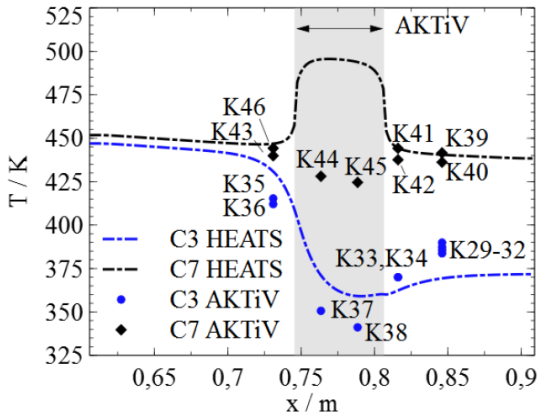

Figure 2.6: AKTiV experiment influence on the wall temperature (Böhrk, 2014).

European eXPErimental Re-entry Testbed (EXPERT)
The EXPERT mission is a flight testbed to obtain aerothermodynamic flight data for the validation of tools, test facilities and verification techniques. The vehicle carried experiments to perform aerothermodynamic measurements and test re-entry technologies. One of the experiments on-board of the vehicle is an enhanced radiation cooling experiment. The experiment is shown in Figure 2.7, and consists of an container made from

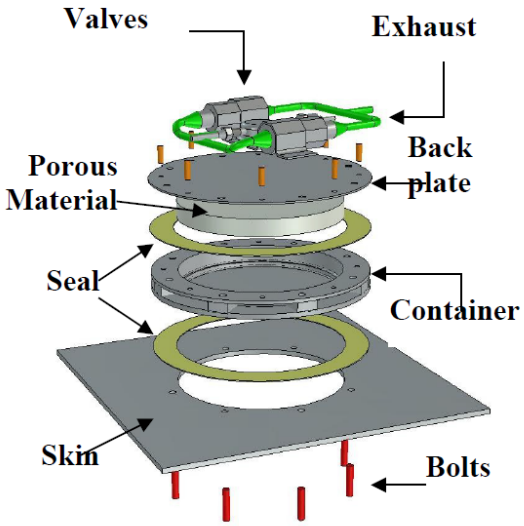

Figure 2.7: The enhanced radiation cooling experiment as mounted on EXPERT (Sudmeijer, 2005).

PM1000 filled with a porous material containing water. During flight, the water heats up and the evaporated water vapour cools down the surface skin material. The vapour is then ejected from the system using pipes to the base of the vehicle to avoid boundary layer contamination. Sadly, the mission is never carried out.

2.1.2. TPS selection

The active TPS that is selected for this thesis research, is the enhanced radiation cooling. This TPS is selected because of the following reasons:

1. Enhanced radiation cooling is capable of both cooling down large and small surfaces. The latter is of particular interest because it can be applied on the nose and leading edges of space vehicle. Doing so will reduce the nose and leading edge radius resulting in a reduction of the drag acting on the vehicle and a increase in the L/D.

2. The concept can be applied to a large range of materials, from metallic to composite materials. This is due to its capability of withstanding high temperatures and heat fluxes.

3. The concept is able to be operated during hypersonic flight, enabling its use for re-entry vehicles. Furthermore, it can be designed as a closed system, removing the possibility of boundary layer contamination resulting in a safer re-entry vehicle.

4. The concept is simple in design and can be manufactured at low cost. It is also the only system that an easily be mounted on a sounding rocket.

5. The cooling system is the only not validated concept. The verification process is carried out by (Bursink, 2005), but has not been validated yet. The verification test were carried out at Delft University of Technology, providing the necessary background and data to set up a validation experiment for the enhanced radiation cooling TPS.

2.2. Enhanced radiation cooling

2.2.1. Process overview

A conventional thermal protection system, as shown in Figure 2.8, consist of an outer material that is able to withstand high temperatures, combined with an insulator beneath to hold of the heat transfer to the inner structures. The system operating principle consist of rejecting as much of the incoming thermal loads as possible and minimizing the heat transfer to the inner structure. Modelling such a system depends on an equilibrium temperature where the incoming aerodynamic heat flux is balanced by the thermal radiation

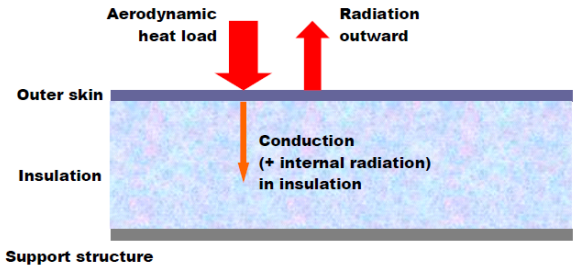

Figure 2.8: Representation of a conventional thermal protection system. (Buursink and Sudmeijer, 2004)

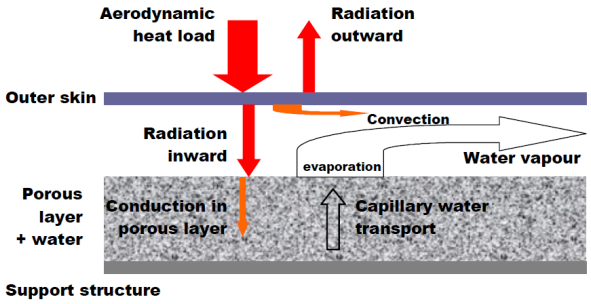

Figure 2.9: Representation of the enhanced radiation cooling thermal protection system. (Buursink and Sudmeijer, 2004)

from the surface. To increase the maximum allowable thermal load, enhanced radiation cooling is applied to the system. This process increases the energy radiated away from the surface by not only outwards but also inwards radiation. To achieve this, the insulation needs to have a low temperature and will remain cold while absorbing thermal radiation from the outer skin. This system is displayed in Figure 2.9. To obtain a cooled insulation the porous material is filled with a liquid (for instance with water). The evaporation of the water keeps the surface temperature at a constant value, namely the boiling temperature of water. This process will keep the surface temperature of the porous material low, provided that the internal transport of water to the surface is sufficiently high enough. The vapour in the system needs to be vented out, to ensure the continuous flow of the vapour.

2.2.2. Process development

As stated in Section 2.1, an enhanced radiation TPS was developed for the EXPERT mission. In the process of designing the cooling experiment, a verification experiment was performed to provide a proof of concept for the enhanced radiation cooling system. This work is presented in (Buursink, 2005) and summarised below to obtain an overview of the work done.

The verification set-up, shown in Figure 2.10, consisted of two square cooling panels with an outer skin made from PM1000 and with a skin thickness of 1 mm as shown in Figure 2.9. The right panel was filled with water and the left panel was kept 'dry'. By doing this the impact of the cooling system could be determined.

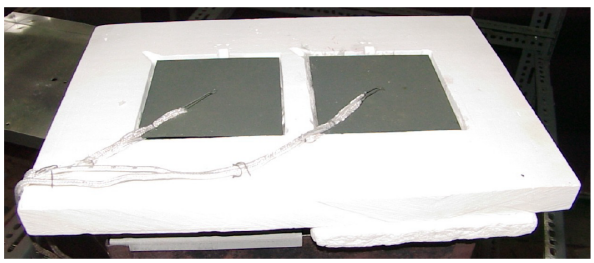

Figure 2.10: Test set-up to proof concept enhanced radiation cooling (Sudmeijer, 2005).

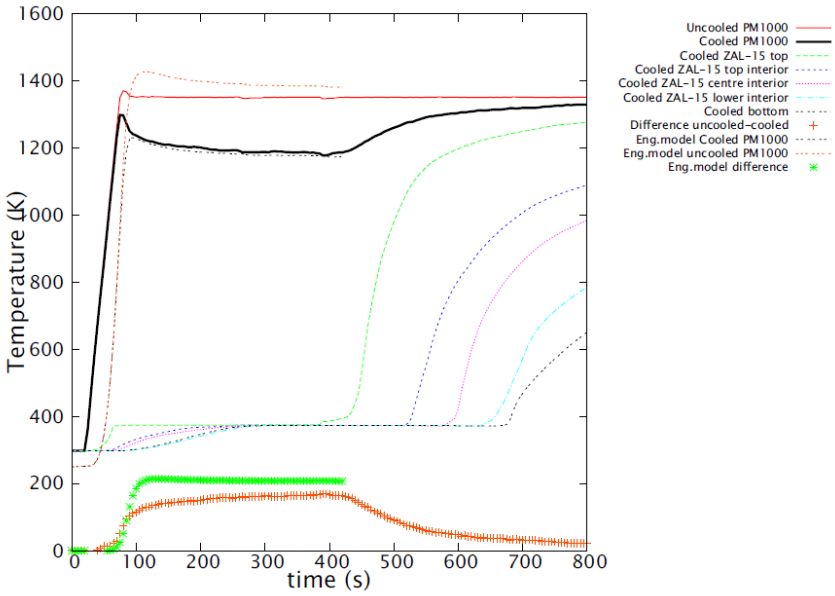

Figure 2.11: Temperature measurements of the test set-up (Buursink, 2005).

Figure 2.11 shows the surface temperature of both panels under to thermal loading of 1350 K. The red (uncooled), black (cooled) and dashed green (surface temperature porous material) curves are of interest: it can be seen that during the test the surface temperature of the porous material remains af the boiling point of water as long as the availability of the water is sufficiently large enough. The effect of the cold surface can be seen in the reduction of the wall temperature of the cooled panel of approximately 200 degrees. After the depletion of the water, the surface temperature of the cooled panel is rising to the surface temperature of the uncooled panel. This test confirmed the predictions of the enhanced radiation cooling concept.

The study has shown that the enhanced radiation cooling system has great potential, and draw the following conclusions relevant for this research:

1. The combination of the materials used (ZAL-15, PM1000 and water) has result in a very high performance of the system that can be be easily matched by other combination of materials. It is recommended to use the same materials in future work.

2. It has been shown that the amount of water effectively used to cool down the outer wall is around 80 % of the total volume. This is due to the saturation level of water. For a skin temperature of approximately 1000K, the critical saturation level varies form 77% to 87%.

3. The maximum heat flux to which the system can be subjected is 8 MW/m^2. For higher heat fluxes, a thin layer of vapour will develop between the water and the nose wall preventing effective heat transfer between the outer skin and the water. The evaporation rate will be reduced and the temperature will quickly rise, this effect will have a negative impact on the cooling properties of the system.

2.3. Mission and vehicle description

2.3.1. Configuration geometry and packaging

The experiment shall be mounted on the T-Minus Dart, a sounding rocket capable of reaching altitudes between 50 and 120 km altitude. The rocket consist of a booster and a dart shaped payload module. The stages of the rocket are shown in Appendix A, the main characteristics[1] are displayed in Table 2.1 and 2.2 for the booster and Dart respectively.

[1] Obtained from http://www.t-minus.nl/products/dart/, accessed 28/10/2017

Table 2.1: Booster characteristics

Motor dimension	
Diameter	0.118 m
Length	2.3 m
Motor performance	
Burn time	5 s
Average thrust	8 kN
Motor weights	
Propellant mass	22 kg
Loaded mass	29 kg
Other characteristics	
Propellant type	AP composite
Casing material	carbon fiber reinforced plastic
Nozzle material	Aluminum/graphite

Table 2.2: Dart characteristics

Motor dimension	
Diameter	35 mm
Length	1.2 m
Motor performance	
Total mass	3.5 kg
Payload mass	0.5 kg
Motor weights	
Max acceleration	< 60g
Maximum Mach number	5.2

Constraints
The experiment will be mounted on the Dart as a replacement of its original nose, therefore the experiment is constrained to the following parameters (see Figure 2.12):

- Maximum outside diameter : 35 mm
- Maximum inside diameter: 30 mm
- Maximum body length (inside Dart): 700 mm

2.3.2. Flight envelope and trajectory definition

The T-Minus Dart is launched using a mobile launcher. After ignition, the booster provides thrust for 5 seconds after which the booster and the Dart separate. The booster follows a ballistic trajectory back to Earth. The Dart continuous its coasting ascent until apogee, then it return to the Earth in a coasting descent. During this thesis research two trajectories will be modelled, an high and a low altitude trajectory. By studying both trajectories, a trade-off can be made for the launch envelope of the validation experiment. The selected trajectories are the launches at 30 and 85 degrees elevation. Evaluating both trajectories will give insight in the behaviour of the rocket equipped with the cooling experiment and the influence fo the trajectory on the wall temperature and the cooling effect of the enhanced radiation TPS. The launch conditions are stated in

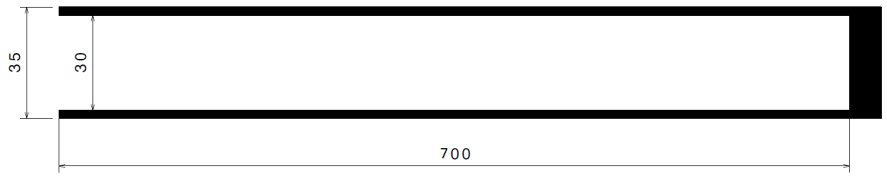

Figure 2.12: Experiment constraints, all dimensions in mm

Table 2.3: Initial conditions for the T-Minus Dart

Parameter	Mission 1	Mission 2
Length launch rail	3.4 m	3.4 m
Elevation angle	30 deg	85 deg
Azimuth angle from north	90 deg	90 deg

Table 2.4: Trajectory parameters of the nominal missions T-Minus Dart

Parameter	Mission 1	Mission 2
Time of separation	5 s	5 s
Apogee	11 km	98 km
Time till apogee	43 s	144 s
Range	60 km	37 km
Time till touchdown	99 s	290 s
Maximum Mach number	4.8 [-]	4.8 [-]
Maximum acceleration	356 $m \cdot s^{-2}$ (36 g)	356 $m \cdot s^{-2}$ (36 g)

Table 2.3. The parameters that define the trajectory of the rocket are shown in Table 2.4 and the plot of the trajectories are shown in Figure 2.13 and 2.14 for the 30 and 85 degrees elevation respectively. An in-depth discussion of the T-Minus Dart rocket is given in Section 4.5.

A typical trajectory is shown in Figure 2.15 as proposed by the company behind the sounding rocket. It shows the launch using the mobile launch tower. The launch tower gives the rocket a spin rate used to stabilise the rocket. The spinning motion is shown in Figure 2.16 and reaches a maximum value after approximately 1.5 seconds and then slowly converges to zero since the fins of the rocket are placed in line with the body and are not canted. This does not create an up-spinning motion and the spin rate disappears. The rocket is accelerated for 5 seconds, after burnout the booster and Dart separate by the large drag forces acting on the booster. The Dart continues its trajectory until it reaches apogee, after which the payload is deployed. The rocket then follows a ballistic trajectory back to Earth.

[2]https://www.kivi.nl/uploads/media/58b03c2731d78/Ruimtevaart-Mark%20Uitendaal-T-Minus%20Engineering.pdf

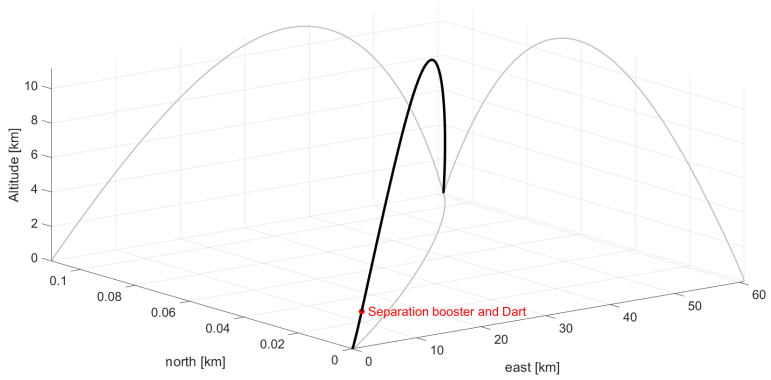

Figure 2.13: Trajectory of the T-Minus Dart launched at 30 degrees elevation.

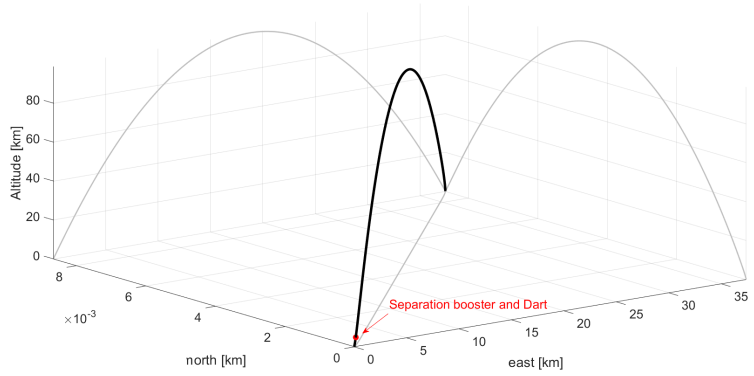

Figure 2.14: Trajectory of the T-Minus Dart launched at 30 degrees elevation.

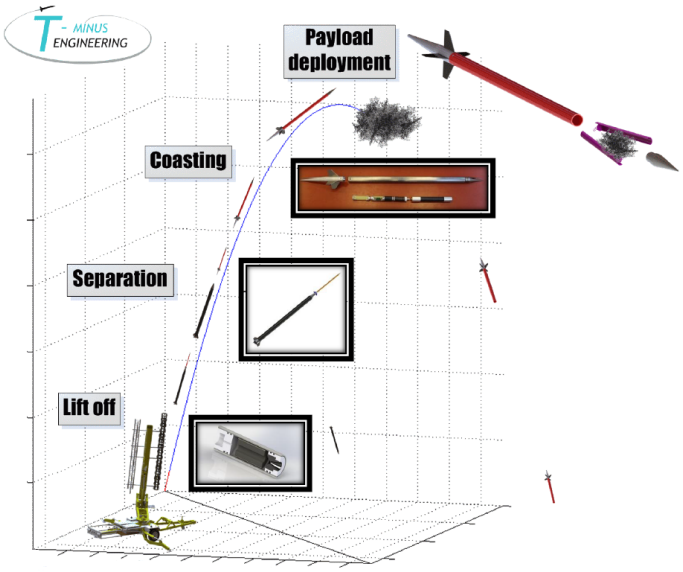

Figure 2.15: Proposed trajectory T-Minus Dart.[2]

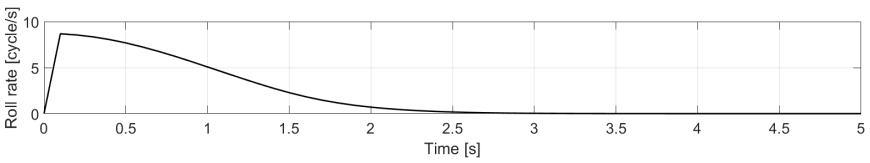

Figure 2.16: Spin rate of the T-Minus Dart.

2.4. Requirements

The experiment will be a success if the requirements stated below are met. The requirements are divided into 3 categories: science, mission and spacecraft, and system requirements. These requirements are preliminary, top-level requirements needed in this research. The system requirements are a combination of top-level requirements and acquirements identified during the research.

2.4.1. Science requirements

SR.01: The experiment shall produce a GPS output that enables the determination of the trajectory and velocity profile of the rocket to an accuracy of TBD centimetre (per second).
SR.02: The experiment shall produce an Inertial Measurement Unit (IMU) output that enables the determination of the angular rates of the rocket to an accuracy of TBD degree per second.
SR.03: The experiment shall produce a temperature product that enables the modelling the wall temperature of the rocket nose to an accuracy of TBD K.

The experiment will be considered a success if it measures the wall temperature of the nose of the rocket and provides a accurate trajectory, velocity and angular rate profile needed to model the effect of the enhanced radiation cooling experiment.

2.4.2. Mission and spacecraft performance

MSP.01: The experiment shall be designed as a stand-alone system.
MSP.02: The experiment shall be mounted on the T-Minus Dart rocket.
MSP.02.01: The outside diameter of the experiment shall not exceed 35 mm.
MSP.02.02: The inside diameter of the experiment shall not exceed 30mm.
MSO.02.03: The maximum total length of the experiment and instruments shall not exceed 700mm.
MSP.03: The experiment shall have repair and replacement on-site procedures in case of damage and failure.
MSP.04: The experiment shall be launched in accordance with the launch site regulations.

2.4.3. System requirements

ER.01: The system shall be able to withstand a heat load of 8 MW/m^2 in the stagnation point.
ER.02: The system shall be able to withstand mechanical loading without failure in the form of yielding, buckling or fracture.
ER.02.01: The system shall be able to withstand an acceleration of 40 g.
ER.03: The system shall not experience a deflection larger than TBD millimetre under the thermal and mechanical loading.

3

Flight Dynamics

In this chapter, a summary of the flight dynamics of a sounding rocket is given. First, the required degrees of freedom are stated in Section 3.1, followed by the definition of the environment and the required accuracy in Section 3.2. Next, the equations of motion are stated in Section 3.3. It states the coordinate systems and the transformations between them, followed by the definition of the state variables and the section is finalised with an overview of the equations of motion. In Section 3.4, the Magnus effect and its influence is treated. The chapter is finalised with an overview of the external forces and moments in Section 3.5.

3.1. Degrees of freedom

To accurately model both a re-entry and launch trajectory, the tool needs to have 6 degrees of freedom (DOF). The body is free to change position in the X, Y and Z direction and to change orientation to rotate around those axes. The study of the translational and rotation motion will provide insight in the static and dynamic stability of the rocket. For the T-Minus Dart, this stability study determines the feasibility of its use for this experiment. The dynamic stability is particularity important because the rocket uses a spin rate to stabilise itself after launch.

3.2. Flight environment

3.2.1. Earth

As stated in the requirement in Section 3.1, the software must be capable to simulate both launch and re-entry trajectories. This means that the Earth must be modelled as a rotating sphere. The rationale behind this can be explained by looking at the z-component of the force equation for a horizontal flight at the equator (Etkin, 1972):

$$-L + mg = 2mV\omega + \frac{mv^2}{\Re} \tag{3.1}$$

The right-hand side of Equation (3.1) is the area of interest: the first term is the Coriolis force due to the Earth rotation and the second term is the Earth curvature. Both terms are dependent on the velocity of the rocket, the first linearly and the second quadratically. (Etkin, 1972) defines the boundary to which the Earth rotation and curvature can be neglected as approximately one-tenth of the orbital speed (±800 m/s or ±2.5 Mach). At this boundary, the influence of the Earth rotation and curvature is about 1% of the weight. Looking at the maximum Mach number of the T-Minus Dart rocket as stated in Section 2.3, it is clear that the effect needs to be taken into account.

The Earth is considered to be a central body as a rotating spheroid. The reference spheroid is displayed in Figure 3.1. The rotation of the Earth is assumed to be constant and directed along the Z_g-axis of the rotating geocentric reference frame (defined in Section 3.3.1):

$$\boldsymbol{\omega_{cb}} = \begin{bmatrix} 0 \\ 0 \\ \omega_{cb} \end{bmatrix}$$

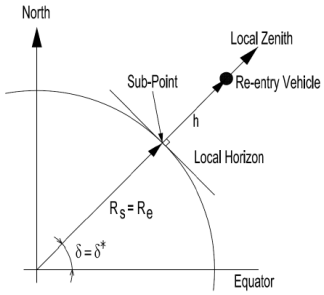

Figure 3.1: The vehicle above the reference spheroid. (Mooij, 2015)

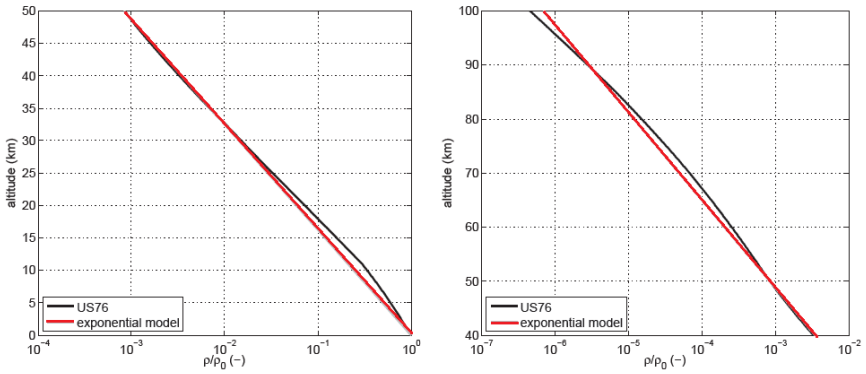

Figure 3.2: Density profile according to the exponential atmosphere model and the US76. (Mooij, 2015).

3.2.2. Atmosphere

The software needs to be able to model the aerodynamic forces and moments acting on the rocket, this means that the software has to model the atmosphere in which the rocket operates. The magnitude of the forces and moments are depend on the dynamic pressure, which is a function of the atmospheric density. Also, the thermodynamic model used to estimate the wall temperature depends highly on the atmospheric properties to estimate the stagnation point heat flux. The two most commonly used models are the exponential atmosphere and the United States Standard Atmosphere released in 1976 (US76). Looking at the difference between both models concerning the atmospheric density (see Figure 3.2), it is clear that these models have only a small difference between them. The US76 model has more accuracy in modelling the deviations in the density profile compared to the exponential model, but the difference between them is small enough to be neglected. The difference in temperature profile between the exponential model and the US76 model is the decisive factor. The exponential model estimates the temperature profile as a linear function, whereas the US76 model gives a non-linear estimation (see Figure 3.3). The US76 model has a fluctuating curve, giving a more accurate representation of the temperature profile of the atmosphere. The superior accuracy of the US76 model is the reason af selecting this model to obtain the atmospheric properties.

The US76 model is implemented in the software by using a look-up table, where the pressure, density, temperature of speed of sound is defined in function of the altitude (National Oceanic and Atmospheric Administration, 1976). Cubic spline interpolation is used to determine the atmospheric properties. It is shown that cubic spline gives better results than using a linear interpolation (Volckaert, 2007). The model is defined between 0 and 84,852 m altitude, outside this interval the values are extrapolated. The temperature is extrapolated linearly and the pressure logarithmically[1].

[1] https://nl.mathworks.com/help/aerotbx/ug/atmoscoesa.html

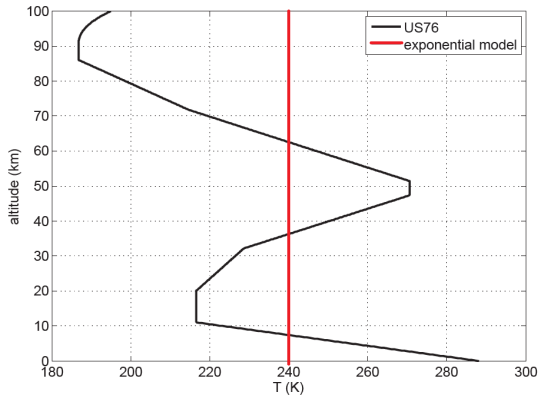

Figure 3.3: Temperature profile according to the exponential atmosphere model and the US76. (Mooij, 2015).

3.3. Equations of motion

3.3.1. Coordinate systems

Definitions

During the derivation of the equations of motion, four reference frames are defined (displayed in Figure 3.4):

1. *Inertial reference frame* (XYZ): The centre of the frame is the centre of the Earth. The Z-axis coincides with the rotation axis of the Earth, positive in northern direction. The X-axis lies in the equatorial plane and points towards the vernal equinox. And the Y-axis completes a right-handed Cartesian reference frame.

2. *Rotating geocentric reference frame* ($X_gY_gZ_g$): this has the same definition as the inertial reference frame only the frame rotates along its Z_g axis with the same angular velocity of the Earth.

3. *Vehicle-centred vertical reference frame* ($X_vY_vZ_v$): used for describing the orientation of the rocket and its velocity vector relative the Earth's surface. The X_vY_v-plane is taken to be the local horizontal plane. The centre of mass of the vehicle is the origin of the frame. The X_v-axis is along the north-south direction, positive to the north. The Y_v-axis is along the east-west direction, positive to the east. And the Z_v-axis is along the radius vector from the centre of the Earth positive downwards.

4. *Body-fixed reference frame* ($X_bY_bZ_b$): the centre of mass of the vehicle is the origin of the frame. The X_b-axis lies along the longitudinal axis of the rocket, positive forwards. The Y_b-axis and the Z_b-axis lie along the other two principal axis of inertia of the vehicle in such a way that the the frame is right-handed. In this reference frame the aerodynamic forces and moments are defined.

Transformations between reference frames

Definition of the transformations matrices:

Any transformation can be described as a combination of unit-axis rotations. A sequence of unit axis-rotations can be represented as a single matrix by multiplying the different unit rotation matrices in sequential order. Suppose a vector is defined in the F_1-frame, the coordinates of that vector expressed in the F_2-frame rotated by an arbitrary angle, φ_x, about the X-axis is shown in Figure 3.5 and defined as (Mulder et al., 2013):

$$\begin{aligned} v_x^2 &= 1\cdot v_x^1 + 0\cdot v_y^1 + 0\cdot v_z^1 \\ v_y^2 &= 0\cdot v_x^1 + \cos\varphi_x\cdot v_y^1 + \sin\varphi_x\cdot v_z^1 \\ v_z^2 &= 0\cdot v_x^1 - \sin\varphi_x\cdot v_y^1 + \cos\varphi_x\cdot v_z^1 \end{aligned} \tag{3.2}$$

The transformation matrix is then defined as:

$$\mathbf{C}_{\varphi_x} = \begin{bmatrix} 1 & 0 & 0 \\ 0 & \cos\varphi_x & \sin\varphi_x \\ 0 & -\sin\varphi_x & \cos\varphi_x \end{bmatrix} \tag{3.3}$$

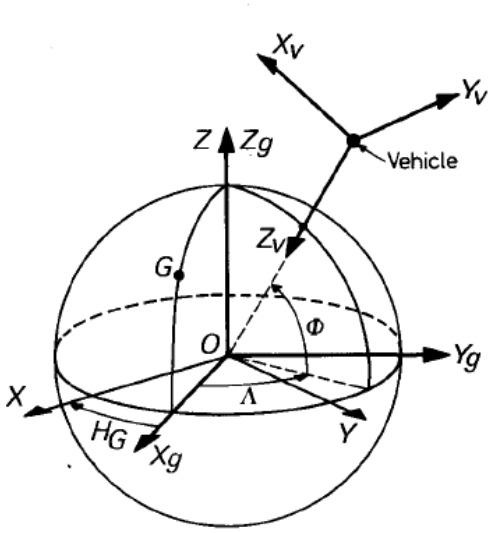

Figure 3.4: The inertial, rotating geocentric and vehicle-centred horizontal reference frame. (Cornelisse et al., 1979)

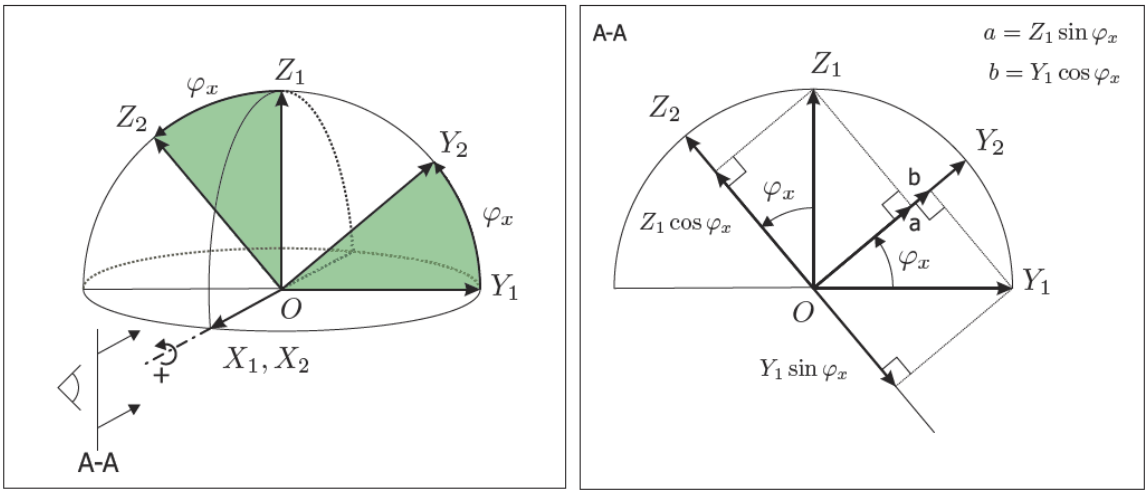

(a) 3D view of rotation

(b) 2D view of rotation

Figure 3.5: Vector decomposition for rotation about X-axis. (Mulder et al., 2013)

The transformation matrices for the rotation about the Y axis (φ_y) and Z axis (φ_z) are defined as:

$$\mathbf{C}_{\varphi_\mathbf{y}} = \begin{bmatrix} \cos\varphi_y & 0 & -\sin\varphi_y \\ 0 & 1 & 0 \\ \sin\varphi_y & 0 & \cos\varphi_y \end{bmatrix} \tag{3.4}$$

$$\mathbf{C}_{\varphi_\mathbf{z}} = \begin{bmatrix} \cos\varphi_z & \sin\varphi_z & 0 \\ -\sin\varphi_z & \cos\varphi_z & 0 \\ 0 & 0 & 1 \end{bmatrix} \tag{3.5}$$

Standard transformations:
The reference frames previously stated in this section are related to each other by the following relations.

- From inertial to rotating geocentric reference frame (see Figure 3.4): the rotating geocentric reference frame is rotated the angular velocity of the Earth about the Z-axis of the inertial reference frame.

$$\mathbf{C_g} = \mathbf{C_Z}(H_G)$$

$$\mathbf{C_g} = \begin{bmatrix} \cos H_G & \sin H_G & 0 \\ -\sin H_G & \cos H_G & 0 \\ 0 & 0 & 1 \end{bmatrix} \tag{3.6}$$

  where H_G equals $\omega(t\text{-}t_0)$.

- From rotating geocentric to vehicle-centred reference frame (see Figure 3.4): the $X_gY_gZ_g$-frame is rotated about the Z_g-axis over an angle Λ and then the system is rotated about it Y-axis over an angle $-(-\pi/2+\Phi)$.

$$\mathbf{C_{vg}} = \mathbf{C_Z}(\Lambda)\mathbf{C_Y}(-(-\pi/2+\Phi))$$

$$\mathbf{C_{vg}} = \begin{bmatrix} -\sin\Phi\cos\Lambda & -\sin\Phi\sin\Lambda & \cos\Phi \\ -\sin\Lambda & \cos\Lambda & 0 \\ -\cos\Phi\cos\Lambda & -\cos\Phi\sin\Lambda & -\sin\Phi \end{bmatrix} \tag{3.7}$$

- From vertical to body-fixed reference frame (see Figure 3.6): this transformation is defined by a rotation around three angles, the Euler angles. First, the system is rotated about the Z_v-axis over an angle ψ resulting in the $X'_vY'_vZ'_v$-frame. The, the system is rotated about the Y'_v-axis over an angle θ resulting in the $X''_vY''_vZ''_v$-frame. Finally, the system is rotated about the X''_v-axis over an angle φ to obtain the $X_bY_bZ_b$-frame.

$$\mathbf{C_{vb}} = \mathbf{C_Z}(\psi)\mathbf{C_Y}(\theta)\mathbf{C_X}(\varphi)$$

$$\mathbf{C_{vb}} = \begin{bmatrix} \cos\theta\cos\psi & \cos\theta\sin\psi & -\sin\theta \\ -\cos\varphi\sin\psi+\sin\varphi\sin\theta\cos\psi & \cos\varphi\cos\psi+\sin\varphi S\sin\theta\sin\psi & \sin\varphi\cos\theta \\ \sin\varphi\sin\psi+\cos\varphi\sin\theta\cos\psi & -\sin\varphi\cos\psi+\cos\varphi\sin\theta\sin\psi & \cos\varphi\cos\theta \end{bmatrix} \tag{3.8}$$

- From inertial to body-fixed reference frame: this transformation is obtained by performing the transformation from inertial to rotating geocentric reference frame, followed by the transformation from rotating geocentric to vehicle-centred vertical reference frame and finally from vehicle-centred vertical to body-fixed reference frame.

$$\mathbf{C_r} = \mathbf{C_{rv}}\mathbf{C_{vg}}\mathbf{C_g} \tag{3.9}$$

$$\mathbf{C_r} = \begin{bmatrix} \cos\theta\cos\psi & \cos\theta\sin\psi & -\sin\theta \\ -\cos\varphi\sin\psi+\sin\varphi\sin\theta\cos\psi & \cos\varphi\cos\psi+\sin\varphi S\sin\theta\sin\psi & \sin\varphi\cos\theta \\ \sin\varphi\sin\psi+\cos\varphi\sin\theta\cos\psi & -\sin\varphi\cos\psi+\cos\varphi\sin\theta\sin\psi & \cos\varphi\cos\theta \end{bmatrix}$$
$$\times \begin{bmatrix} -\sin\Phi\cos\Lambda & -\sin\Phi\sin\Lambda & \cos\Phi \\ -\sin\Lambda & \cos\Lambda & 0 \\ -\cos\Phi\cos\Lambda & -\cos\Phi\sin\Lambda & -\sin\Phi \end{bmatrix}$$
$$\times \begin{bmatrix} \cos H_G & \sin H_G & 0 \\ -\sin H_G & \cos H_G & 0 \\ 0 & 0 & 1 \end{bmatrix}$$

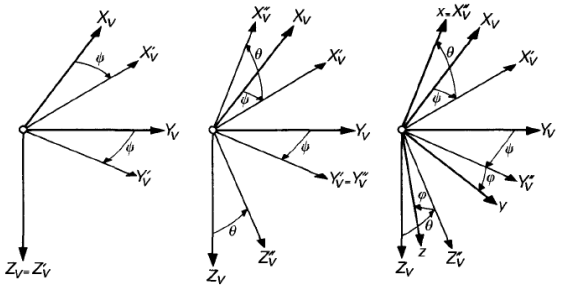

Figure 3.6: The vehicle-centred horizontal and vehicle reference frame with yaw, pitch and bank angles. (Cornelisse et al., 1979)

3.3.2. State variables

Position and velocity

Cartesian components:

The state variables for position and velocity are expressed in Cartesian components with respect to the inertial or rotating reference frame. Both reference frames use the same variables but with different subscripts. The variables are:

- Position: x, y, z
- Velocity: $\dot{x}, \dot{y}, \dot{z}$

Note that the velocity components $\dot{x}, \dot{y}, \dot{z}$ are commonly noted as u, v, w.

Spherical components

The spherical position and velocity are defined with respect to the rotating reference frame, they are expressed by:

- Position: distance $\Re$, longitude μ and latitude λ
- Velocity: groundspeed V_g, flight-path angle γ and heading χ

The longitude is measured positive to the East ($0° \leq \lambda < 360°$). The latitude is measured along the appropriate meridian along the equator, positive North and negative South ($-90° \leq \mu \leq 90°$). The distance, R, is the the distance from the centre of mass of the central body to the centre of mass of the vehicle. The relative velocity, V_g, is expressed in with respect to the rotating reference frame. The flight-path angle is the angle between the velocity vector and the local horizon. The heading defines the direction of the projection of the velocity vector in the local horizontal plane with respect to the local North ($-180° \leq \chi \leq 180°$).

Attitude and angular rates

Attitude:

The attitude of the vehicle describes the orientation of a body-fixed reference frame with respect to another reference frame. The attitude can be expressed in three definitions:

1. *Classical attitude angles*, i.e., the roll angle ϕ, the pitch angle θ and the yaw angle ψ. These angles define the attitude of the the body frame w.r.t. inertial space but can also be used to define the attitude of the body w.r.t. the local horizontal plane. These angles define the attitude of the body frame with respect to the inertial space or with respect to the local horizontal plane.
2. *Aerodynamic angles*, i.e., the angle of attack α ($-180° < \alpha \leq 180°$, for a nose-up attitude $\alpha > 0°$), the angle of sideslip β ($-90° \leq \beta \leq 90°$, β is positive for a nose-left attitude) and the bank angle σ ($-180° < i\sigma \leq 180°$, σ is positive when banking to the right). These angles define the attitude and the orientation of the body with respect to the groundspeed or with respect to the airspeed.

Angular rates:

The angular rate of the body is defined as the rotational velocity of the body frame w.r.t. inertial frame, expressed in components along the body axes. The rotation vector $\boldsymbol{\omega}$ is defined by the roll rate p, the pitch rate q and the yaw rate r (see Figure 3.7).

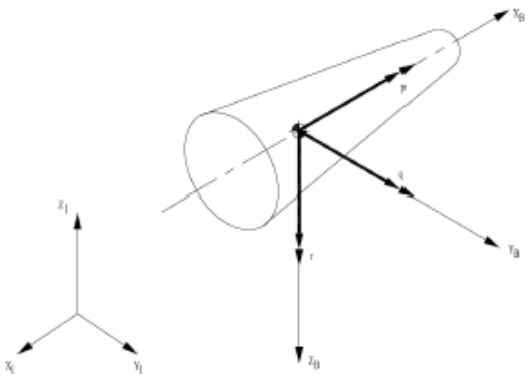

h

Figure 3.7: Definition of the angular rate of the vehicle (Mooij, 2015).

3.3.3. Set-up equations of motion

The equations of motions of motion are set up according to (Etkin, 1972). The equations of motion describe the motion of a vehicle over a spherical rotating Earth with six degrees of freedom. The assumptions are fist stated, followed by the set-up for the equations of motion.

Assumptions

The model is describing the motion of the rocket, is subjected to the following assumptions:

1. The spherical Earth is rotating about an axis fixed in inertial space, and the gravitational acceleration is a radial vector.

2. The centripetal acceleration due to the Earth rotation is neglected.

3. The atmosphere is at rest relative to the Earth.

4. The rocket is a rigid body, but the mass and moments of inertia change during the powered part of the flight.

5. The rocket is is axisymmetric around two planes of symmetry: XZ and XY (see Figure 3.8). These planes have geometric, mass and aerodynamic symmetries.

6. The thrust vector lies along the X axis of the rocket and is positive in positive X direction: $T = T_x$ and $T_y = T_z = 0$.

7. The centre of mass of the rocket lies on the X-axis.

Velocity and acceleration in a moving reference frame

All the reference frames defined in Section 3.3.1 are in motion relative to the inertial reference frame. It is desired to express the position, velocity and acceleration of the rocket in components parallel to the axes of these moving frames. Therefore, an expression for the velocity and acceleration in a rotating frame is needed. The full derivation of the equations presented next can be found in (Etkin, 1972). Looking at Figure 3.9, the velocity of the point P in the moving frame (subscript I) expressed in terms of the moving frame (subscript M) equals :

$$\mathbf{V_M} = \mathbf{V_{0_M}} + \dot{\mathbf{r}}'_{\mathbf{M}} + \boldsymbol{\omega}_{\mathbf{M}} \times \mathbf{r}'_{\mathbf{M}} \tag{3.10}$$

The first term in Equation (3.10) is the velocity of the origin of the moving frame relative to the inertial frame, the second term is relative velocity of the point P and the last term is the transport velocity. The acceleration of point P equals:

$$\mathbf{a_M} = \mathbf{a_{0_M}} + \ddot{\mathbf{r}}'_{\mathbf{M}} + \dot{\boldsymbol{\omega}}_{\boldsymbol{M}} \times \mathbf{r}'_{\mathbf{M}} + 2\boldsymbol{\omega}_{\boldsymbol{M}} \times \dot{\mathbf{r}}'_{\mathbf{M}} + \boldsymbol{\omega}_{\boldsymbol{M}} \times (\boldsymbol{\omega}_{\boldsymbol{M}} \times \mathbf{r}'_{\mathbf{M}}) \tag{3.11}$$

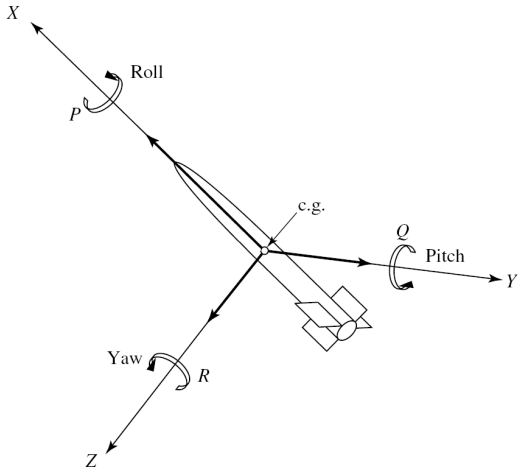

Figure 3.8: Representation of the rocket's plane of symmetry and degrees of freedom (Siouris, 2004).

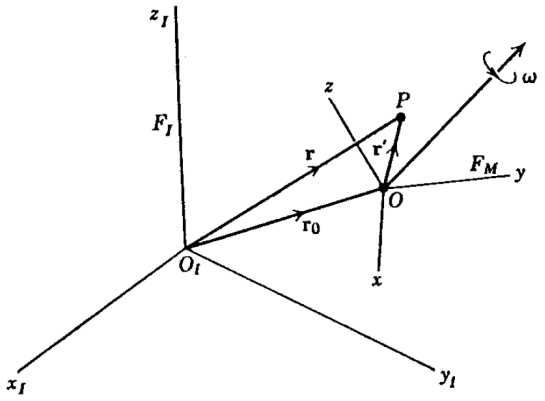

Figure 3.9: Moving coordinate system.

In Equation (3.11), the different terms are defined as:

$\mathbf{a_{0_M}}$	=	acceleration of the origin of the moving frame
$\ddot{\mathbf{a}}'_{\mathbf{M}}$	=	acceleration of P relative to the moving frame
$\dot{\boldsymbol{\omega}}_{\boldsymbol{M}} \times \mathbf{r}'_{\mathbf{M}}$	=	tangential acceleration as a result of the rotational acceleration of the moving frame
$2\boldsymbol{\omega}_{\boldsymbol{M}} \times \dot{\mathbf{r}}'_{\mathbf{M}}$	=	Coriolis acceleration
$\boldsymbol{\omega}_{\boldsymbol{M}} \times (\boldsymbol{\omega}_{\boldsymbol{M}} \times \mathbf{r}'_{\mathbf{M}})$	=	centripetal acceleration

The acceleration of the moving frame relative to the inertial frame can be expressed as the summation of three terms: the dragging, Coriolis and relative acceleration. The centripetal acceleration can be neglected as stated in the assumptions.

Angular velocities of the reference frame

In Equation (3.10) and (3.11), the angular velocity of the moving frame is needed. These angular velocities are expressed in Euler angles in the body-fixed reference frame. The Euler angular rates equal:

$$\begin{bmatrix} \dot{\phi} \\ \dot{\theta} \\ \dot{\psi} \end{bmatrix} = \begin{bmatrix} 1 & \sin\phi\tan\theta & \cos\phi\tan\theta \\ 0 & \cos\phi & -\sin\phi \\ 0 & \sin\phi\sec\theta & \cos\phi\sec\theta \end{bmatrix} \begin{bmatrix} P \\ Q \\ R \end{bmatrix} \tag{3.12}$$

Equations (3.12) can be used to determine the Euler angular rates from the relative angular velocities (P, Q, R). In turn, the relative angular velocities can be found from the body angular rates (p, q, r) by taking into account

the rotation of the Earth:

$$\begin{bmatrix} P \\ Q \\ R \end{bmatrix} = \begin{bmatrix} p \\ q \\ r \end{bmatrix} - \mathbf{C_{vb}} \begin{bmatrix} (\omega_{cb} + \dot{\mu})\cos\lambda \\ -\dot{\lambda} \\ -(\omega_{cb} + \dot{\mu})\sin\lambda \end{bmatrix} = \begin{bmatrix} p \\ q \\ r \end{bmatrix} + \begin{bmatrix} p^E \\ q^E \\ r^E \end{bmatrix} \tag{3.13}$$

In Equation (3.13), the rates of change $(\dot{\lambda}, \dot{\mu})$ are defined in the next paragraph.

The position, velocity and acceleration of the vehicle
The location of the vehicle relative to the Earth is given by the spherical polar coordinates. Their rates of change are defined as:

$$\dot{\Re} = -V_z \tag{3.14}$$

$$\dot{\mu} = \frac{V_y}{\Re\cos\lambda} \tag{3.15}$$

$$\dot{\lambda} = \frac{V_x}{\Re} \tag{3.16}$$

The components of **V** are given by:

$$\mathbf{V} = \mathbf{C_{vb}} \left(\begin{bmatrix} u \\ v \\ w \end{bmatrix} + \begin{bmatrix} W_x \\ W_y \\ W_z \end{bmatrix} \right) \tag{3.17}$$

With the assumption that the atmosphere is at rest with respect to the Earth, Equations (3.14), (3.15) and (3.16) become:

$$\dot{\Re} = V\sin\theta \tag{3.18}$$

$$\dot{\mu} = \frac{V}{\Re}\cos\theta\sin\psi\sec\lambda \tag{3.19}$$

$$\dot{\lambda} = \frac{V}{\Re}\cos\theta\cos\psi \tag{3.20}$$

$$\tag{3.21}$$

Or alternatively, expressed in terms of the body-axis velocity components:

$$\begin{bmatrix} \dot{\lambda}\Re \\ \dot{\mu}\Re\cos\lambda \\ -\dot{\Re} \end{bmatrix} = \mathbf{C_{vb}} \begin{bmatrix} u \\ v \\ w \end{bmatrix} \tag{3.22}$$

Looking back at Equation (3.11), the point O lie sin the rotating frame then $\dot{\mathbf{r}}'$ equals **V** as defined in Equation (3.17). The assumption that the Earth's axis is fixed in inertial space, $\dot{\boldsymbol{\omega}} = 0$ and the centripetal acceleration can be neglected. The acceleration is then given by, with an atmosphere at rest relative to the Earth:

$$\mathbf{a} = \ddot{\mathbf{a}}_\mathbf{M} + 2\boldsymbol{\omega_M} \times \mathbf{r}'_\mathbf{M} = \dot{\mathbf{V}} + \left(\boldsymbol{\omega} + \boldsymbol{\omega^E}\right) \times \mathbf{V} \tag{3.23}$$

$$\mathbf{a} = \begin{bmatrix} \dot{u} \\ \dot{v} \\ \dot{w} \end{bmatrix} + \left(\begin{bmatrix} p \\ q \\ r \end{bmatrix} + \begin{bmatrix} p^E \\ q^E \\ r^E \end{bmatrix} \right) \begin{bmatrix} u \\ v \\ w \end{bmatrix} \tag{3.24}$$

Where $\begin{bmatrix} p^E \\ q^E \\ r^E \end{bmatrix}$ is defined in Equation 3.13.

Euler's force and moment equations
The last set equations needed are the force and moment equations so that the position, velocity and acceleration of the vehicle can be determined. The equations are defined in the body-fixed reference frame. This is necessary to accurately model the forces and moments based on the aerodynamic coefficients and avoid

unnecessary transformations. The force equation of motion is composed using Newton's second law and Equation 3.24:

$$\mathbf{F} = m\mathbf{a} \tag{3.25}$$

Or, in component form:

$$X - mg\sin\theta = m\left(\dot{u} + \left(q^E + q\right)w - \left(r^E + r\right)v\right) \tag{3.26}$$

$$Y + mg\cos\theta\sin\phi = m\left(\dot{v} + \left(r^E + r\right)u - \left(p^E + p\right)w\right) \tag{3.27}$$

$$Z + mg\cos\theta\cos\phi = m\left(\dot{w} + \left(p^E + p\right)v - \left(q^E + q\right)u\right) \tag{3.28}$$

The moment equation of motion is given by:

$$\mathbf{G} = \dot{\mathbf{h}} + \boldsymbol{\omega} \times \mathbf{h} \tag{3.29}$$

Or, in component form, with the assumption of an axisymmetric rocket:

$$L = I_x\dot{p} - \left(I_y - I_z\right)qr \tag{3.30}$$

$$M = I_y\dot{q} - \left(I_z - I_y\right)rp - \dot{m}qx_e^2 \tag{3.31}$$

$$N = I_z\dot{r} - \left(I_x - I_y\right)pq - \dot{m}rx_e^2 \tag{3.32}$$

Where the terms $\dot{m}qx_e^2$ and $\dot{m}rx_e^2$ are the jet damping.

3.4. Magnus effect

The T-Minus Dart uses a spin around the longitudinal axis to obtain stability trough the gyroscopic effect. However, the spin induces an asymmetrical flow field about the angle of attack plane, this causes a force perpendicular to the lift force and a yawing moment. This characteristic is know as the Magnus effect. Although the Magnus force is only 1/100 to 1/10 of the (Sturek et al., 1978), the Magnus moment can be sufficient large to cause the rocket to become unstable. For example, this effect has caused about one-third of the flights during the development of the Tomahawk sounding rocket to become dynamic unstable (Curry and Uselton, 1967). Due to the design of the T-Minus Dart (slender body with fins), there are three independent phenomena present that contribute to the Magnus effect: the bare-body Magnus force, the Magnus effect due to body-fin interference and the Magnus effect due to fin base pressure. A fourth phenomenon, the Magnus effect due to canted fins, is also treated here because of the configuration of the validation vehicle, the VS-40. The four phenomena will be discussed separately because each one has its own centre of pressure land magnitude. At the end of this section, the phenomena will be merged into one, usable equation for estimation of the Magnus effect.

3.4.1. The bare-body Magnus force

The bare-body Magnus force is determined using the theory stated in (Martin, 1957). As shown in Figure 3.10, the asymmetrical boundary-layer displacement thickness will produce an effective body shape which bends away from the original body axis. The Magnus force produced by this displacement thickness will be determined by using slender body theory, the orientation of this force is perpendicular to the normal force against the spin as shown in Figure 3.11. The bending of the effective body shape will cause a cross flow in the plane of zero yaw. The velocity potential (in polar coordinates) for this flow along the body axis equals:

$$\Phi = Vx - V\left(\frac{\delta\Delta'}{\delta x}\right)\Big]_{\theta=\pi/2}\left(\frac{a^2}{R}\right)\sin\left(\frac{z}{a}\right) \tag{3.33}$$

where Δ' is the part of displacement thickeners which contributes to the Magnus effect and equals:

$$\frac{\delta\Delta'}{\delta x}\Big]_{\theta=\pi/2} = 6.575\left(\alpha_T\frac{V_r}{V}\right)\left(\frac{x}{a}\right)\left(\frac{\sqrt{vx/V}}{a}\right) \tag{3.34}$$

From this, the perturbation potential function is:

$$\phi = -6.575\alpha V_r\left(\frac{x}{a}\right)\left(\frac{\sqrt{vx/V}}{a}\right)\left(\frac{a^2}{R}\right)\sin\left(\frac{z}{a}\right) \tag{3.35}$$

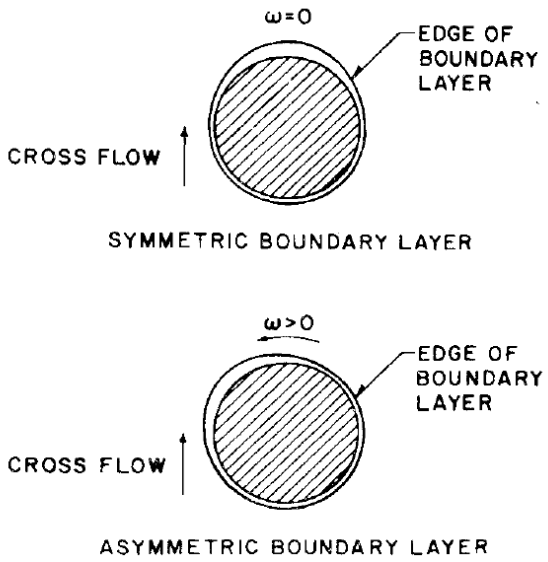

Figure 3.10: The change in effective body shape due to spin (Sturek et al., 1978).

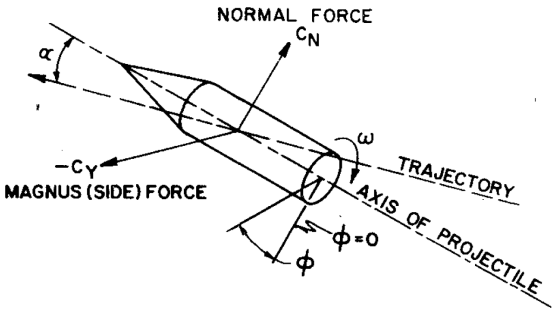

Figure 3.11: The bare-body Magnus force (Sturek et al., 1978).

The pressure coefficient equals:

$$C_p = \left(\frac{-2\phi_x}{V}\right) - \left(\frac{\phi_x^2}{V^2}\right) - \left(\frac{\phi_y^2}{V^2}\right) - \left(\frac{\phi_z^2}{V^2}\right) \tag{3.36}$$

or, to the first power in $\alpha V_r/V$,

$$C_p = 19.75\left(\alpha_T \frac{V_r}{V}\right)\left(\frac{\sqrt{\nu x/V}}{a}\right)\left(\frac{a}{R}\right)\sin\left(\frac{z}{a}\right) \tag{3.37}$$

The potential function in Z-direction has no influence on the pressure coefficient since the origin is along the body axis. Assuming a thin boundary layer, the pressure on the body can be found be evaluating Equation (3.37) on the surface of the body. Equation (3.37) reduces to:

$$C_p = 19.75\left(\frac{\alpha_T}{a}\right)\left(\frac{V_r}{V}\right)\left(\sqrt{\nu x/V}\right)\sin\left(\frac{z}{a}\right) \tag{3.38}$$

The Magnus force per unit length equals:

$$F = 2\bar{q}_0 \int_0^{\pi} C_p a \sin\left(\frac{z}{a}\right) d\left(\frac{z}{a}\right) \tag{3.39}$$

The total Magnus force is now

$$\begin{aligned} F_M &= \int_0^l F dx \\ &= 13.15\pi\bar{q}_0\left(\alpha_T \frac{V_r}{V}\right) l\sqrt{\frac{l\nu}{V}} \end{aligned} \tag{3.40}$$

Since, the displacement thickness at zero yaw is

$$\Delta_0 = 1.721\sqrt{\frac{x\nu}{V}} \tag{3.41}$$

Equation (3.40) can be rewritten as:

$$F_{p\alpha} = 7.641\pi\bar{q}_0\left(\alpha_t \frac{V_r}{V}\right) l\delta_0^* \tag{3.42}$$

with $\delta_0{}^*$ the displacement thickness at the base for zero yaw. This relation indicates that the Magnus force is a linear function of $\delta_0{}^*$. Rewriting Equation (3.42) in coefficient form:

$$\begin{aligned} C_{F_{p\alpha}} &= 6.001\left(\frac{l}{d}\right)\left(\frac{\delta_0^*}{d}\right) \\ &= 10.33\frac{(l/d)^2}{\sqrt{Re}} \end{aligned} \tag{3.43}$$

The solution in Equation (3.43) only give good results for small small angles. In order to obtain a solution for large angles of attack, the following solution can be derived (Milton, 1974) :

$$C_{F_{p\alpha}} = k\frac{2}{\pi}\left(\frac{l}{d}\right)^2 \tan\alpha_T (\sin\alpha_T)^{3/4}\left(\frac{Vd}{\nu}\right)^{\frac{-1}{4}} \tag{3.44}$$

where $k = 10$ is a experimentally determined value. This relation is validated using wind tunnel data and has a derivation for angles of attack below or equal to 4 degrees of 1 % and for angles between 4 and 10 degrees of 10 % (Oh et al., 2009). Finally, the centre of pressure for the Magnus force is located at (Martin, 1957)

$$\bar{x} = \frac{\int_0^l xF dx}{\int_0^l F dx} \tag{3.45}$$

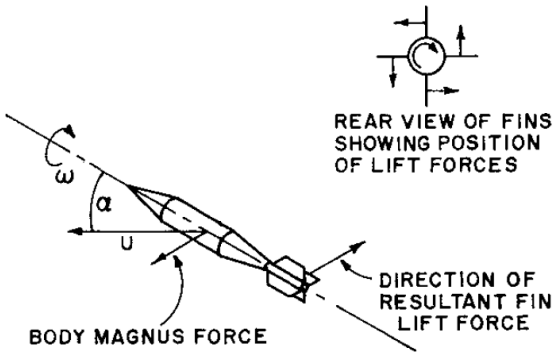

Figure 3.12: Fin force due to spin Platou (1965).

3.4.2. The Magnus effects due to body-fin interference

When there are fins aligned on the body of the rocket, the lift force on each fin contributes toward a torque about the centreline of the body which tends to retard the rotation. The lift force on each fin is perpendicular to the surface, and at an angle of attack of zero degrees, the opposite fins cancel one another. However, when there is an angle of attack that is not zero, the body interference is such that the lift force on the upper fin is reduced, resulting in a unbalanced force. The body and fin Magnus forces oppose one another, but act in a different centre of pressure. This results in a moment couple equal to the lesser of the two forces multiplied by the distance between the two forces (see Figure 3.12). The Magnus moment about the centre of gravity of the rocket will be the sum of the couple plus the moment due to the unbalanced Magnus force. For an axisymmetric rocket, the resultant lift force equals (Nielsen, 1960):

$$L = 2\pi\alpha_T s_m^2 \left(1 - \frac{a^2}{s_m} + \frac{a^4}{s_m^4}\right) \tag{3.46}$$

At small angles of attack only the inboard lift distribution is affected, and because of the symmetry about the angle-of-attack plane, produce a force perpendicular to the normal force against the spin. At larger angles of attack, the body wake will influence the outboard lift distribution and the resulting force will decrease to zero.

3.4.3. The Magnus effects due to fin base pressure

The base pressure can suddenly change on an thin fin ($t/c < 5\%$) when the following conditions are met: low supersonic Mach number, laminar boundary layer, thin trailing edge and small angle of attack (Chapman et al., 1952). For a flow over a rotating finned body, the angle of attack of two opposing fins can be written as:

$$\alpha_{left} = \alpha_b + \delta - (py/V) \tag{3.47}$$

$$\alpha_{right} = \alpha_b - \delta + (py/V) \tag{3.48}$$

These equations only hold when the fins are perpendicular to the body angle-of-attack plane (roll angle = 0 degrees). At another roll angle the fin angles oscillate between the left and right values, resulting in a continuously changing angle of attack on each fin. If the critical angle of attack is between the left and right hand values, then the fin base pressure will change as the fins rotate. This will create a Magnus moment, positive with the roll rate (Platou, 1965):

$$C_{M_{p\alpha}} = \frac{\left[\left(p_b/p_\infty\right)_R - \left(p_b/p_\infty\right)_L\right] Sbp_\infty}{\bar{q}\pi(d^2/4)d(pd/2V)\alpha_b} \tag{3.49}$$

This moment results in a moment larger than the fin-body interference moment. However, the unequal fin base pressure moment can be discarded if the conditions stated before are not met. For example, by increasing the thickness of the fins so that the boundary layer tips over the fins leading edge.

3.4.4. The Magnus effects due to canted fins

This mechanism for Magnus moments as treated below does not depend on interference but rather on the normal forces on the two wing panels which are incapable of contributing to any other Magnus effects. It is

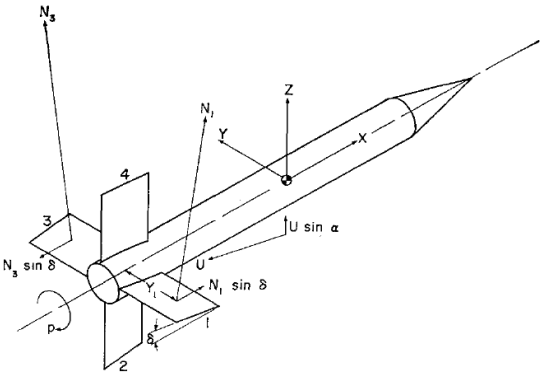

Figure 3.13: Nomenclature and origin of present Magnus moment (Benton, 1964).

assumed that the basic fins to be rolling at the steady-state rolling velocity. This velocity is determined by an exact balance between the roll-damping moment and the rolling moment induced by the fins. Looking at Figure 3.13, the total moment due to the first fin equals (Jacobson and Yaggy, 1973):

$$N_1 y_1 = \int_{D/2}^{b//2} \bar{q} C_{N_\alpha} \left(\alpha - \delta + \frac{py}{V}\right) dy \tag{3.50}$$

And the moment due to the third fin equals:

$$N_3 y_3 = \int_{D/2}^{b//2} \bar{q} C_{N_\alpha} \left(\alpha + \delta + \frac{py}{V}\right) dy \tag{3.51}$$

The total moment equals then:

$$M_{p\alpha} = -2\bar{q} C_{N_\alpha} \alpha_b d^3 \delta \tag{3.52}$$

And the Magnus moment coefficient:

$$C_{M_{p\alpha}} = -8/\pi \left(\frac{\omega d}{2\delta V}\right)^{-1} C_{N_\alpha} \tag{3.53}$$

3.4.5. Overview

The Magnus force and moment coefficient can be determined from all the components above by adding the relevant phenomena together. However in order to accurately model these coefficients, the aerodynamic coefficients and their origin need to be known. The aerodynamics coefficients and its location can be modelled using Missile DATCOM but the origin of the Magnus force and moment need to be determined from wind tunnel measurements. Looking at Equation (3.45), the origin of the bare-body Magnus moment changes at every instant during flight. Therefore, using the slender body theory, an estimation of the Magnus force and moment coefficients and its orientation divided in components can be derived. The components are shown in Table 3.1. For instance the Magnus force coefficient in Y-direction can be determined as the product between the derivatives in angle of attack and spin rate.

$$F_{p_\alpha} = \left(\frac{2\pi}{3} \alpha \frac{pb}{2V}\right) \bar{q} S \tag{3.54}$$

3.5. External forces and moments

3.5.1. Gravity

Since the software needs to be able to simulate a trajectory close to the Earth, the gravitational pull can not be considered to be a third-body perturbation. The Earth is modelled as a body of finite dimensions with an inhomogeneous mass distribution. The gravitational potential for the Earth can be expressed as the summation of a central field term, representing a mass-symmetric body, and a correction term for the Earth‘s

Table 3.1: Magnus coefficients components for a slender cruciform rocket (Nielsen, 1960)

	Y	Z	L	M	N
α	$\frac{2\pi}{3}\left(\frac{pb}{2V}\right)$	–	–	- -	$\frac{-\pi}{9A}\left(\frac{pb}{2V}\right)$
β	–	$\frac{-2\pi}{3}\left(\frac{pb}{2V}\right)$	–	$\frac{-\pi}{9A}\left(\frac{pb}{2V}\right)$	–
p	$\frac{2\pi}{3}\alpha$	$\frac{-2\pi}{3}\beta$	–	$\frac{-\pi}{9A}\beta$	$\frac{-\pi}{9A}\alpha$

non-symmetric mass distribution in the form of an appropriate spherical harmonic expansion (Mooij, 2015):

$$U = -\frac{GM_E}{\Re} + U_c\left(\Re, \mu, \lambda\right) \tag{3.55}$$

U_C can be written as (Vallado, 2001):

$$U_c\left(\Re, \mu, \lambda\right) = \frac{GM_E}{\Re}\left\{\sum_{n=2}^{\infty}\left[\left(\frac{\mathrm{R}_e}{\Re}\right)^n J_n P_n^0\left(\cos\theta\right) + \sum_{m=1}^{n}\left(C_{nm}\cos m\mu + S_{nm}\sin m\mu\right)P_n^m\left(\cos\theta\right)\right]\right\} \tag{3.56}$$

where θ is the co-latitude, J_n are the zonal harmonic coefficients, P_n^m are Legendre polynomials and C_{nm} and S_{nm} are tesseral coefficients for $n \neq m$ and sectoral harmonic coefficients for $n = m$. The gravitational acceleration is defined as:

$$\mathbf{g} = \begin{pmatrix} g_\Re & g_\mu & g_\lambda \end{pmatrix}^T = \begin{pmatrix} -\frac{\partial U}{\partial \Re} & -\frac{1}{\Re\cos\lambda}\frac{\partial U}{\partial \mu} & -\frac{1}{\Re}\frac{\partial U}{\partial \lambda} \end{pmatrix}^T \tag{3.57}$$

with

$$\frac{\partial U}{\partial \Re} = \frac{GM_E}{\Re^2}\left\{1 + \sum_{n=2}^{n_{\max}}\left[\left(\frac{\mathrm{R}_e}{\Re}\right)^n \sum_{m=0}^{n}\left(C_{nm}\cos m\mu + S_{nm}\sin m\mu\right)\times(n+1)\,\bar{P}_n^m\left(\sin\lambda\right)\right]\right\} \tag{3.58}$$

$$\frac{\partial U}{\partial \mu} = \frac{GM_E}{\Re}\sum_{n=2}^{n_{\max}}\left(\frac{\mathrm{R}_e}{\Re}\right)^n \sum_{m=0}^{n}\left(S_{nm}\cos m\mu - C_{nm}\sin m\mu\right)\bar{P}_n^m\left(\sin\lambda\right) \tag{3.59}$$

$$\frac{\partial U}{\partial \lambda} = \frac{GM_E}{\Re}\sum_{n=2}^{n_{\max}}\left(\frac{\mathrm{R}_e}{\Re}\right)^n \sum_{m=0}^{n}\left(C_{nm}\cos m\mu + S_{nm}\sin m\mu\right)\frac{\partial \bar{P}_n^m\left(\sin\lambda\right)}{\partial \lambda} \tag{3.60}$$

In Section 3.2.1, it is stated that the Earth is a spheroid body. This means that in Equation 3.57, $n = m = 0$ can be assumed. In this case the summations start at $n = 2$ and do not contribute so that:

$$\frac{\partial U}{\partial \Re} = \frac{GM_E}{\Re^2} \tag{3.61}$$

$$\frac{\partial U}{\partial \mu} = \frac{\partial U}{\partial \lambda} = 0 \tag{3.62}$$

3.5.2. Wind

The wind profile is imported in the software using a look-up table. This is deliberately done to provide flexibility in the software. The values can be measured on the launch day and can be inserted in the software. The wind profile is measured in the vehicle centred reference frame and needs to be transformed to the body-fixed reference frame by:

$$\begin{bmatrix} u_{wind} \\ v_{wind} \\ w_{wind} \end{bmatrix} = \mathbf{C_{vb}} \begin{bmatrix} V_{X_{wind}} \\ V_{Y_{wind}} \\ V_{Z_{wind}} \end{bmatrix} \tag{3.63}$$

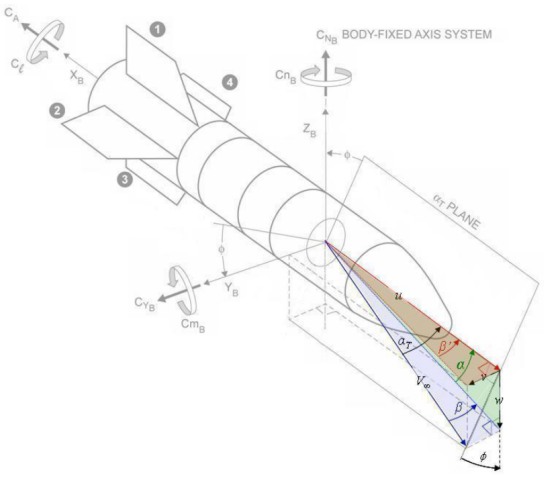

Figure 3.14: Aerodynamic coefficients. (Blake et al., 2011)

3.5.3. Aerodynamics

Because the rocket travels through an atmosphere, it will be subjected to aerodynamic forces and moments. These forces and moments are defined in the body-fixed reference frame. The forces depend on the dynamic pressure, reference area and aerodynamic force coefficients, whereas the moments depend on the dynamic pressure, reference area, aerodynamic moment coefficients and reference length. The roll and yaw moment are dependant on a longitudinal reference length and the pitch moment is dependant on a lateral reference length. However, since the rocket is axisymmetric, it can be assumed that the longitudinal and lateral reference length are equal. The force and moment equations then equal:

$$\text{Axial force: } F_x = C_X \bar{q} S_{ref} \tag{3.64}$$

$$\text{Side force: } F_y = C_Y \bar{q} S_{ref} \tag{3.65}$$

$$\text{Normal force: } F_z = C_Z \bar{q} S_{ref} \tag{3.66}$$

$$\text{Roll moment: } L = C_l \bar{q} S_{ref} b \tag{3.67}$$

$$\text{Pitch moment: } M = C_m \bar{q} S_{ref} b \tag{3.68}$$

$$\text{Yaw moment: } N = C_n \bar{q} S_{ref} b \tag{3.69}$$

The aerodynamic coefficients in Equations (3.64) to (3.69) are determined using the equations stated in (Siouris, 2004) and (Baranowski, 2013) and adapted to fit (Rosema et al., 2011) and (Nielsen, 1960). These papers described the aerodynamic coefficients and their derivatives and how to fit them into the force and moment equations. The outcome of these papers is defined in Equation (3.70) to (3.75). These coefficients are a function of the angle of attack, Reynolds number and Mach number and are determined using Missile Datcom and Table 3.1. The coefficients are defined below and shown in Figure 3.14:

$$C_X = -C_A \tag{3.70}$$

$$C_Y = C_{Y_\beta}\beta - C_{Y_{\alpha p}} \frac{pb}{2V}\alpha \tag{3.71}$$

$$C_Z = -C_{N_\alpha}\alpha + C_{Y_{\alpha p}} \frac{pb}{2V}\beta \tag{3.72}$$

$$C_l = C_{ll} + C_{ll_b} \frac{pb}{2V} \tag{3.73}$$

$$C_m = C_{m_\alpha}\alpha + \left(C_{m_q} + C_{m_{\dot{\alpha}}}\right) \frac{qb}{2V} + C_{N_{\alpha p}} \frac{pb}{2V}\beta \tag{3.74}$$

$$C_n = C_{n_\beta}\beta + \left(C_{n_r} r + C_{n_p} p\right) \frac{b}{2V} + C_{N_{\alpha p}} \frac{pb}{2V}\alpha \tag{3.75}$$

The coefficients in Equation (3.70) to (3.75) are a function of Mach number and angle of attack. In the software, the corresponding coefficient in determined using a two-dimensional look-up table.

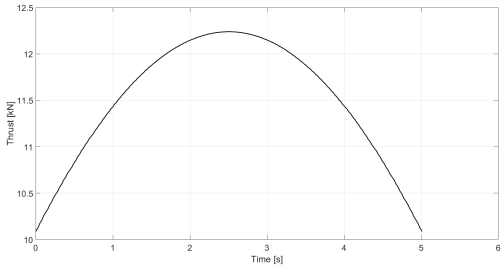

Figure 3.15: Thrust profile for the T-Minus Dart[2]

3.5.4. Thrust

The thrust profile is determined on forehand and is inserted as a look-up table in the software. The thrust is defined in the body-fixed reference frame, positive in negative X-direction. The thrust is determined as a function over time and expressed in a time step of 0.03 seconds. The magnitude of the thrust is shown in Figure 3.15.

3.5.5. Launch tower constraints

The rocket is launched using a launch tower, this constraints the initial movement of the rocket and provides the rocket with a spin rate. After launch, the rocket travels along the launch tower limiting the movement of the rocket along the X-axis in the boy-fixed reference frame. This ensures that the rocket is launched at the desired elevation angle in the desired direction. The launch tower also provides the rocket with an initial spin rate. It rotates the rocket over 270 degrees along the X-axis in the body-fixed reference frame when in the tower and restricting angular accelerations in the Y and Z-axis in the body-fixed reference frame. The angular accelerations of the rocket in the body-fixed reference frame are defined by:

$$dp = \frac{3\pi}{2}\left(\frac{2l_{tower}}{\frac{T}{m} - \frac{g}{\cos(\frac{\pi}{2}-\lambda)}}\right)^{-1} \tag{3.76}$$

$$dq = 0 \tag{3.77}$$

$$dr = 0 \tag{3.78}$$

[2]Private communication, T-Minus Engineering, 01/11/2016

4

Software Description

In this chapter, the software is described. Firstly, an overview of the program is given in Section 4.1. The numerical integrator and interpolator used in the program is stated in Section 4.2. The verification and pseudo-validation is treated in Section 4.3 and 4.4. Finally, the tool is use to determine the stability of the T-Minus Dart in Section 4.5.

4.1. Program Description

4.1.1. Block diagram

An overview of the program is given in Figure 4.1, it shows the different steps the programs takes to simulate the trajectory of the rocket. The program starts from an initial state (launch configuration) and uses the Dormand–Prince (RKDP) method to obtain the updated state variables from the equations of motion and the aerodynamic coefficients. The program stops when the altitude of the rocket reaches zero, this is checked by the change in sign of the Z-coordinate. The flow diagram for the software is given in Figure 4.2, it shows the different Matlab files that are used in the simulation and the order in which they are used.

4.1.2. Input

Aerodynamic coefficients

The aerodynamic coefficients needed to solve the Euler's force and moment equations are determined using Missile Datcom. This program is commonly used for determining the aerodynamic coefficients suitable for preliminary design. The methods used for determining the aerodynamic coefficients are stated in (Blake et al., 2011). The input files for the T-MINUS Dart in boosted and coasting configuration are given in Appendix B.1 and B.2 respectively. The coefficients that are used in the software are stated in Section 3.5.3. The coefficients are determined as a function of Mach number and angle of attack as shown for the axial force coefficient in Figure 4.3. To find the coefficients for the corresponding Mach number and angle of attack, the values are interpolated using a cubic spline function.

Vehicle configuration

The vehicle configuration gives the vehicle parameters in function of time for the booster and are constant for the Dart. These vehicle parameters are the thrust, mass and moments of inertia in function of time[1]. For the coasting phase of the flight, these parameters are constant and shown in Table 4.1. These parameters are constant because there is no thrust, jettisoning of parts or change in configuration of the rocket. Note that these parameters reflect on the T-Minus Dart with modified nose.

4.1.3. Output

The software gives an output file as shown in Table 4.2: X, Y, and Z components of the position and velocity, the roll, pitch and yaw rates and finally the four elements of the quaternion describing the rockets rotational position. The position of the rocket is defined in the vehicle-centred vertical reference frame and the momentum vectors are defined in the body-fixed reference frame. The four elements of the quaternion describing

[1] Private communication, T-Minus Engineering

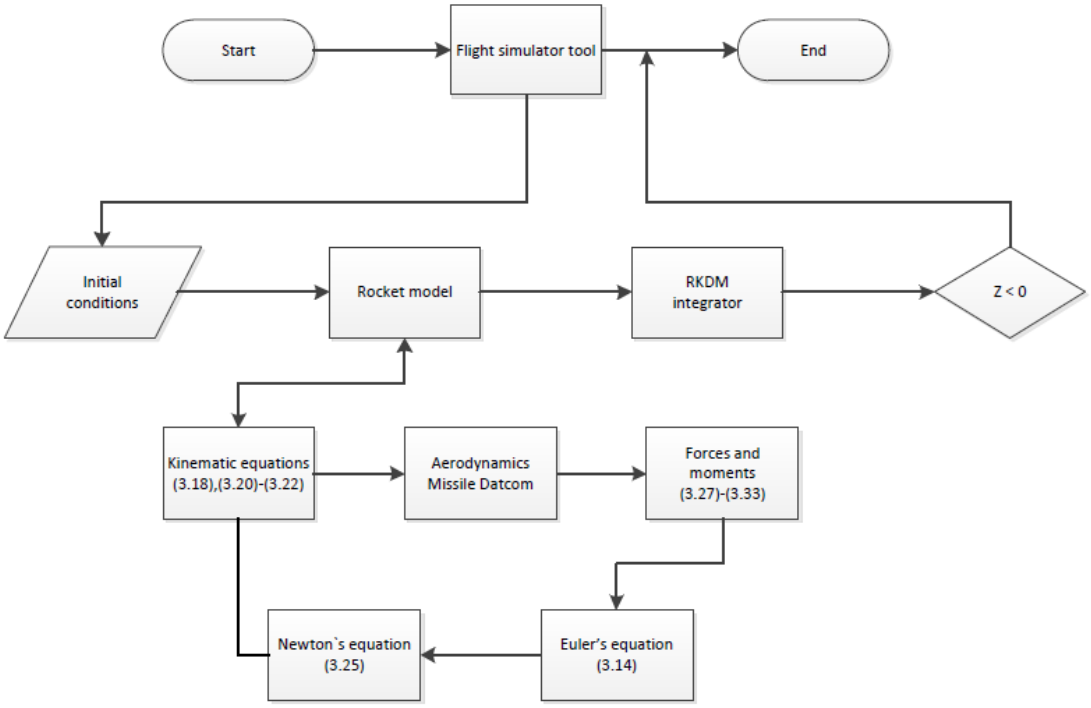

Figure 4.1: Code block diagram for the flight simulator tool

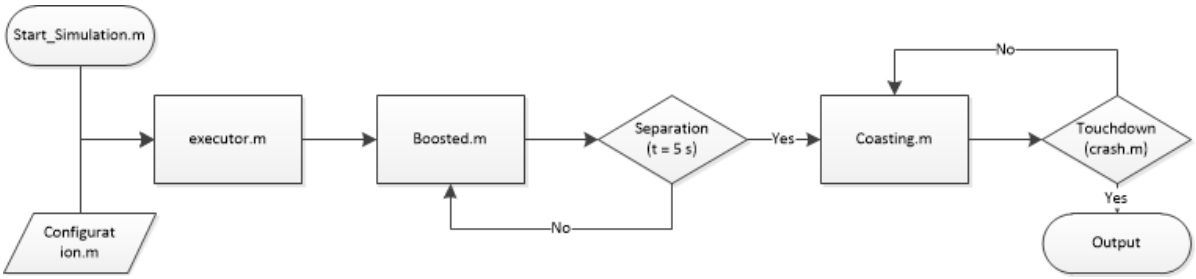

Figure 4.2: Functional flow diagram of the software

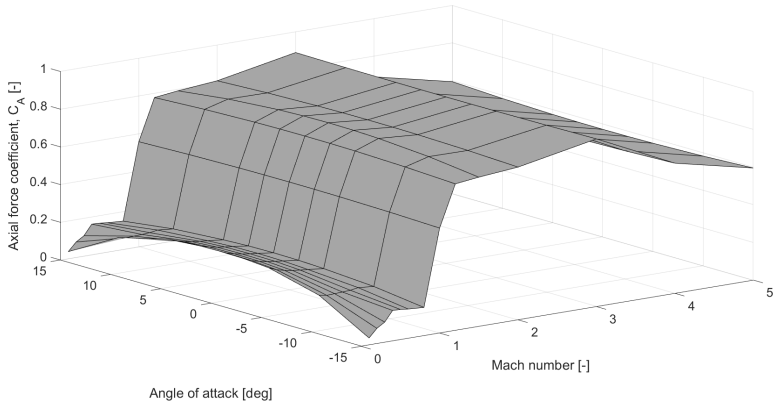

Figure 4.3: Axial force coefficient

Table 4.1: Vehicle configuration file for the coasting phase of the T-Minus Dart[2]

Thrust [N]	Mass [kg]	$I_{yy} = I_{zz}$ [kg · m^2]	I_{zz} [kg · m^2]
0	3.485	6.54E-04	2.42E-01

Table 4.2: Output of the software

Column	Parameter	Unit
1	Time	s
2	Easterly positive position from launch site	m
3	Northerly positive position from launch site	m
4	Altitude above the surface of the Earth	m
5-7	Rockets linear momentum vector	m s^{-1}
8-9	Rockets angular momentum vector	rad s^{-1}
10-14	The four elements of the quaternion describing the rockets rotational position	-

the rotational position of the rocket are also given in the output file, this is to easily transform the results between the reference frames.

4.2. Numerical methods

The numerical integration and interpolation used are defined by the use of the Matlab, *ode45* and *spline*, functions. The *ode45* function is an numerical integration method based on the Dormand–Prince method. The *spline* function is a cubic spline integrator.

4.2.1. Numerical integration

To solve the differential equations, a numerical integrator is needed. The method used here is the Dormand-Prince (RKDP) method (Dormand and Prince, 1980). The method compares two approximate solutions for each time step. if the two approximations are in close agreement, the solution is accepted. If the approximations do not meet the required accuracy, the step size, h, is decreased. On the other and if the solutions answers to more significant digits than required, the step size is increased. Each step size uses the following values:

$$k_1 = hf\left(t_k, y_k\right) \tag{4.1a}$$

$$k_2 = hf\left(t_k + \frac{h}{5}, y_k + \frac{k_1}{5}\right) \tag{4.1b}$$

$$k_3 = hf\left(t_k + \frac{3}{10}h, y_k + \frac{3}{40}k_1 + \frac{9}{40}k_2\right) \tag{4.1c}$$

$$k_4 = hf\left(t_k + \frac{4}{5}h, y_k + \frac{44}{45}k_1 - \frac{56}{15}k_2 + \frac{32}{9}k_3\right) \tag{4.1d}$$

$$k_5 = hf\left(t_k + \frac{8}{9}h, y_k + \frac{1937}{6561}k_1 - \frac{25360}{2187}k_2 + \frac{64448}{6561}k_3 - \frac{212}{729}k_4\right) \tag{4.1e}$$

$$k_6 = hf\left(t_k + h, y_k + \frac{9017}{3168}k_1 - \frac{355}{33}k_2 + \frac{46732}{5247}k_3 + \frac{49}{176}k_4 - \frac{5103}{18656}k_5\right) \tag{4.1f}$$

$$k_7 = hf\left(t_k + h, y_k + \frac{35}{384}k_1 - \frac{500}{1113}k_3 + \frac{125}{1952}k_4 - \frac{2187}{6784}k_5 + \frac{11}{84}k_6\right) \tag{4.1g}$$

Then an approximation to the solution of the problem equals using a RK method of order 4:

$$y_{k+1} = y_k + \frac{5179}{57600}k_1 + \frac{7571}{16695}k_3 + \frac{393}{640}k_4 - \frac{92097}{339200}k_5 + \frac{187}{2100}k_6 + \frac{k_7}{40} \tag{4.2}$$

[2]Private communication, T-Minus Engineering

Table 4.3: Verification methods of software blocks

Software block	Method used
Aerodynamic coefficient database	Compare with in-house software and check implementation in equations of motion
Aerodynamic forces	Check with unit test
Aerodynamic moments	Check with unit test
Atmosphere model	Compare values with (National Oceanic and Atmospheric Administration, 1976)
Gravitational acceleration	Compare values with manual calculations
Input files	Check if all files and values have the desired input and contains no irregularities
Interpolator	Test with manual calculations
Integrator	Test with manual calculations
Rotational equations of motion	Check with unit test
Translational equations of motion	Check with unit test
Transformations between reference frames	Check quaternions with unit transformations
Wind	Compare data from input with output data

A better value for the solution is determined using a RK method of order 5:

$$z_{k+1} = y_k + frac35384k_1 + \frac{500}{1113}k_3 + \frac{125}{192}k_4 - \frac{2187}{6784}k_5 + \frac{11}{84}k_6 \tag{4.3}$$

The optimal step size can be determined by multiplying the scalar s times the current step size. The scalar s equals:

$$s = \left(\frac{\epsilon h}{2\left|z_{k+1} - y_{k+1}\right|}\right)^{1/4} \tag{4.4}$$

where ϵ is the specified error control tolerance. The error control tolerance defines the magnitude of the next step. The larger the error, the larger the time step will be.

4.2.2. Numerical interpolation

To accurately interpolate between two variables in a table, a cubic spline function is used. The cubic spline function is particularly useful when interpolating between two altitudes in the US76 atmospheric model. It is possible to determine the second derivatives if the continuity of the first derivative is required (Press, 2007). If one needs to find a value between x_j and x_{j+1}, the cubic spline function equals (Press, 2007):

$$f(x) = Af(x_j) + Bf(x_{j+1}) + Cf''(x_j) + Df''(x_{j+1}) \tag{4.5}$$

Where

$$A = \frac{x_{j+1} - x}{x_{j+1} - x_j} \tag{4.6}$$

$$B = 1 - A \tag{4.7}$$

$$C = \frac{1}{6}(A^3 - A)(x_{j+1} - x_j)^2 \tag{4.8}$$

$$D = \frac{1}{6}(B^3 - B)(x_{j+1} - x_j)^2 \tag{4.9}$$

4.3. Verification

4.3.1. Case 0: unit level

Firstly, the software is tested at unit level by testing the different code blocks. An overview of the code blocks tested and the method used is shown in Table 4.3. The unit test consist of calculations with the equations stated in Section 3.3.3 and 3.5.3. The values are manually inserted in the equations and compared to the output of the program.

Table 4.4: Tower constraints, output file software.

Time [s]	X [m]	Y [m]	Z [m]	u [m/s]	v [m/s]	w [m/s]	p [rad/s]	q [rad/s]	r [rad/s]
0	0	0	0	0	0	0	0	0	0
0.025	10^{-18}	10^{-17}	0.08	6.62	10^{-17}	10^{-17}	15.60	0	0
0.05	10^{-18}	10^{-17}	0.33	13.29	10^{-17}	10^{-17}	31.32	0	0
0.075	10^{-18}	10^{-17}	0.75	20.01	10^{-17}	10^{-17}	47.15	0	0
0.10	10^{-18}	10^{-17}	1.33	26.78	10^{-17}	10^{-17}	54.38	10^{-19}	10^{-19}
0.125	10^{-18}	10^{-17}	2.09	33.59	10^{-17}	10^{-17}	54.20	10^{-19}	10^{-19}
0.15	10^{-18}	10^{-17}	3.01	40.46	10^{-17}	10^{-17}	54.20	10^{-19}	10^{-19}

4.3.2. Case 1: no environment and no events

The first case is to test whether there are no changes in the state that are not the result of interaction with the environment or due to external events. In order to check this the atmosphere, the gravity field, the rotation of the Earth and the propulsion forces are set to zero. Furthermore, all initial conditions are set to zero. The expected outcome is that the aerodynamic forces and moments remain zero and as a result of this the state derivative will be zero, resulting in a constant state. Implementation of the above conditions give a rocket resting in the launch tower, all the output variables are zero as expected.

4.3.3. Case 2: tower restraints

This case test whether the launch tower is correctly implemented in the software. The case can be divide in two parts: the behaviour of the rocket in the tower (constraints) and the expected outcome when the rocket leaves the tower.

Tower constraints

When the rocket is in the tower, its trajectory is predetermined by the tower. The rocket travels along the tower at a predetermined launch angle. Since the launch tower is 3.4 meters long, the output is checked for a travelled distance below 3.4 meters. The constraints of the tower are the determined trajectory and the absence of wind influences in the tower. Looking at the output (Table 4.4), it can be seen that the first part of the trajectory (under 3.4 meters) has no influence of the wind as expected. Furthermore, it can be seen that the only acceleration to which the rocket is subjected in the X_b-direction. If, rocket is launched at an elevation of 90 degrees, the only displacement and velocity is along the X_b-axis. The others values in the order 10^{-19} are a result of the numerical integration, this is the noise of the program.

Tower output

The rocket leaves the tower with a roll rate of around 55 rad·s^{-1}, this is expected since the tower rotates the rocket over 270 degrees in a time interval of 0.15 seconds. This means that the software gives the rocket the desired acceleration around the X_b-axis. The pitch and yaw rates are zero (except for the noise) as defined in Section 3.5.5.

4.3.4. Case 3: straight up and down

In this case, the software is checked if there are no singularities in the rotations and whether the aerodynamic model functions at large angles of attack. A flight where the rocket is launched straight up (elevation of 90 degrees) is simulated to check this without any external forces and moments and no rotation of the Earth. In the first simulation there is no atmosphere present, this should give a trajectory straight up and down. The rocket should land at the exact spot from where it is launched. In the second simulation the atmosphere is present, a small disturbance will affect the rotational equilibrium. Assuming the rocket to be aerodynamically stable, the angle of attack and sideslip should converge to zero again after apogee. When the rocket rotates, there will be a lift component in the horizontal plane and thus a movement in the horizontal plane.

No atmosphere present

The mathematical relations for a vertical ascent in vacuum with constant thrust are given by (Naeije and

Table 4.5: Verification values for case 3: straight up and down

Parameter	Calculated Value	Simulated value
V [m s^{-1}]	2239.7	2239.7
Z [m]	4572.1	4572.1
ΔX [m]	0	0

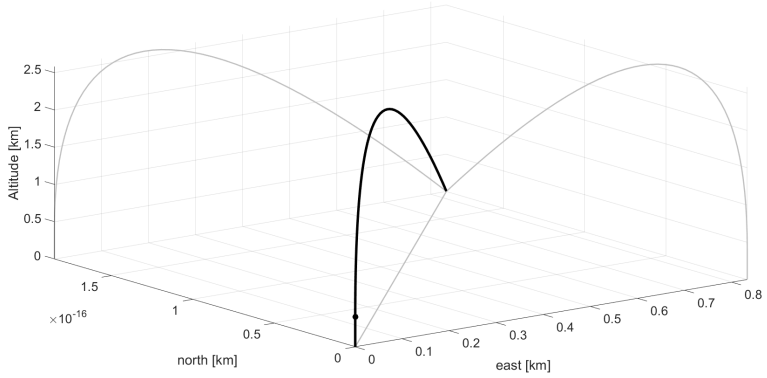

Figure 4.4: Trajectory of verification case 3 with an atmosphere present.

Mooij, 2016):

$$V = \frac{c_{eff}}{\Psi_0}\left(\Psi_0 \ln\Lambda - 1 + \frac{1}{\Lambda}\right) \tag{4.10}$$

$$Z = \frac{c_{eff}^2}{g_0\Psi_0}\left(1 - \frac{1+\ln\Lambda}{\Lambda} - \frac{\left(1-\frac{1}{\Lambda}\right)^2}{2\Psi_0}\right) \tag{4.11}$$

The calculated values and the output of the program are compared in Table 4.5. Looking at the values one can see that the software produces the desired outcome. The rocket flies straight up and has no horizontal movement. The translational equations of motion produce the correct outcome.

An atmosphere present
The software should produce a horizontal movement when the atmosphere is present. The smallest numerical disturbance will disturb the rotational equilibrium, resulting in a lift component in the horizontal plane. The consequence of this, is that there is a movement in the horizontal plane. Figure 4.4 shows the trajectory of this verification case. The horizontal movement can be seen in eastward direction, this is due to the change in orientation at apogee. The rocket rotates 180 degrees and this gives the displacement in eastward direction. The movement in northward direction is a result of the numerical noise.

4.3.5. Case 4: basic cases

Here, the software is subjected to standard mathematical cases where the results can be compared with manual calculated values.

Constant altitude (orbit around Earth)
This case is to check when the rocket travels, in absence of the atmosphere but with a constant gravitational acceleration, remains at a constant altitude. Assuming the rocket travels at an altitude of 640 kilometres above the surface at the Earth, its speed to remain in orbit equals:

$$V = \sqrt{\frac{GM_E}{r}} = \sqrt{\frac{\left(6.67\cdot10^{-11}\right)\cdot\left(5.98\cdot10^{24}\right)}{6.38\cdot10^6 + 640000}} = 7.54\cdot10^3 \text{m/s} \tag{4.12}$$

Inserting these values in the software gives the following values after a flight time of 5 seconds (see Table 4.6).This means the rocket stays at the initial altitude and has a constant velocity as expected.

Table 4.6: Verification values for case 5: constant altitude

Parameter	Value
ΔX [m]	9.5×10^{-12}
ΔZ [m]	-7.8×10^{-5}
Δu [m s^{-1}]	0
Δw [m s^{-1}]	0.0098

Table 4.7: Verification values for case 5: only drag acting on the rocket

Parameter	Value 3 DOF	Value 6 DOF	Error
X	1.718 m	1.719	0.04 %
Z	3768.984m	3765.8	0.08 %
V	2127.158m/s	2127.03	0.005 %

Only drag acting on the rocket
In this case, the rocket operates in a rotating atmosphere in an exponential gravity field but is only subjected to one aerodynamic force (drag) and no aerodynamic moments. The benchmark used for this test is a simple 3 degrees-of-freedom (DOF) simulation developed at T-Minus Engineering which operates in the XZ plane. The 3 DOF software gives the values in spherical coordinates, so they are converted using the following relations to obtain it in Cartesian coordinates (Mulder et al., 2013):

$$x = R \sin\tau \cos\delta \tag{4.13}$$

$$y = R \sin\tau \sin\delta \tag{4.14}$$

$$z = R \cos\tau \tag{4.15}$$

And the velocity can be compared by transforming the body velocities by:

$$V = \sqrt{u^2 + v^2 + w^2} \tag{4.16}$$

Inserting these values in the software (and projecting in the XZ plane) gives the following values stated in Table 4.7.Again, it can be seen that the outcome of the simulation is as expected.

4.4. Pseudo-validation

To pseudo-validate the software, the outcome of the simulations is compared with the nominal trajectory of the Veículo de Sondagem (VS)-40[3]. The term pseudo-validate reflects on the fact that the validation is not done with data from a flown mission, but with data calculated for the nominal mission. The focus during the validation lies on the first 62 seconds of the trajectory. This is due to two main reasons: firstly, to check whether the launch tower constraints are accurately modelled in the software and secondly, this is the boosted phase of the flight. This will give us insight in the modelling of the position and velocity of the rocket and the angular rates of the rocket. The angular rates of this rocket need to be examined carefully, the rocket has a up-spinning motion around the X-axis and accurately modelling the angular rates will give us an accurate tool for determining the static and dynamic stability. The input file for determining the aerodynamic coefficients using Missile Datcom is stated in Appendix B.3.

4.4.1. Tower constraints

Looking at Table 4.8, the output of the simulation for the first 0.7 seconds, the influence of the constraints of the launch tower is shown. It shows that the rocket travels along the path of the tower and has no angular rates acting on it. The velocity in Y direction is also zero since the rocket is not subjected to out-of-plane displacement. This is expected as stated in Section 3.5.5.

4.4.2. Simulated flight

The simulated trajectory for the VS40 is shown in Figure 4.5, with the trajectory shown in black and the projections in the planes in grey. The output for the components for the position and velocity after 62 seconds is

[3]Private communication, E. Mooij

Table 4.8: Tower constraints for the VS40 from output file.

Time [s]	X [m]	Y [m]	Z [m]	u [m/s]	v [m/s]	w [m/s]	p [rad/s]	q [rad/s]	r [rad/s]
0	0	0	0	0	0	0	0	0	0
0.1	0	0	0	0	0	0	0	0	0
0.2	0.0012	0.0076	0.0049	0.2749	0	0.2730	0	0	0
0.3	0.0088	0.0555	0.0412	2.5366	0	0.4094	0	0	0
0.4	0.0253	0.1595	0.3647	5.7978	0	0.5459	0	0	0
0.5	0.0509	0.3217	1.0916	9.0503	0	0.6824	0	0	0
0.6	0.0858	0.5417	2.1375	12.2837	0	0.8189	0	0	0
0.7	0.1298	0.8195	3.5011	15.5033	0	0.9554	0	0	0

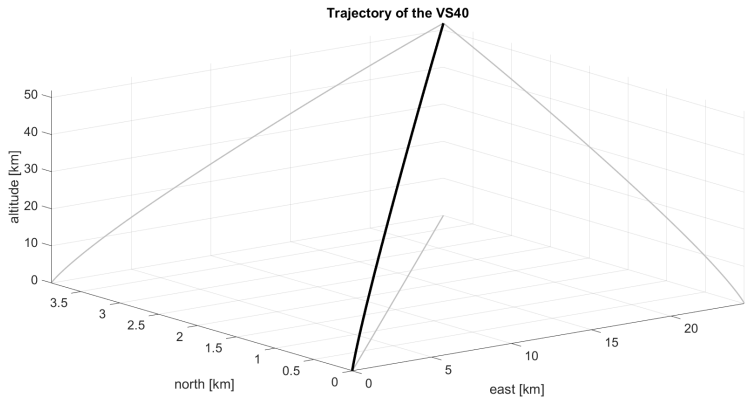

Figure 4.5: VS40 simulated trajectory

shown in Table 4.9. The difference between the simulated and the validation value is due to computational errors, the use of simplified equations for the gravity field, Earth and atmosphere and uncertainties in the input files. The errors in X- and Y-direction are approximately 5% and in Z-direction approximately 2%.The difference between the values can be explained by the assumptions made in the mathematical model used in the software and numerical accuracy.

Looking at the simulated angular rates shown in Figure 4.6, it is clear that the software produces an accurate output. The local differences are explained by the use of the aerodynamic coefficients. In pitch and yaw rate, these differences are more present than in the roll rate. This is explained by the error that comes with the use of Missile Datcom (Sooy and Schmidt, 2005) (Abney and McDaniel, 2005).

4.5. T-Minus Dart

The implementation of the enhanced radiation cooling design on the nose of the T-Minus Dart, changes the configuration of the rocket. The change from a conical to a spherical nose, can have an impact on the static and dynamic stability of the rocket. The new configuration of the rocket needs therefore be tested whether it

Table 4.9: Simulated results for the VS40

Parameter	Simulated value	Validation value
X	3.8779 km	3.811 km
Y	24.578 km	23.437 km
Z	51.8448 km	52.792 km
V_X	113.75 m $\cdot$ s^{-1}	113.077 m $\cdot$ s^{-1}
V_Y	701.62 m $\cdot$ s^{-1}	690.105 m $\cdot$ s^{-1}
V_Z	-1201.884 m $\cdot$ s^{-1}	-1322.2146 m $\cdot$ s^{-1}

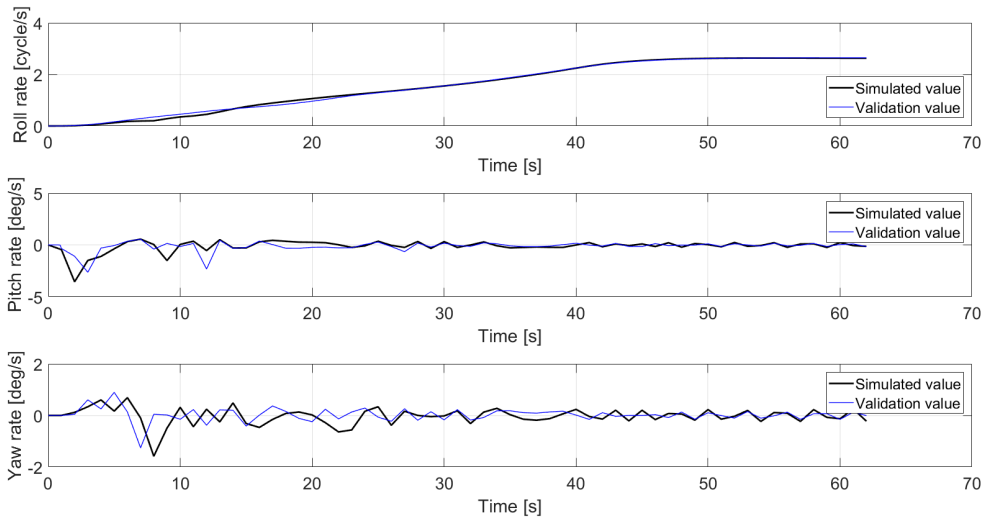

Figure 4.6: VS40 simulated angular rates

is static and dynamic stable. The new configuration of the T-Minus Dart is shown in Figure 4.7.

4.5.1. Stability study using linearised equations of motion

The stability considerations are studied using the eigenmotion of the rocket using the linearised equations of motion according to (Zipfel, 2000). The eigenmotion is determined using the state-space form of the perturbations of unsteady flight. The choice for analysing the eigenmotion in the unsteady flight is to include the angular velocities in the analysis. The equations needed to form the space-state form are determined using the small-disturbance theory (Etkin, 1972). To group the equations in two groups: equations regarding the longitudinal and lateral motion, the following assumptions are made:

- Regarding the longitudinal motion:
  1. The Earth is flat.
  2. There is at least one plane of symmetry.
  3. There is no presence of gyroscopic rotor effects.
- Regarding the lateral motion:
  1. The Earth is flat.
  2. The equations of motion are linearised.
  3. There is no presence of gyroscopic rotor effects.
  4. The aerodynamic forces are decoupled.

With these assumptions, the state vectors can be composed. The longitudinal state vector is composed of u, p, r, ϕ and equals (Zipfel, 2000) :

$$\begin{bmatrix} \dot{v} \\ \dot{p} \\ \dot{r} \\ \dot{\sigma} \end{bmatrix} = \begin{bmatrix} -\frac{\bar{q}S}{MV} C_{Y_\beta} & w & -w & g \\ \frac{\bar{q}Sb}{I_x V} C_{l_\beta} & \frac{\bar{q}Sb^2}{2I_x V} C_{l_p} & \frac{-I_z+I_y}{I_x} q + \frac{\bar{q}Sb^2}{2I_x V}\left(C_{l_r} + C_{l_\beta}\right) & 0 \\ \frac{\bar{q}Sb^2}{I_z V} C_{n_\beta} & \frac{-I_x+I_y}{I_z} q + \frac{\bar{q}Sb^2}{2I_z V} C_{n_p} & \frac{\bar{q}Sb^2}{2IzV}\left(C_{n_r} + C_{n_\beta}\right) & 0 \\ 0 & \cos\theta & \sin\theta & 0 \end{bmatrix} \times \begin{bmatrix} v \\ p \\ r \\ \sigma \end{bmatrix} \tag{4.17}$$

And the lateral state vector is composed of v, p, r, σ and equals (Zipfel, 2000) :

$$\begin{bmatrix} \dot{u} \\ \dot{w} \\ \dot{q} \\ \dot{\theta} \end{bmatrix} = \begin{bmatrix} -\frac{\rho VS}{M}\left(C_{A_r} + C_{N_r}\right) & -q & -w & -g\cos\theta \\ q & -\frac{qS}{MV} & u & -g\sin\theta \\ \frac{\rho VS}{I_y} C_{m_r} & \frac{\bar{q}Sb}{I_y V} C_{m_\alpha} & \frac{\bar{q}Sb^2}{2I_y V}\left(C_{m_q} + C_{m_{\dot{\alpha}}}\right) & 0 \\ 0 & 0 & 1 & 0 \end{bmatrix} \times \begin{bmatrix} u \\ w \\ q \\ \theta \end{bmatrix} \tag{4.18}$$

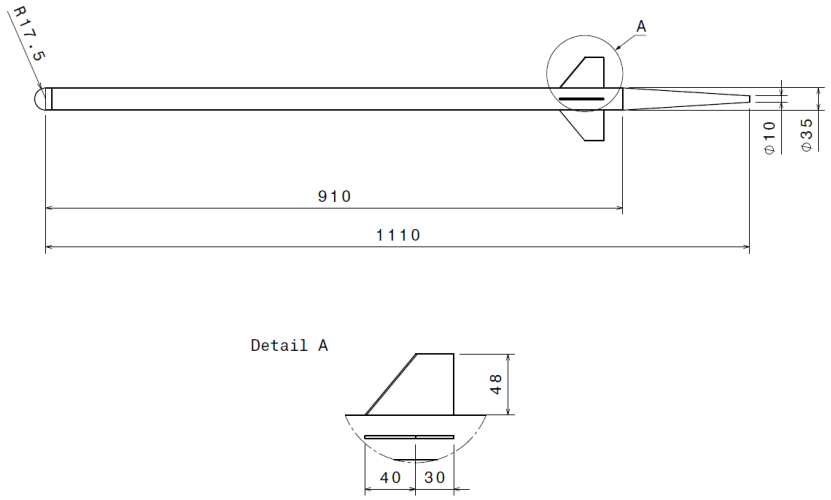

Figure 4.7: T-Minus Dart with enhanced radiation cooling subsystem

Where σ is the horizontal roll angle. The eigenmotion can be characterised by defining the period, P, the halving time, $T_{\frac{1}{2}}$, and the damping ration, ς:

$$P = \frac{2\pi}{\text{Im}(\lambda)} \tag{4.19}$$

$$T_{\frac{1}{2}} = \frac{\ln \frac{1}{2}}{\text{Re}(\lambda)} \tag{4.20}$$

$$\zeta = -\frac{\text{Re}(\lambda)}{\sqrt{\text{Re}(\lambda)^2 + \text{Im}(\lambda)^2}} \tag{4.21}$$

Mission launched at 30 degrees elevation
First, the trajectory of the rocket, launched at 30 degrees elevation is studied. The eigenvalues for translational motion are shown in Figure 4.8. The motion during the flight consists of two phases, the boosted and coasting phase. The coasting phase has two distinct motions: two longitudinal periodic motions and a aperiodic lateral motion. Zooming in on the origin of the system, one can see that during the boosted phase, there are three periodic motions. In order to identify the motions further, the periods during flight are stated in Figure 4.9, During the boosted phase, the motions are short period oscillations in both longitudinal and lateral direction. During the coasting phase, the damping ratio remains constant due to the absence of large variations in the aerodynamic forces. The periods of those motion are very small, the motions are identified as short period oscillation. All three motions have negative real parts, making these motions stable, meaning that the eigenmotion will be converging.

The eigenvalues for the rotational motion are shown in Figure 4.10, during the boosted phase the motions are all aperiodic (no imaginary part in the eigenvalues). The lateral rotation about the Z-axis is an unstable motion, the eigenmotion will be diverging. The other lateral motion about the X-axis is stable and the longitudinal motion is also stable. During the coasting phase, the longitudinal motions have become periodic, except at three instances during flight where there is no decoupling between the aerodynamic forces due to an error in the linearisation.

Mission launched at 85 degrees elevation
The eigenvalues for the translational motion is shown in Figure 4.11.The motion consists of two complex eigenvalues: a lateral and longitudinal oscillation. The motion reaches large eigenvalues when subjected to large aerodynamic forces and thus experiences a large dynamic pressure. The aperiodic and periodic eigenvalues all have negative real parts and are thus stable. The period for the lateral, translational motion has the

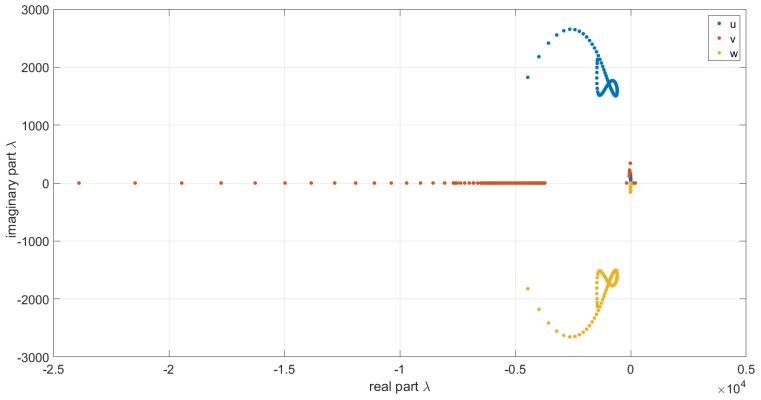

Figure 4.8: Eigenvalues for the translational motion for the rocket launched at 30 degrees elevation.

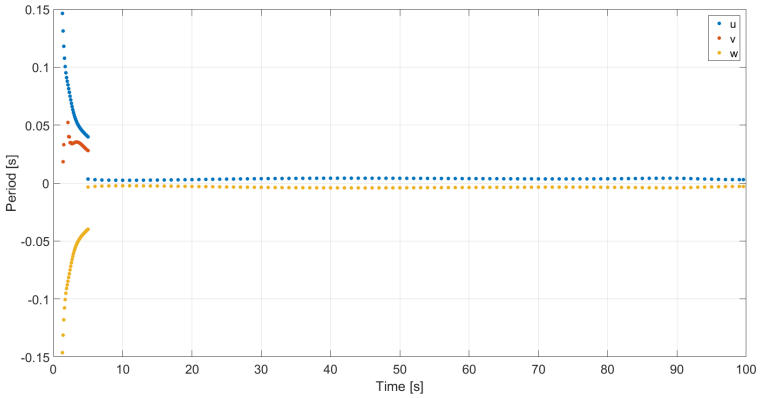

Figure 4.9: Periods for the translational motion for the rocket launched at 30 degrees elevation.

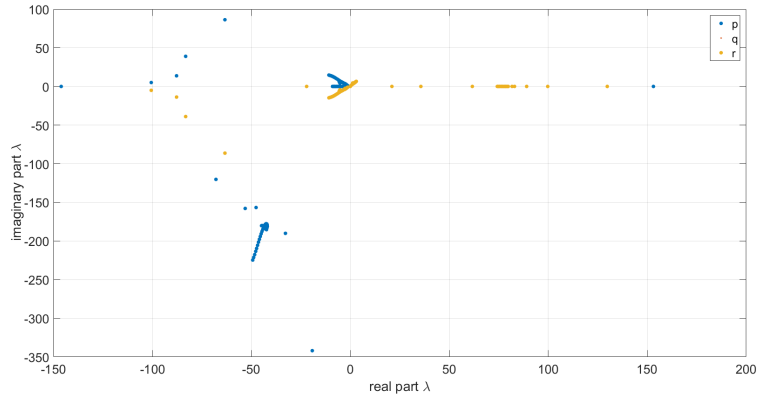

Figure 4.10: Eigenvalues for the rotational motion for the rocket launched at 30 degrees elevation.

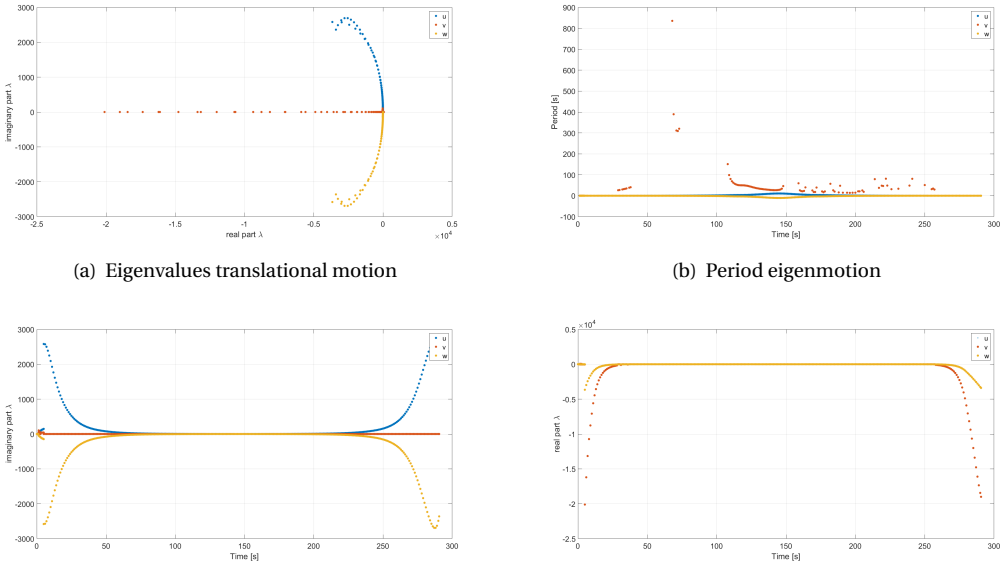

(a) Eigenvalues translational motion

(b) Period eigenmotion

(c) Imaginary part eigenvalues

(d) Real part eigenvalues

Figure 4.11: Translational eigenmotion and characteristics.

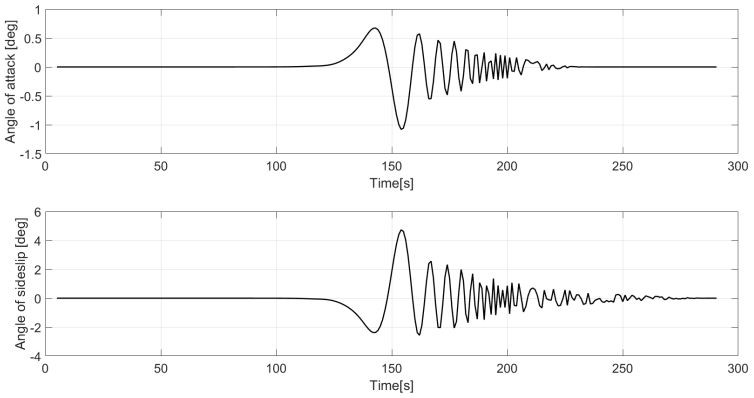

Figure 4.12: Variations in angle of attack and sideslip.

same behaviour as the longitudinal motions but is subjected to pitch rate when approaching apogee, resulting in the large period as shown in Figure 4.11. After apogee, the rocket is subjected to a damped angular motion, resulting in a converging angle of attack and sideslip (see figure 4.14. This is caused by the change in orientation of the rocket, resulting in an oscillating motion around the Y- and Z-axis.

The eigenvalues for the rotational motion are shown in Figure 4.13. The motion consist again of two periodic motions: a longitudinal and lateral oscillation when subjected to a large dynamic pressure in the first stage of the flight. When entering the higher atmosphere, the motions become aperiodic and remain aperiodic until the rocket entries the atmosphere again. The other rotation motion is aperiodic during the entire flight. All the eigenvalues have negative real parts, resulting in a stable motion. The oscillating motion during the initial descent phase is clearly visible in the pitch and yaw rate, as shown in Figure **??**. The motion about the yaw rate has a constant damping amplitude but has as increasing amplitude due to the increase in aerodynamic forces at the end of the flight

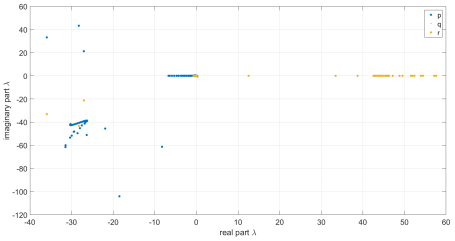

(a) Eigenvalues rotational motion

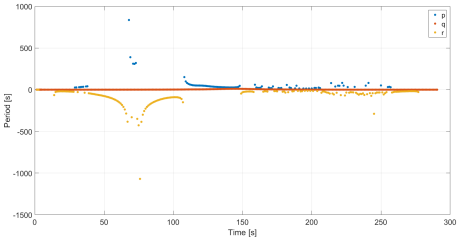

(b) Period eigenmotion

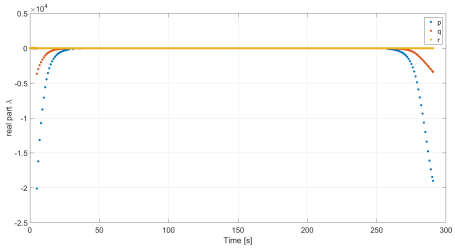

(c) Imaginary part eigenvalues

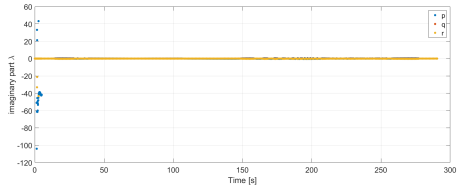

(d) Real part eigenvalues

Figure 4.13: Rotational eigenmotion and characteristics.

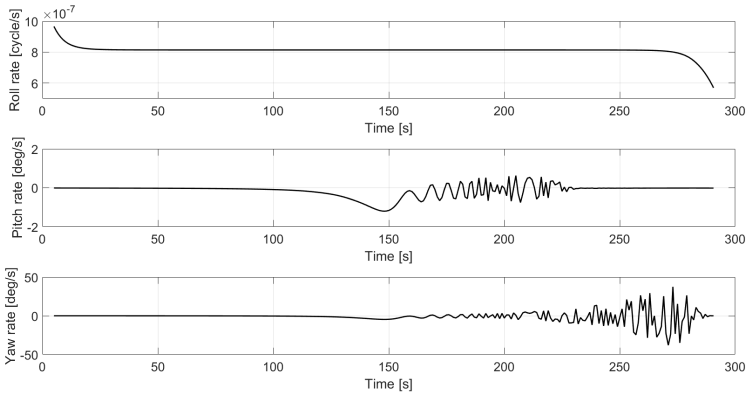

Figure 4.14: Angular rates for the T-Minus Dart launched at 85 degrees

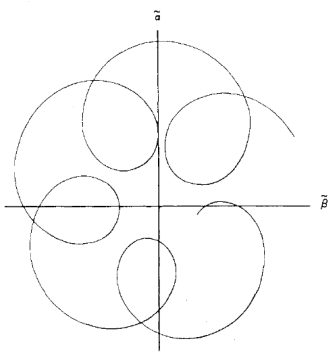

Figure 4.15: Typical epicyclic motion of a spin-stabilized shell (Murphy, 1981).

4.5.2. Stability study using the complex angle of attack

Another method to determine whether the rocket has static and dynamic stability is to determine the gyroscopic and dynamic stability factor. The methods for determining the static and dynamic stability are determined using (Murphy, 1981) and (Cornelisse et al., 1979). First, the static stability is determined by introducing the complex angle of attack and looking at the damping coefficients. Next, the dynamic stability is determined by identifying the region of dynamic stability using the gyroscopic and dynamic stability factors.

Static stability and non-spinning symmetric rockets

The static moment is assumed to be linear in the angle of attack and sideslip (Murphy, 1963):

$$C_m = C_{m_\alpha}\alpha + C_{m_0} \tag{4.22}$$

$$C_n = C_{n_\beta}\beta + C_{n_0} \tag{4.23}$$

Or combined in complex variable form:

$$C_m + iC_n = -iC_{m_\alpha}(\xi - \xi_a) + i\hat{C}_{m_\alpha}\tilde{\xi} \tag{4.24}$$

where $\xi = \beta + i\alpha$. Next to the static moment coefficients, the linear motion of a non-spinning rocket is affected by four damping coefficients: $C_{m_q}, C_{n_r}, C_{m_{\dot{\alpha}}}$, and $C_{n_{\dot{\beta}}}$. These are the yaw and pitch moment derivative, these coefficients influence that motion of the rocket around its axis in the absence of a spin rate. For an oscillatory motion, the angular derivatives are related:

$$q \doteq \dot{\alpha} \tag{4.25a}$$

$$r \doteq \dot{\beta} \tag{4.25b}$$

Due to symmetry, the complete linear transverse moment equals:

$$C_m + iC_n = -i\left(C_{M_\alpha}\xi + d_0\dot{\xi}\right) \tag{4.26}$$

where $d_0 = (l/V)\left(C_{m_q} + C_{m_{\dot{\alpha}}}\right)$. The angular motion of a spinning symmetric rocket with a linear aerodynamic moment is a two-mode epicyclic motion shown in Figure 4.15. This motion is the combination of two circular motions. For instance, a rocket that uses spin to stabilise around the body axis while it is spinning around the velocity axis. If the motion damps out the rocket is static and dynamic stable. If the motion remains constant, the rocket is static unstable and dynamic stable. If the amplitude of the motion increase the rocket is static and dynamic unstable.

Dynamic stability

Defining the coordinate system

To avoid the complexity of a spinning rocket-fixed XYZ axis system,non-spinning aero-ballistic coordinates $\tilde{X}\tilde{Y}\tilde{Z}$ are introduced. The $\tilde{X}$ axis pitches and yaws with the missile. The $\tilde{Y}$ axis is selected to lie in the horizontal plane initially, but does not remain there. If the $\tilde{Y}$ axis remain in the horizontal plane, the spin of the

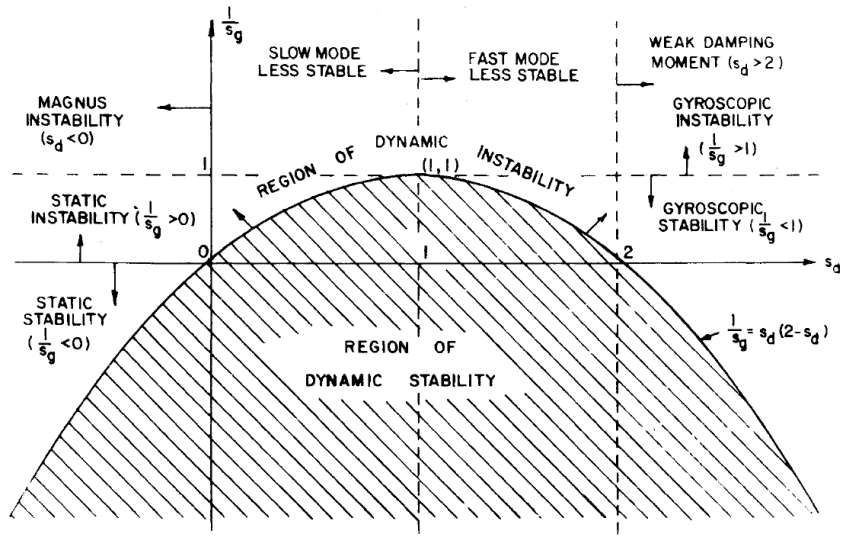

Figure 4.16: Stability regions in the $s_d - 1/s_g$ plane (Murphy, 1981).

system would be non-zero and these axes would be plane-fixed axes.

Stability factors

In aero-ballistic coordinates, the complex angle of attack and the transverse aerodynamic moment coefficients become:

$$C_{\tilde{m}} + iC_{\tilde{n}} = \left(p\hat{c} - iC_{M_\alpha}\right)\hat{\xi} - id_0\dot{\hat{\xi}} \tag{4.27}$$

with $\hat{c} = M_{p\alpha}\left(1/2\rho SlV^2 p\delta\right)$. In Equation (4.27), the first term on the right side represents the Magnus moment. A positive Magnus moment coefficient represents a moment that acts to rotate the nose of the missile around the velocity vector in the direction of the spin. Dynamic stability requires two negative damping rates and can be expressed in terms of two stability factors:

$$s_g = \frac{(\sigma p)^2}{C^*_{M_\alpha}} \tag{4.28}$$

$$s_d = \frac{-2\hat{c}}{d_0\sigma} \tag{4.29}$$

with σ is the ratio of the products of inertia. For dynamic stability, the following holds:

$$\frac{1}{s_g} = \frac{C^*_{M_\alpha}}{(\sigma p)^2} < (2 - s_d)\, s_d \tag{4.30}$$

The implications of Equation (4.30) are shown in Figure 4.16. This figure shows the stability criterion for a given point during the flight of the rocket. It shows whether a rocket posses dynamic and dynamic stability and the periodic motion associated with it.

Looking at Figures 4.17 and 4.18, where the angular motion of the rocket is presented during the boosted phase.The difference between the magnitude of the angle of attack and sideslip is explained by the aerodynamic forces acting on the rocket. The launch at 85 degrees is mainly subjected to the forces along its X_nb-axis, whereas the launch at 35 degrees is subjected to the aerodynamic forces in X_b- and Z_b-direction resulting in larger displacements in those planes. It is clear that both launches have stability, the angular motion of the rocket converges to zero. Looking at Figure 4.16, the convergence it achieved in a fast mode due to the high spin rate during the initial phase of the flight It can be seen that the rocket is in the region of dynamic stability above the S_d-axis. The motion during the coasting phase, is already discussed in the previous study and proven to be stable. .

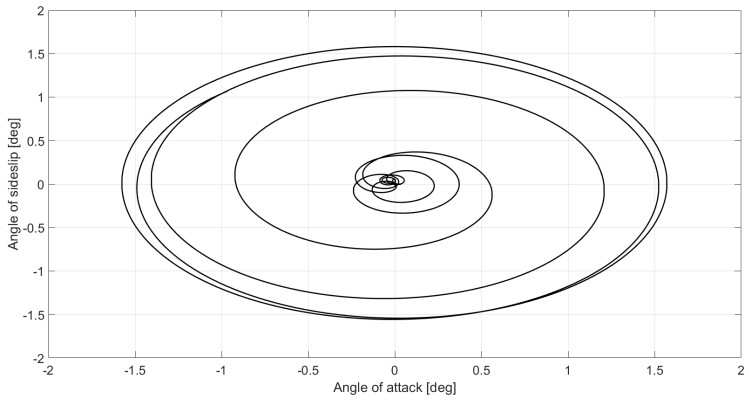

Figure 4.17: Angular stability booster launched at 30 degrees elevation.

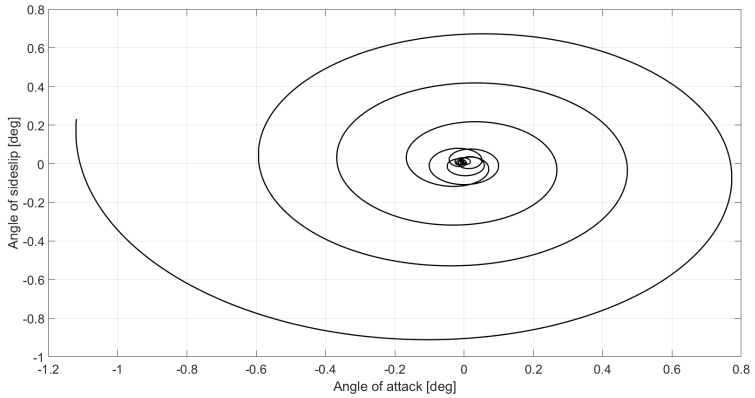

Figure 4.18: Angular stability booster launched at 85 degrees elevation.

5

Aerothermodynamic Analysis

In this chapter, the aerothermodynamic analysis of the rocket is presented. The analysis focusses on the stagnation point of the rocket, where the thermal loading at maximum is. In Section 5.1, the heat balance for the system is given. The method for determining the wall temperature in the stagnation point is given in Section 5.2. The verification of the mathematical models used is stated in Section 5.3. The chapter is finalised with a sensitivity analysis of the cooling subsystem in Section 5.4.

5.1. Heat balance

To accurately determine the wall temperature of the system, first the thermal loading acting on the system need to be identified. The focus on this research is the wall temperature in the stagnation point, where the thermal loading is the highest. The stagnation point is the point in the flow field where the local velocity of the fluid is zero. The location of the stagnation point is shown in Figure 5.1.

5.1.1. Overview

The general heat balance for a body equals (Abraham, 1962):

$$q = q_1 + q_2 + q_3 + q_4 + q_5 + q_6 - q_7 - q_8 \tag{5.1}$$

where q is the heat to the structure, q_1 the convective or boundary layer heating, q_2 th shock wave radiation, q_3 the dissociation heating, q_4 the surface combination, q_5 the solar irradiation, q_6 the Earth and sky irradiation, q_7 the back radiation from the body's surface and q_8 the internal cooling. Solving Equation (5.1) would be a time consuming and unnecessary complex computation. Therefore, the following assumptions are made:

1. The solar irradiation and the Earth and sky irradiation is neglected. The magnitude of these irradiations is small compared to the boundary layer heating and can be assumed to be zero.
2. It is assumed that the body does not experience burning of change, so that the surface combination is zero.
3. The body is assumed to be non-catalytic, there is no recombination of the dissociated oxygen or nitrogen atoms in the boundary layer.Equilibrium conditions are assumed.
4. The shock wave radiation is neglected for simplicity. Although, the magnitude of the shock wave radiation is about 10 % of the convective heating, this radiation is neglected. This error is accepted during the estimation of the wall temperature of the system.
5. The skin is thin, this means that the rate of change of the temperature is a function of the rate of total heat input to the skin and its ability to absorb this heat.

With these assumption Equation (5.1), now becomes:

$$q = q_1 - q_7 - q_8 = q_w - q_r - q_i \tag{5.2}$$

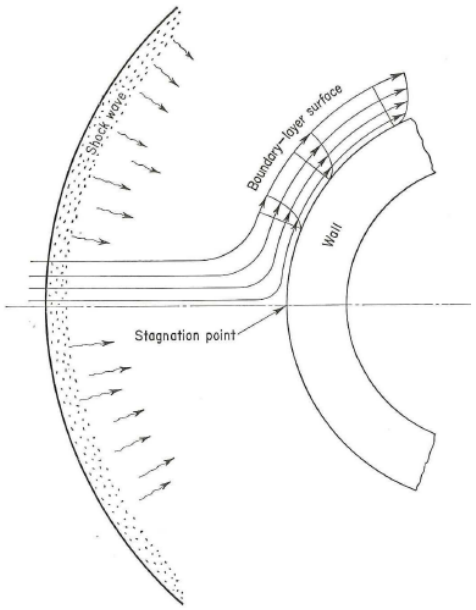

Figure 5.1: Stagnation point location (Abraham, 1962).

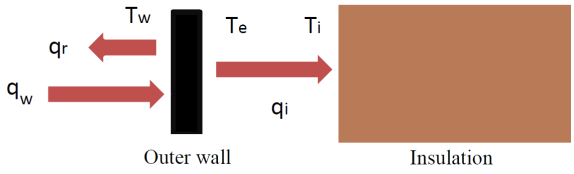

Figure 5.2: Heat balance[1].

where q_w is the convective or boundary layer heating, q_r is the radiative heating and q_i is the internal cooling. The system is represented in Figure 5.2, where the nomenclature for the temperature is also shown. In the next section, the components of the heat balance will be derived. The enhanced radiation system is shown in Figure 5.3, the system is modelled for a spherical nose.

5.1.2. Convective heat flux

General expression

The stagnation point convective heat flux for a frozen boundary layer with a non-catalytic wall equals (Cohen, 1961):

$$q_w = 0.767(\mathrm{Pr}_w)^{-0.6}\,(H_{st} - H_w)\,(\rho\mu)_{e,st}^{0.43}\,(\rho\mu)_{w,st}^{0.07}\left(\sqrt{\frac{du}{dS}}\right)_{e,st} \tag{5.3}$$

From the equation is can be seen that the stagnation point heat flux is dependent on the velocity of the flow and the atmospheric properties in the stagnation point.To accurately model Equation (5.3), expressions for the velocity gradient and the enthalpy difference are needed. The expressions are derived below followed by the boundary conditions for the system.

Components of the stagnation point heat flux

The components of the stagnation point heat flux can be calculated using the following relations and definitions as shown in Figure 5.4. The system is modelled as a two-dimensional cylindrical body with an infinite span perpendicular to the page. The radius of curvature is defined as the radius of outer skin. The direction of the flow is defined tangential along the body.

[1] Private communication, K. J. Sudmeijer

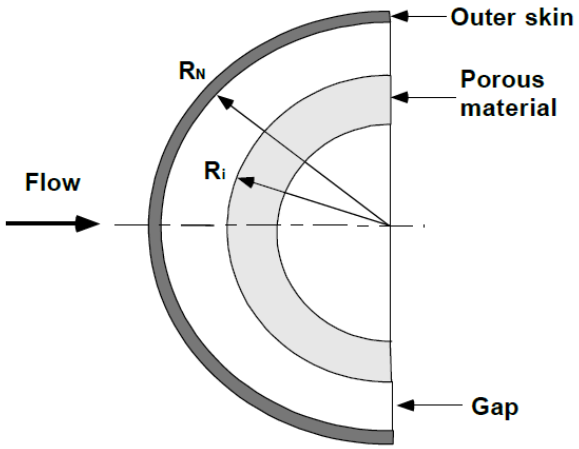

Figure 5.3: Configuration of the enhanced radiation cooling system.

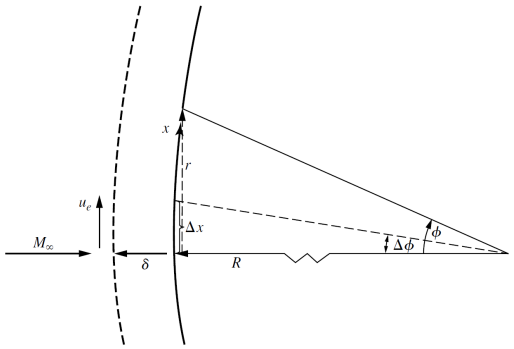

Figure 5.4: Stagnation region geometry. (Anderson, 2000)

The velocity gradient:

From Euler's equation applied at the edge of the boundary layer,

$$dp_e = -\rho_e u_e du_e \tag{5.4}$$

one obtains:

$$\frac{du_e}{dS} = -\frac{1}{\rho_e u_e}\frac{dp_e}{dS} \tag{5.5}$$

Assuming a Newtonian pressure distribution over the surface and defining the angle ϕ as the angle between the normal to the surface and the freestream, one obtains for the heat capacity at constant pressure (Anderson, 2000):

$$c_p = 2\cos^2\phi \tag{5.6}$$

From the definition of c_p, Equation (5.6) becomes:

$$\frac{p_e - p_\infty}{\bar{q}_\infty} = 2\cos^2\phi \tag{5.7a}$$

$$p_e = 2\bar{q}_e\cos^2\phi + p_\infty \tag{5.7b}$$

Inserting this relation into Equation (5.5) gives:

$$\frac{du_e}{dS} = \frac{4\bar{q}_\infty}{\rho_e u_e}\cos\phi\sin\phi\frac{d\phi}{dS} \tag{5.8}$$

This equation hold for all the points along the body. Now consider the stagnation point, in this region let ΔS be a small increment of surface distance above the stagnation point, corresponding to the small change $\Delta\phi$. Then

$$u_e = \left(\frac{du_e}{dS}\right)\Delta S \tag{5.9}$$

In the stagnation region ϕ is small. Hence,

$$\cos\phi \approx 1 \tag{5.10}$$

$$\sin\phi \approx 0 \approx \Delta\phi \approx \frac{\Delta S}{R_N} \tag{5.11}$$

$$\frac{d\phi}{dS} = \frac{1}{R_N} \tag{5.12}$$

In the stagnation point, ϕ equals zero and combining with Equation (5.9) trough (5.12), Equation 5.8 becomes:

$$\frac{du_e}{dS} = \frac{1}{R_N}\sqrt{\frac{2\left(p_e - p_\infty\right)}{\rho_e}} \tag{5.13}$$

Enthalpy difference:
The definition for the specific heat at constant pressure equals:

$$c_p = \frac{\gamma R}{\gamma - 1} \tag{5.14}$$

The gas constant equals:

$$R = \frac{p}{\rho T} \tag{5.15}$$

and for a perfect gas the following definition for the enthalpy holds:

$$H = c_p T \tag{5.16}$$

Combining the relations above, gives an relation between the enthalpy and the temperature:

$$H_s - H_w = c_p\left(T_{st} - T_w\right) \tag{5.17}$$

The atmospheric properties are determined using the relations above and the values for dry air [2].

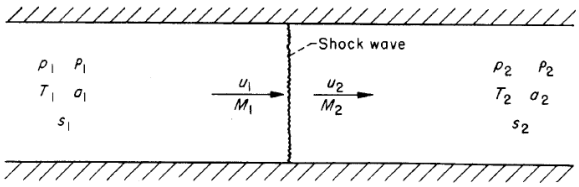

Figure 5.5: Notation for normal shock wave (Ames Research Staff, 1953).

Boundary conditions

Boundary conditions at the edge of the stagnation point boundary layer:

The conditions just downstream of the normal shock wave are determined using the equations stated in (Ames Research Staff, 1953). The notations for the normal shock wave are displayed in Figure 5.5 and the conditions for a steady normal shock require conservation of mass, momentum and energy as shown below:

$$\begin{aligned} \text{mass: } & \rho_1 u_1 = \rho_2 u_2 \\ \text{momentum: } & p_1 + \rho_1 u_1^2 = p_2 + \rho_2 u_2^2 \\ \text{energy: } & \frac{1}{2}u_1^2 + h_1 = \frac{1}{2}u_2^2 + h_2 \end{aligned} \tag{5.18}$$

The conditions for upstream of the normal shock are obtained from (National Oceanic and Atmospheric Administration, 1976). The Mach number upstream of the shock is obtained by dividing the velocity of the rocket by the speed of sound at the corresponding altitude. The following relations hold for normal shock waves in terms of the upstream Mach number:

$$\frac{p_2}{p_1} = \frac{2\gamma M_1^2 - (\gamma - 1)}{\gamma + 1} \tag{5.19}$$

$$\frac{\rho_2}{\rho_1} = \frac{(\gamma + 1) M_1^2}{(\gamma - 1) M_1^2 + 2} \tag{5.20}$$

$$\frac{T_2}{T_1} = \frac{\left(2\gamma M_1^2 - (\gamma - 1)\right)\left((\gamma - 1) M_1^2 + 2\right)}{(\gamma + 1)^2 M_1^2} \tag{5.21}$$

$$\mu_2 = \mu_1 \left(\frac{T_2}{T_1}\right)^{\frac{3}{2}} \left(\frac{T_1 + 110.4}{T_2 + 110.4}\right) \tag{5.22}$$

With the relations stated above one can estimate the boundary condition at the edge of the shock wave in the stagnation point by using $(\rho\mu)_{e,st} = \rho_2\mu_2$.

Boundary conditions in the stagnation point:

The conditions in the stagnation point are determined by using the equations stated in (Quinn and Gong, 2000). The following relations hold for the stagnation point in terms of the conditions downstream of the normal shock wave:

$$\frac{p_{st}}{p_2} = \left(1 + \frac{\gamma - 1}{2} M_1^2\right)^{\frac{\gamma}{\gamma - 1}} \tag{5.23}$$

$$\frac{\rho_{st}}{\rho_2} = \left(1 + \frac{\gamma - 1}{2} M_1^2\right)^{\frac{1}{\gamma - 1}} \tag{5.24}$$

$$\frac{T_{st}}{T_2} = \left(1 + \frac{\gamma - 1}{2} M_1^2\right) \tag{5.25}$$

$$\mu_{st} = \mu_1 \left(\frac{T_{st}}{T_1}\right)^{\frac{3}{2}} \left(\frac{T_1 + 110.4}{T_{st} + 110.4}\right) \tag{5.26}$$

With the relations stated above, one can estimate the boundary condition in the stagnation point by using $(\rho\mu)_{w,st} = \rho_{st}\mu_{st}$.

[2] http://www.engineeringtoolbox.com/dry-air-properties-d_973.html

Summary
Equation (5.3) now becomes:

$$q_w = 0.767(\mathrm{Pr})^{-0.6}\left(\rho_2\mu_2\right)^{0.43}\left(\rho_{st}\mu_{st}\right)^{0.07}\left(\sqrt{\frac{1}{R_N}\sqrt{\frac{2\left(p_e-p_\infty\right)}{\rho_e}}}\right)c_p\left(T_{st}-T_w\right) \tag{5.27}$$

With this relation, one can estimate the stagnation point heat flux as a function of the velocity gradient and the atmospheric properties.

5.1.3. Radiation heat flux
The radiation heat flux can be calculated using the Stefan-Boltzmann law (Chapman, 1984):

$$q_r = \varepsilon_e \sigma T_w^4 \tag{5.28}$$

5.1.4. Radiation between insulation and skin: cooling radiation
The cooling radiation heat flux can be determined as the radiation exchange between two enclosed concentric spheres (Bergman and Incropera, 2011):

$$q_i = \frac{\sigma\left(T_e^4 - T_i^4\right)}{\frac{1}{\varepsilon_i} + \frac{1-\varepsilon_e}{\varepsilon_e}\left(\frac{R_i}{R_N}\right)^2} \tag{5.29}$$

5.2. Process simulation
With the heat balance determined, the wall temperature can be estimated. The method used is based on (Abraham, 1962). The wall temperature is determined using the thin-skin assumption: the skin material is sufficiently conductive and thin that the temperature between the inner and outer surface is negligible: $T_w = T_e$. The rate of change of temperature over a thin skin is a function of the rate of total heat input to the skin, its ability to absorb the heat and material response. The shock wave radiation and catalytic wall effects are ignored and in the stagnation point equilibrium conditions are assumed (no dissociation). The differential equation equals:

$$\frac{T_w}{dt} = \frac{q}{\rho C_p \delta} \tag{5.30}$$

Inserting Equation (5.3), (5.29) and (5.28) into Equation (5.30) gives:

$$\rho C_p \delta\left(\frac{T_w}{dt}\right) = 0.767(\mathrm{Pr}_w)^{-0.6}\left(H_{st}-H_w\right)\left(\rho\mu\right)_{e,st}^{0.43}\left(\rho\mu\right)_{w,st}^{0.07}\left(\sqrt{\frac{du}{dS}}\right)_{e,st} - \varepsilon_e\sigma T_w^4 - \frac{\sigma\left(T_e^4-T_i^4\right)}{\frac{1}{\varepsilon_i}+\frac{1-\varepsilon_e}{\varepsilon_e}\left(\frac{R_i}{R_N}\right)^2} \tag{5.31}$$

For small time increments, the following holds:

$$\frac{T_w}{dt} = \frac{T_{w_1} - T_{w_2}}{\Delta t} \tag{5.32}$$

Inserting Equations (5.32) into (5.31), the heat balance then becomes:

$$T_{w_2} = T_{w_1} + \frac{\Delta t}{\rho C_p \delta}\left(0.767(\mathrm{Pr}_w)^{-0.6}\left(H_{st}-H_w\right)\left(\rho\mu\right)_{e,st}^{0.43}\left(\rho\mu\right)_{w,st}^{0.07}\left(\sqrt{\frac{du}{dS}}\right)_{e,st}\right) - \frac{\Delta t}{\rho C_p \delta}\left(\varepsilon_e\sigma T_w^4 + \frac{\sigma\left(T_e^4-T_i^4\right)}{\frac{1}{\varepsilon_i}+\frac{1-\varepsilon_e}{\varepsilon_e}\left(\frac{R_i}{R_N}\right)^2}\right) \tag{5.33}$$

5.3. Verification of the mathematical models
In this section, the mathematical models for estimation of the heat fluxes are tested for accuracy and the estimation of the wall temperature is verified using the data stated in (Buursink, 2005).

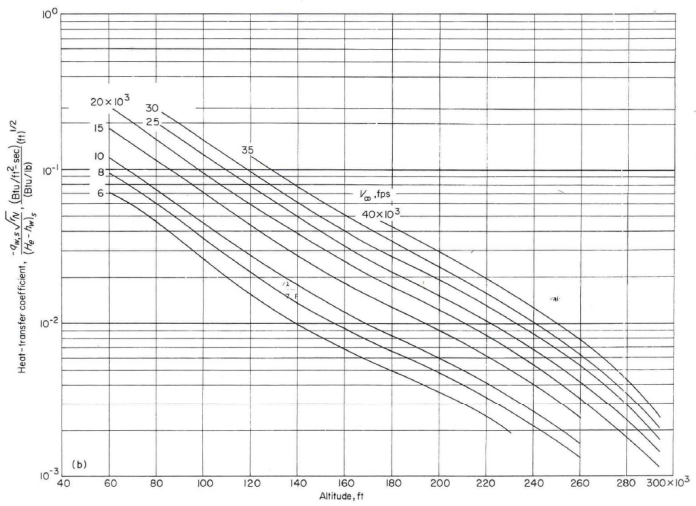

Figure 5.6: Heat transfer coefficient (Cohen, 1961).

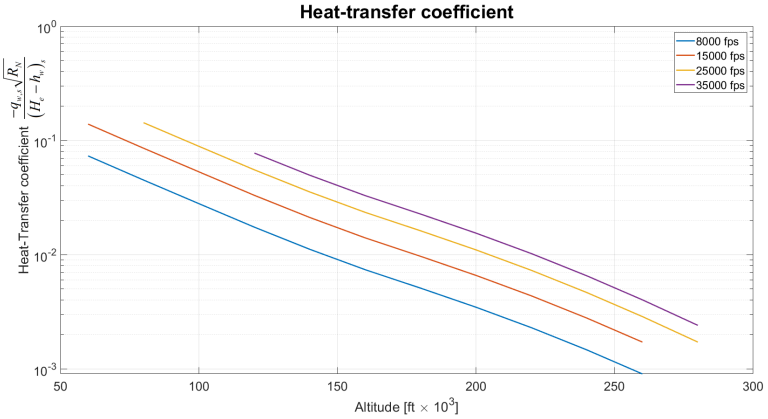

Figure 5.7: Heat transfer coefficient, Equation (5.3).

5.3.1. Heat fluxes

The equations for the body-back radiation and cooling radiation as stated in Equation (5.28) and (5.29), are commonly used relations and are assumed to be accurate for the estimation of the heat flux. The expression for the determination of the convective heat flux is tested using the heat transfer coefficient. This coefficient equals:

$$\text{Heat transfer coefficient} = \frac{-q_w\sqrt{R_N}}{(H_{st} - H_w)} \tag{5.34}$$

Equation (5.34), gives a tool to determine the accuracy of Equation (5.3), by eliminating the body configuration. The heat transfer coefficient is shown in Figure 5.6, it gives the heat transfer coefficient as a function fo the altitude. The output of Equation (5.3) is shown in Figure 5.7. It can be seen that Equation (5.3) produces the same output as the heat transfer coefficient from (Cohen, 1961). There is a small difference between the values, this is due to the accuracy used in the transformation from metric to imperial units.

5.3.2. Verification of the estimation of the wall temperature

To verify the accuracy of the estimation of the wall temperature, the data from (Buursink, 2005) is used. The test set-up is stated in Section 2.2.2, the system is subjected to a constant temperature of 1350 K. This means that using Equation (5.28), the heat flux acting on the system equals:

$$q = \varepsilon_e \sigma T_w^4 = 0.85 \cdot .670367 \cdot 10^{-8} \cdot 1350^4 = 189.2\text{KW/m}^2$$

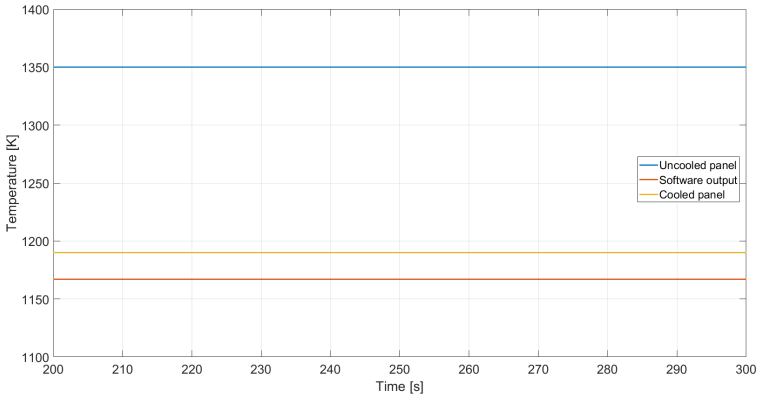

Figure 5.8: Wall temperature verification

To verify that the software produces accurate results, one first need to modify Equation (5.33) to fit the exchange between two plates instead of two sphere. Equation (5.33) becomes now:

$$T_{w_2} = T_{w_1} + \frac{\Delta t}{\rho C_p \delta}\left(18.92 \cdot 10^3\right) - \frac{\Delta t}{\rho C_p \delta}\left(\varepsilon_e \sigma T_w^4 + \frac{\sigma\left(T_e^4 - T_i^4\right)}{\frac{1}{\varepsilon_i} + \frac{1}{\varepsilon_e} - 1}\right)$$

Where the cooling radiation between two plates equals:

$$q_i = \frac{\sigma\left(T_e^4 - T_i^4\right)}{\frac{1}{\varepsilon_i} + \frac{1}{\varepsilon_e} - 1}$$

The output of the software is stated in Figure 5.8, with the focus on the time interval 200 - 300 seconds. This interval is chosen to be the focus since here the results can be compared, in this interval the cooling system works at full capacity. As can be seen from Figure 5.8, the software produces an error of 23 degrees. This error was already identified by (Buursink, 2005), the difference between the experiment values and the software output varies between 35 and 57 degrees. This is due to the assumptions made in the software, the evaporation rate of water and the influences during the experiment. Taking this error into account, one can state that the software produces an accuracy sufficient for the first estimation of the wall temperature of the cooling system.

5.4. Sensitivity analysis

5.4.1. Overview

The system is shown in Figure 5.3. Previous research determined that the use of water as coolant is the most suited for this system. The high heat of evaporation of water makes it the ideal for this purpose (Sudmeijer, 2005). The gap between the outer shell and the insulation is set at 3 mm. This is determined by (Buursink, 2005) as the optimal width for the vapour flow. The following materials are defined: type 304 stainless steel as the outer skin, ZAL15 as the insulation material, water as the coolant and high emissivity coating on the inside of the outer shell to maximise the cooling radiation. The physical properties for the materials are shown in Table 5.1. The initial conditions are:

$$T_i = 373\text{K}$$
$$T_{w_0} = 300\text{K}$$

5.4.2. Dry thermal protection system

To calculate the wall temperature for the 'dry' experiment, one needs to adjust Equation (5.33). The 'dry' experiment has no interaction between the insulation and the outer skin, this means that $q_i = 0$. Equation

[3] Obtained from http://www.zircarceramics.com/pages/rigidmaterials/specs/zal15.htm

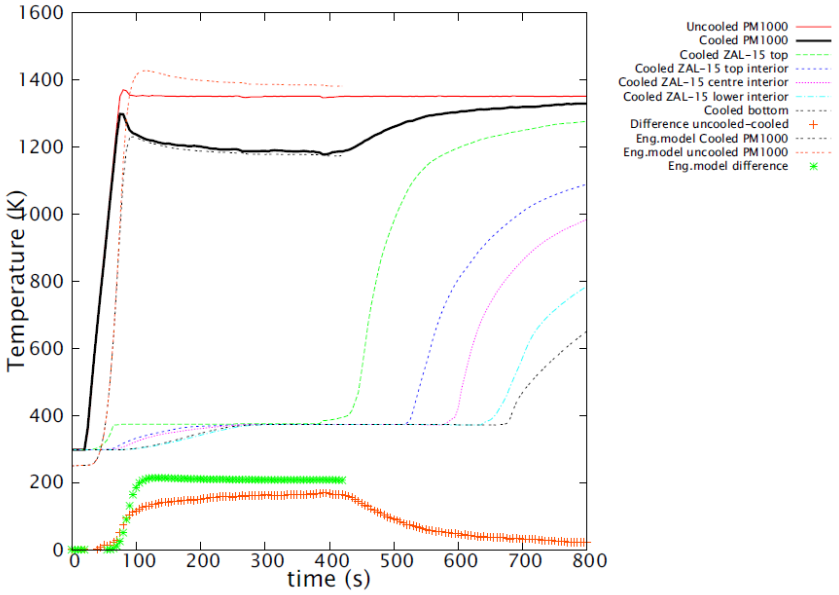

Figure 5.9: Temperature measurements of the test set-up (Buursink, 2005).

Table 5.1: Physical properties of the skin and insulation

Parameter	Type 304 Stainless Steel (Stainless Structurals, 2017)	ZAL15[3]	High emissivity coating
k [$W \cdot m^{-1} \cdot K^{-1}$]	21.4	0.16	n/a
C_p [$J \cdot kg^{-1 \cdot K^{-1}}$]	500	1047	n/a
ρ[$kg \cdot m^{-3}$]	6750	240	n/a
ε	0.6	0.91	0.9

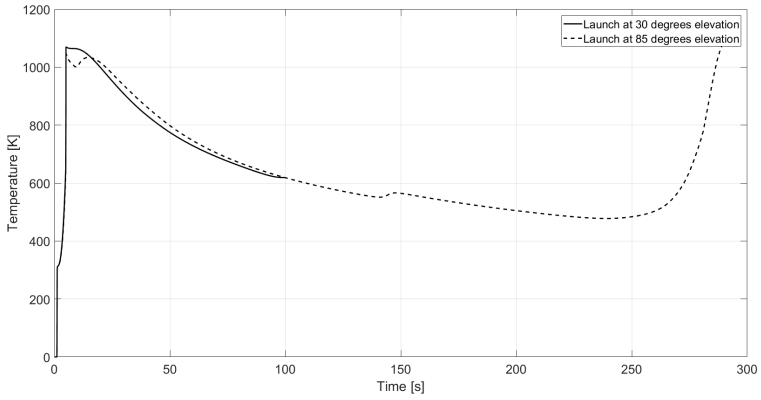

Figure 5.10: Uncooled wall temperatures for the T-Minus Dart for different launch angles.

(5.33) now becomes:

$$T_{w_2} = T_{w_1} + \frac{\Delta t}{\rho C_p \delta}\left(0.767(\mathrm{Pr}_w)^{-0.6}\left(H_{st} - H_w\right)\left(\rho\mu\right)_{e,st}^{0.43}\left(\rho\mu\right)_{w,st}^{0.07}\left(\sqrt{\frac{du}{dS}}\right)_{e,st} - \varepsilon\sigma T_w^4\right) \tag{5.35}$$

The result for both launch angles is shown in Figure 5.10. A configuration of an outer shell of 35 diameter with a thickness of 0.5mm, a gap of 3 mm and an insulation sphere of 14 mm radius is assumed during this estimation. It can be seen that all both curves have the same shape: a high peak during the boosted phase and a constant phase during the coasting phase. The constant phase is our area of interest since the experiment can here be tested over a period of time under relatively constant parameters. The difference between both curves is very small, this is due to same velocity profile during the first 100 seconds of the flight. The stagnation point heat flux is highly dependent on the Mach number, resulting in similar results for both launch angles.

5.4.3. Wet thermal protection system

The wall temperature for the wet experiment can be determined using equation (5.33) (repeated below).

$$T_{w_2} = T_{w_1} + \frac{\Delta t}{\rho C_p \delta}\left(0.767(\mathrm{Pr}_w)^{-0.6}\left(H_{st} - H_w\right)\left(\rho\mu\right)_{e,st}^{0.43}\left(\rho\mu\right)_{w,st}^{0.07}\left(\sqrt{\frac{du}{dS}}\right)_{e,st}\right) - \frac{\Delta t}{\rho C_p \delta}\left(\varepsilon\sigma T_w^4 + \frac{\sigma\left(T_e^4 - T_i^4\right)}{\frac{1}{\varepsilon_i} + \frac{1-\varepsilon_e}{\varepsilon_e}\left(\frac{R_i}{R_N}\right)^2}\right) \tag{5.33}$$

Inserting these values in the software, results in a temperature drop of around 30 %. This is not a large drop in temperature. Reflecting on Equation (5.2), it can be seen that the advantage of this system is not the drop in temperature but the resistance to higher aerodynamic heat loading. Assuming the dry and wet experiment are subjected to the same aerodynamic heating, then the wet experiment will produce the same wall temperature for a heat load roughly increased with a factor:

$$\frac{1}{\frac{1}{\varepsilon_i} + \frac{1-\varepsilon_e}{\varepsilon_e}\left(\frac{R_i}{R_N}\right)^2} \tag{5.36}$$

For the T-Minus Dart equipped with the enhanced radiation cooling TPS, it will be able to withstand a heat load of roughly two times larger than a rocket without the thermal protection system, while having the same wall temperatures. Looking at Figure 5.11, it can be seen that there is a measurable region during flight.

5.4.4. Skin thickness

Looking at Equation (5.33), it can be seen that the term for the skin thickness, δ, has a major role in the determination of the cooling effect of the enhanced radiation system. The thinner the skin, the higher the

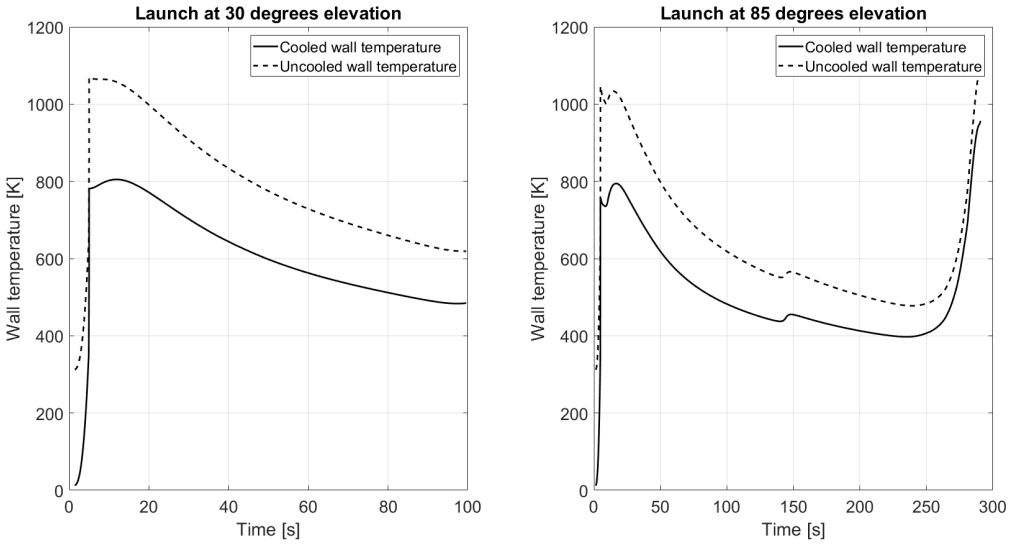

Figure 5.11: Wall temperatures for the T-Minus Dart.

wall temperature will be at the inside of the outer shell resulting in a higher cooling radiation and the larger the effect will be of the cooling. The effect of various skin thickness can be seen in Figure 5.12. The effect is shown 30 seconds after launch until touchdown, here is the effect is clearly visible. The selected mission is the launch with 30 degrees of elevation. It can be seen that the thinner the skin, the larger the effect of the cooling system will be.

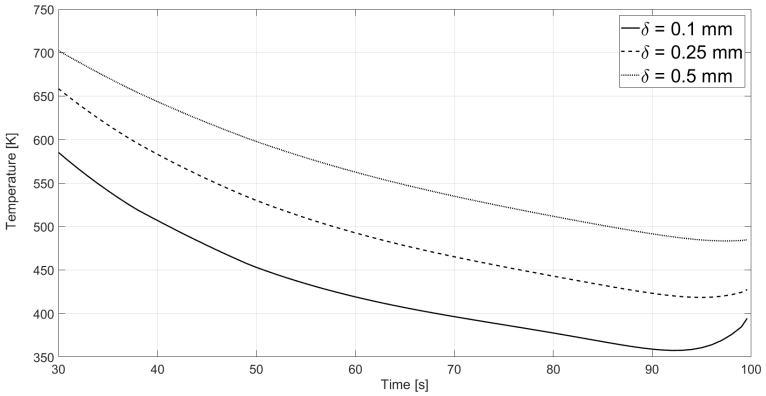

Figure 5.12: Effect of skin thickness on the enhanced radiation cooling system

5.4.5. Coolant usage

To estimate the amount of coolant (assumed to be water), one first needs to find the total heat load acting on the nose. The total heat rate is related to the stagnation point heat rate by (Anderson, 2000):

$$\frac{q_{total}}{q_w} = \cos^{\frac{3}{2}}\phi \tag{5.37}$$

In Equation (5.37), the cosine variation has a theoretical limit of up to 45 degrees and gives reasonable results up to 70 degrees (Tauber, 1989). The total heat load can calculated by integrating Equation (5.37) over the

entire body:

$$\begin{aligned} Q_{total} &= \int_0^{\phi} q_{total}(\phi)\, dA \\ &= \int_0^{\phi} q_w \cos^{\frac{3}{2}}\phi 2\pi R_N \sin\phi R d\phi \\ &= -\frac{4}{5}\pi R^2 q_w \cos^{\frac{5}{2}}\phi \Big|_0^{90} \\ &= \frac{4}{5}\pi R^2 q_w \end{aligned} \tag{5.38}$$

With $dA = 2\pi R_N \sin\phi R d\phi$. Equation (5.38) extends the limit of 70 degrees, but since $q_{total}(90) \ll q_w$, the assumption still holds. If the assumption is made that all heat is absorbed by the water, the water consumption can be determined using the definition of the heat of evaporation

$$\dot{m} = \frac{Q_{total}}{H_{vap}} \tag{5.39}$$

The total amount of water needed is then easily computed by the summation of the mass flow per instant of time. Calculating the amount of water needed for both mission gives a total amount of 3.2 grams for the mission launched at 30 degrees elevation and 3.8 grams for the mission launched at 85 degrees elevation. This overestimates the amount of water needed. In Equation (5.39), the heat of evaporation is assumed to be constant at 2257 J g^{-1}, however this is not a constant value. This value for water pressurised at 1 atmosphere. During flight, the pressure will decrease causing the heat of evaporation to drop. As stated in Section 2.2.2, to take the saturation level of water into account, one need to add 20% to this volume, resulting in approximately 4.8 grams of water needed. This value estimated here is a good first estimate of the water needed during the experiment. Section 2.2.2 also stated that the maximum convective heat flux can not be larger than 8 MW/m^2, Figure 5.14 gives the convective heat flux for the mission launched at 30 degrees elevation. The heating will be larger than the mission launched at 85 degrees due to its presence in the lower atmosphere. The maximum heat flux acting on the system reaches only a value of 0.5 MW/m^2, clearing the danger of developing a thin layer of vapour between the water and the outer shell.

A point of interest for the use of water is the triple-point (see Figure 5.13), this is the combination of pressure and temperature where all 3 phases of water occur. For water is this point at 273.16 K and 611.657 Pa Wagner et al. (1994). During this experiment, the minimum static pressure is 0.0204 Pa for the mission launched at 85 degrees elevation and 22061 Pa for the mission launched at 30 degrees elevation (see Figure 5.15). However, the temperature of the vapour is assumed to be at 373 K, this means that there is no phase change from gas to solid.

5.4.6. Results and discussions

From the sections above, the following conclusions can be drawn to obtain the optimum design. Firstly, regarding the skin thickness, the thinner the outer shell, the higher the cooling effect will be. However, the thickness is limited to what is possible to manufacture. Therefore, the skin thickness is selected on 0.5 mm, this is a realistic thickness that can be manufactured. Furthermore, the aim for the experiment is to measure the temperature and the effect of the enhanced radiation system on it. Both launch angles of 30 and 85 degrees elevation have a relative constant region where the temperature can be accurately measured. The choice of a preferred mission is made in Section 6.2, where all the aspects of the experiment are taken into account. As discussed in Section 5.4.3, one of the main aspects of the system is to increase the incoming aerodynamic heat flux while maintaining the same temperature. To check whether the statement holds that the incoming heat flux can be doubled for the same wall temperatures, the simulation is run with both heat fluxes and compared in Figure 5.16. It can be seen that when doubling the incoming heat flux, the system with the enhanced radiation cooling produces the same wall temperature as the system without the cooling system subjected to normal heat flux. The significant, measurable drop in wall temperature when applying the cooling system ensures that an experiment to verify this drop is feasible. Detailed description of the system and experiment are given in Chapter 6.

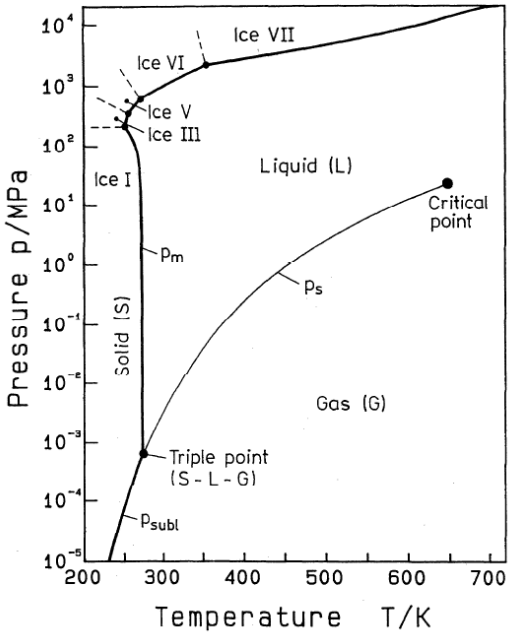

Figure 5.13: The phase-boundary curves of water (Wagner et al., 1994).

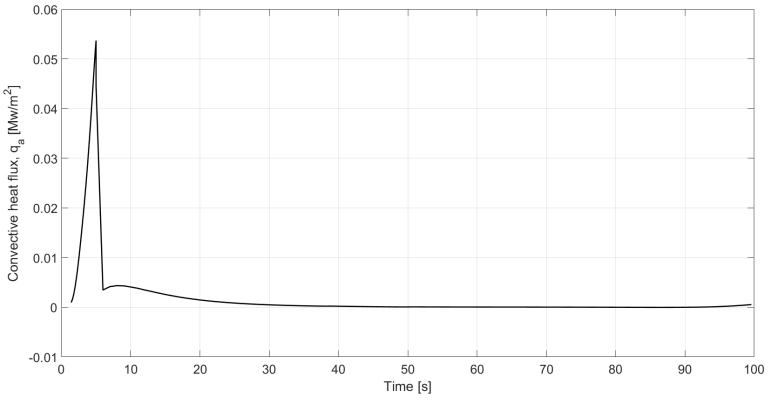

Figure 5.14: Convective heat flux during flight T-Minus Dart.

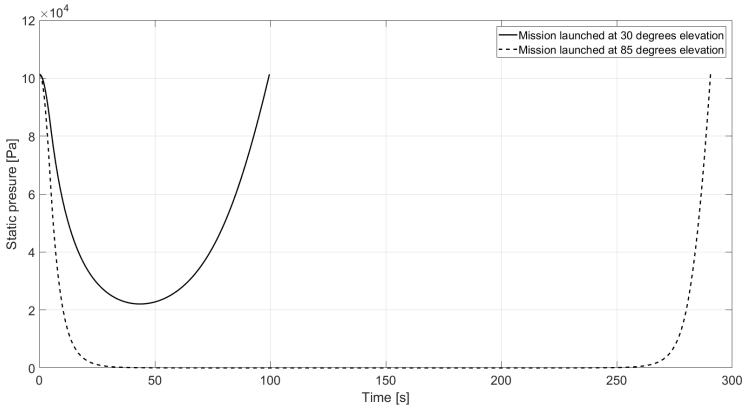

Figure 5.15: Static pressure during nominal flight

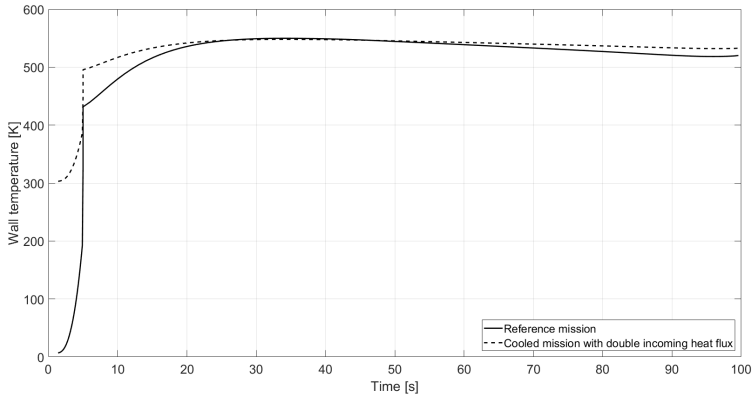

Figure 5.16: Effect of the enhanced radiation cooling system

6

Subsystem and Experiment Design

In this chapter, the subsystem and experiment design is stated. In Section 6.1, the mechanical design of the subsystem is presented. The design of the experiment is shown in Section 6.2.

6.1. Subsystem design

From the discussions and results in Section 5.4, the optimum design for the enhanced radiation experiment is achieved. The complete mechanical design (enhanced radiation cooling system and temperature measurement instrumentation) is shown in Figure 6.1. First, an overview of working of the the cooling process will be given. Next, the experiment manufacturing, assembly and mounting will be presented.

6.1.1. Process Overview

During flight, the experiment cools down the outer shell by means of enhanced radiation cooling. The optimal dimensions for the components crucial for the cooling are shown in Figure 6.2. Before launch the 14 mm radius insulation sphere is filled with approximately 4.8 grams of water. During flight, the rocket will heat up due to aerodynamic heating and the water will start to evaporate. The vapour will fill the 3 mm gap between the insulation and the outer shell, the result is that the temperature on the surface of the insulation will not raise above the boiling temperature of water. This will cool down the inner wall of the outer shell resulting in a lower wall temperature of the outer wall of the shell. The vapour will be discarded trough channels in bracket 1 to outside the rocket into the boundary layer. Directly removing the vapour from the system removes the need for a storage measure for the water. The channels for the vapour are shown in Figure 6.3, there are four channels evenly spaced in a circular pattern in bracket 1. The temperature of the wall is measure by the use of a thermocouple, mounted in the centre of the system as shown in Figure 6.1. As a reference, a fine-diameter mineral-insulated thermocouple with exposed junction[1] is used.

6.1.2. Experiment manufacturing, assembly and mounting

Manufacturing

The experiment is designed following the KISS (Keep It Simple, Stupid) principle, the system is kept as simple as possible and unnecessary complexity is avoided. The brackets can be manufactured from a rod using a lathe with the thread and the channels drilled in a later stage. The insulation sphere is cut to size and sanded down by the manufacturer. The outer shell is the most difficult component to manufacture, it is crucial that the sphere is virtually perfect and with the required thickness. The process most suitable for this, is deep drawing. A sheet is drawn through a die opening creating the sphere and then cut to the desired length. The materials used for the manufacturing are stated in Table 6.1 and the measurements for the brackets are stated in Appendix C.

Assembly and mounting

The experiment is designed in such a way that it mostly can be assembled and mounted on site. The only components that need to be assembled beforehand is the insulation sphere with the position tube for the

[1] https://www.omega.com/pptst/KMTSS_JMTSS_CHB.html

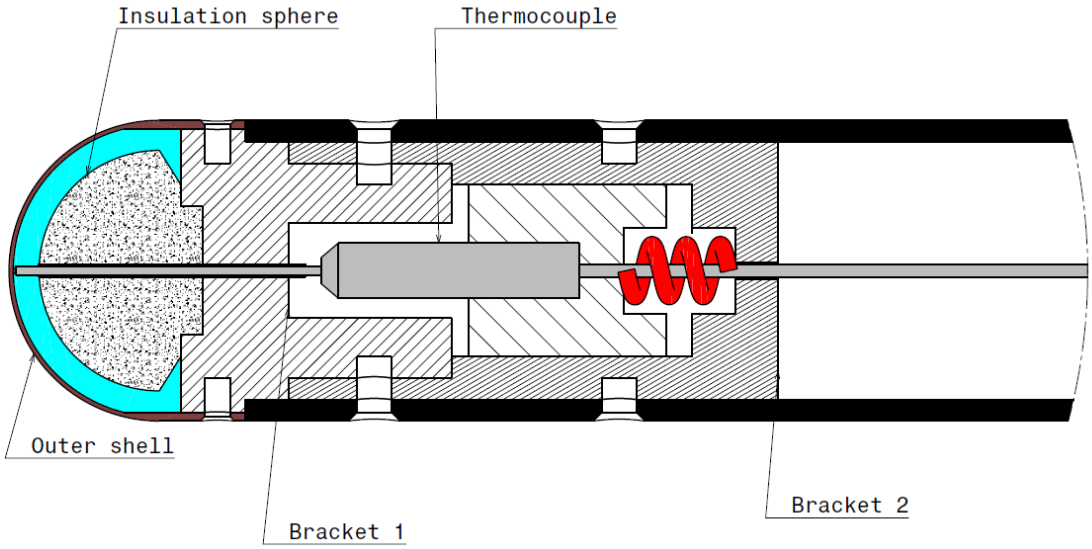

Figure 6.1: Experiment overview, all dimensions in mm.

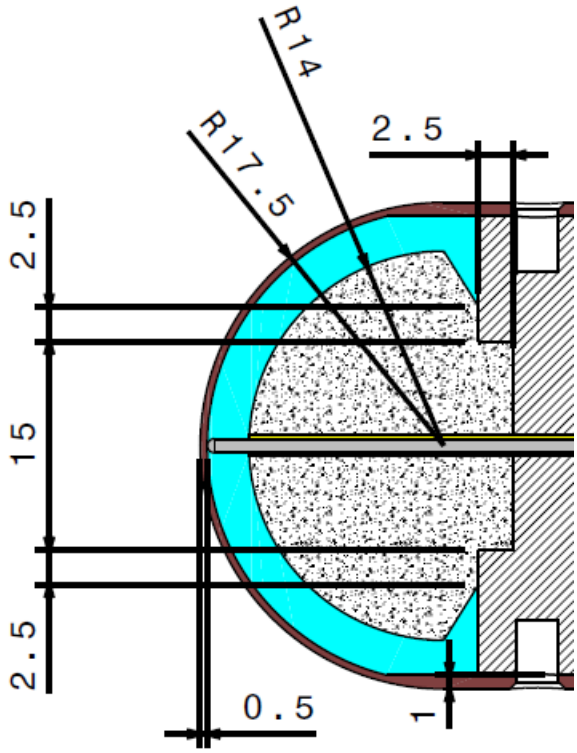

Figure 6.2: Dimensions of the cooling system, all dimensions in mm.

Table 6.1: Materials used in the enhanced radiation cooling experiment.

Part	Material
Shell	Type 304 Stainless Steel
Insulation	ZAL15
Coolant	H_2O
Coating	High emissivity coating, US 5668072 A
Brackets	Type 304 Stainless Steel

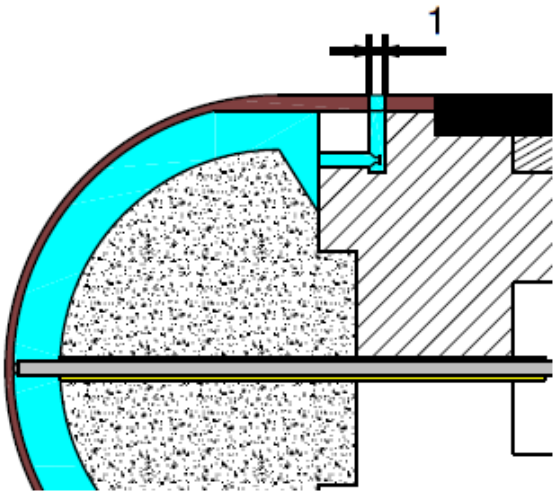

Figure 6.3: Channels for removing the vapour from the system..

thermocouple on bracket 1, this is to give to adhesive time to cure, and the coating on the inside of the outer shell, to ensure a uniform and clean coverage. The other components can be assembled and mounted on the rocket on site.

At the launch site, the first step is to install the thermocouple in the rocket. Looking at Figure 6.1, it can be seen that the thermocouple is placed inside an unsecured bracket inside bracket 2. This is done to ensure that the thermocouple can move along its centreline. The rationale behind this is that during launch, the system is subjected to an acceleration of around 36 g. This means that the possibility exists that the thermocouple is forced back. A spring is installed at the bottom of the bracket to ensure that when this happens, the thermocouple is forced forward restoring contact with the outer shell. The bracket has also the possibility to move forward to respond to the possible expanding of the outer shell. During flight, the outer shell is part subjected to the highest thermal loading. Since the part is designed as thin as possible to maximise the cooling effect, it is sensitive to thermal expansion. To cope with this during flight, the bracket with the thermocouple can be pushed forward to ensure constant contact with the outer shell. As last safety measure, to ensure continuous contact between the outer shell and the thermocouple, the insulation is fitted with position tube in its centre. This is done because the sheath of the thermocouple is flexible, positioning it inside the tube will ensure that it stays into position and will not drop back into the cavity below.

When bracket 2 is secured to the body of the Dart using 4 evenly spaced bolts, the bracket with the thermocouple and spring can be put into place. The next step is to fill the insulation with water . This can be done by submerging the insulation into water and letting it absorb it. Another option is to manually insert to water in the insulation using a for instance injection needle. Since only 4 grams of water is required, this can easily be done on site. If the insulation is filled with water, it can be placed on to of bracket 2, and secured using 4 evenly spaced bolts. To prevent bracket 1 to move back and push bracket 2 down during flight, the bolts securing bracket is to the Dart is also put trough bracket 2. The final step is to mount the outer shell on the rocket. This is done by simply bolting the shell to bracket 1, when the shell and bracket 1 are bolted together the channels for the removal of the vapour align through the shell and bracket 1. With this last step, the rocket is ready for launch.

6.2. Experiment design

In this section, the experiment design is treated. It gives insight in the data needed to make the experiment successful, the instrumentation to obtain the data and the optimum trajectory to obtain the most accurate results.

6.2.1. Flight data

As stated in Section 2.4.1, three data sets need to be obtained to make the experiment a success: a temperature profile, the angular rates and a GPS output.

- *Temperature profile:* The temperature profile is the temperature of the outer shell over time during flight. This will show the impact of the enhanced radiation cooling experiment.
- *GPS data:* The time and position of the rocket during flight. From this dataset the trajectory and the velocity of the rocket can be modelled.
- *Angular rates:* The angular rates of the rocket are needed firstly to check if the simulation produces accurate results and secondly to check the stability of the rocket.

6.2.2. Instrumentation

To obtain the datasets as stated in the previous section, the following instruments are needed:

- *Thermocouple:* To measure the temperature of the outer shell. The thermocouple is placed in the centre of the experiment with its exposed junction against the outer shell. The sheath is equipped with a sprig to withstand the accelerations in X direction such that the thermocouple has constant contact with the outer shell. In this study the thermocouple is modelled after a fine-diameter mineral-insulated thermocouple with exposed junction[2].
- *GPS receiver:* To obtain the data from the GPS satellites, a receiver and antennas are needed. The dataset carried by the GPS signal contains three types of data[3]:
  1. Pseudo-random code: an identification code that shows which satellite is transmitting the information.
  2. Ephemeris data: the almanac data on the GPS signal contains the status of the satellite as well as its date and time,which is used to determine the position of the GPS receiver.
  3. Almanac data: this dataset gives information about the position of the satellite and orbit information of the transmitting satellite.

  The GPS signal is send on the L1 frequency (1575.42 MHZ).
- *Inertial Measurement Unit (IMU):* by using triaxial accelerometer and triaxial gyroscope sensors, it generates the acceleration, angular rate, position and velocity of the rocket (Lord Mirostrain sensing, 2017).
- *Communication system:* this is needed to transmit the data during flight to the ground station. This system is crucial for obtaining the datasets generated during flight. The datasets can be sent down in two ways. Firstly, when in apogee the nose can be separated from the body and antennas will be deployed to sent the data down or secondly, the use of an antenna ring which enables the rocket to continuously transmit data from lift-off to touch down.
- *Power system:* the instruments needs to be powered during flight. Since the instruments do not require much power an ordinary battery pack will be sufficient.

6.2.3. Launch campaign

The last part of the experiment is to determine the optimum launch angle for this experiment. Looking at Section 5.4.3, it can be seen that the wall temperatures for both the launch at 30 and 85 degrees are similar in magnitude. The decision for the launch angle is made by looking at the complexity of the entire experiment and the parameters that need to be measured. Figures 6.4 and 6.5 show the areas of interest of the experiment. These areas are the velocity profile, the altitude profile and temperature. For the 30 degrees launch, the values during the boosted phase are relatively constant but for the launch at 85 degrees there is a strong variation in the velocity profile. Therefore, the launch at 30 degrees has the preference.

Another consideration is the complexity of the system. Since the experiment is designed according to the KISS principle, the launch at 30 degrees elevation will result in a simpler system. The rocket can be equipped

[2] Obtained from https://www.omega.com/pptst/KMTSS_JMTSS_CHB.html
[3] Obtained from http://www.radio-electronics.com/info/satellite/gps/signals.php

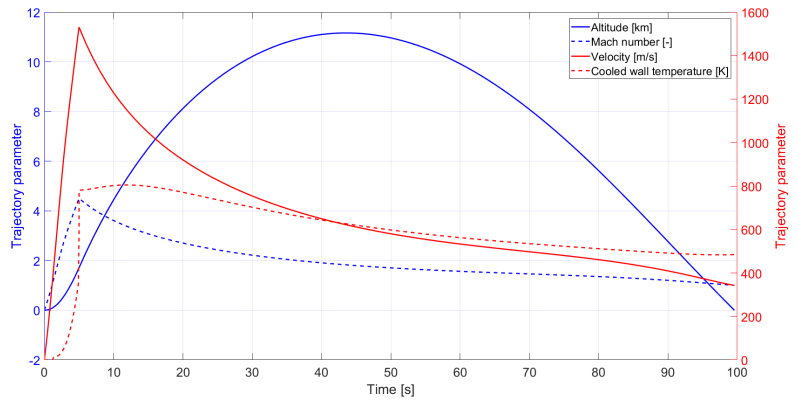

Figure 6.4: Parameter overview for the launch at 30 degrees elevation.

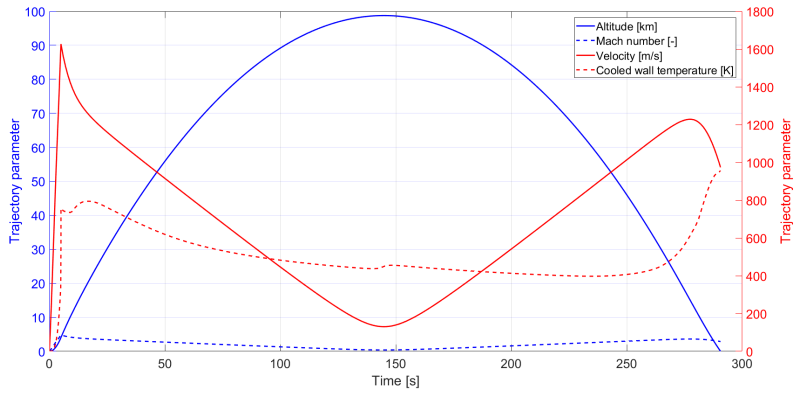

Figure 6.5: Parameter overview for the launch at 85 degrees elevation.

with an antenna ring to transmit the data to the ground station and with a Phoenix receiver (Grillenberger and Markgraf, 2011) as GPS receiver. The advantage of using a Phoenix receiver is the blade antennas which can be mounted on the outside of the rocket (for instance integrated in the fins). This will bypass the blocking effect of the body of the rocket, resulting in more accurate measurement. One could argue that with the use of an antenna ring and the Phoenix receiver, the launch at 85 degrees elevation has the same advantage. This is true but the main advantage of having a low trajectory is that the distance over which the data needs to be sent will be smaller. The need for strong power consuming transmitters in not needed and will simplify the system. The use of separation at apogee is discarded because it will greatly increase the complexity of the system (parachute deployment etc.), continuously sending data using build in antennas is the preferred choice.

7

Conclusions and Recommendations

This thesis aimed to provide the first step in answering the research question:

Can an active thermal protection system improve the flying characteristics and the flight performance of a re-entry vehicle?

The goal of this thesis was to set up an experiment to validate the impact of an active thermal protection system. The work done in the thesis can be divided in four main categories: the development of a flight simulator and a tool for the estimation of the wall temperature in the stagnation point, a sensitivity analysis of an enhanced radiation cooling thermal protection system and the design of a validation experiment. In Section 7.1, the conclusion regarding these four tasks are stated. The recommendations for improvement of the tools and for future work are presented in Section 7.2.

7.1. Conclusions

The selection of enhanced radiation cooling as the TPS, has proven to be able to improve the flying characteristics and performance of a re-entry vehicle. The enhanced radiation cooling has been designed to be mounted on the T-Minus Dart. The choice for this sounding rocket was driven by availability and cost. However, the use of this rocket needs to be further investigated since during the thesis research problem rose regarding the overly stable rocket. The vehicle is designed to follow a high altitude trajectory while the area of interest for this experiment is at low altitudes where the thermal loading is the largest. The possible trajectories have been simulated using the flight simulator. The simulator has been verified using data from other nominal missions, but the modelling of the atmosphere and more specifically the wind variations has not been researched to a degree that they were implemented and verified in the software. The tool is more than suited to estimate a trajectory of sounding rocket, but if a re-entry mission were to be simulated the assumptions in the model would not hold any-more and this would ensure a loss in accuracy.

With the obtained flight data from the flight simulator, the cooling impact of the enhanced radiation TPS was estimated. The model is developed and verified for a two-dimensional heat flow acting on the system. The assumption that only an incoming aerodynamic and the body heat fluxes interact with the vehicle, makes it not suitable for re-entry testing. However, the tool was verified using experimental data obtained from a plasmatron, there is was shown that the tool has the desired accuracy and produces results with an acceptable accuracy. The impact of the enhanced radiation cooling system has been determined and it was proven that this concept holds the promise to become an efficient, reusable and cheap TPS. The reduction of the wall temperature and the ability to be able to withstand a heat flux twice as high makes this concept very feasible to be applied on a space mission.

The impact of the cooling system together with the chosen vehicle, an experiment is set up to validate the impact of the cooling subsystem. A mechanical design of the cooling subsystem has been made. The design for the experiment is ready to undergo testing and take the next step in the validation of the enhanced radiation cooling TPS. A first insight can be given in answering the research question: *Can an active thermal protection system improve the flying characteristics and the flight performance of a re-entry vehicle?* The tools

developed in this thesis research gave a first indication that the question can be answered positive. The thesis aimed to set up an experiment to validate the impact of enhanced radiation cooling. The first step in answering this question has been taken, however many more steps need to be taken before the system can be validated as a TPS for a re-entry vehicle. A proposal for the next step and recommendations regarding the research are given in the next section.

7.2. Recommendations

7.2.1. Recommendations regarding the tools

Flight simulator

The flight simulator tool is already extensive but can be improved on a few areas. Firstly, the tool makes use of the Matlab Aerospace Toolbox for importing the aerodynamic coefficient form the Missile Datcom file, the cubic spline data interpolation and the ode45 (RKDM) functions. This requires a lot of computation time and rewritten this functions will significantly reduce the computation time of the flight simulator. Furthermore, a estimated value is used for the Magnus coefficients, when simulating a re-entry trajectory it is recommended that the equations as stated in Section 3.4 are used. If the simulator is updated to these elaborated models, the final step is to update the environment of the rocket by implementing a non-uniform gravity field and the wind profiles that act in the atmosphere.

Thermodynamic analysis

The thermodynamic analysis tool is developed for a 2 dimensional heat balance in the stagnation point. This gives a good first estimate of the maximum temperatures experienced bu the outer shell. However, the tool needs to be extended for the entire subsystem, not only in the stagnation point. This means that the next step is to model the vapour flow inside the subsystem and the temperature distribution over the entire wall. The incoming aerodynamic heat flux varies with the body angle of the nose of the rocket resulting in a non uniform heating of the wall. The evaporation of the water can as a result be also non uniform, giving a non uniform cooling of the outer wall. This needs to be investigated carefully to get an accurate representation of the cooling mechanisms.

7.2.2. Recommendations regarding the subsystem design

During this research the focus of the design lay on the enhanced radiation cooling system implantation on the T-Minus Dart rocket. An experiment is derived using the tools to test the effect fo the cooling system on the wall temperature. However, to perform a real-life rocket test, there needs to be research and designing done on the instrumentation and the mechanical loading. The required instrumentation is selected but the detailed architectures and budgets needs to be researched. The design challenge lies in the constraints of the rocket and the selected trajectory. The most important architectures needed for this research that need to be determined are the communications and attitude determination architecture.

With all the architectures and the subsystem design, the experiment needs to undergo an verification campaign. Special interests are the mechanical loading and the data management. The experiments needs to survive and operate during a highly accelerated flight, this means coping with the accelerations and forces acting on it, the resistance to vibrations due to the launch and propelled phase, and the high velocity impact during flight. These three parameters are the main challenges in terms of mechanical loading in finalising the design of the experiment. The data management need to be verified on beforehand, this is due to the fact that the rocket will not be recovered after flight. All the datasets need to be sent before touchdown of the rocket.

Another area of interest in the experiment design, is to perforate the outer shell such that the vapour travels along the outside of the nose. This should decrease the temperature of the wall further but rises questions about boundary layer contamination. When performing a re-entry flight, one needs to investigate the effect of releasing water vapour in the boundary layer and its possible consequences. This system can cool down the rocket further than enhanced radiation cooling but needs to be investigated thoroughly.

7.2.3. Recommendations regarding the T-Minus Dart rocket

During the research it is assumed that the separation between the booster and the rocket is executed perfectly and has little to no impact on the flight profile. The effect of the separation needs to be investigated and

implemented in the design of the experiment. The lock and release mechanism between the booster and the rocket is the main area of interest.

7.2.4. Future work

This thesis research forms an elaborated basis to further develop the enhanced radiation cooling TPS. The next step is to accurately model the heat loading acting on the system and the behaviour of the coolant inside the system. With this knowledge, an accurate model is obtained and can be verified using a test in the plasmatron. With this verification test, the experiment can be made flight ready and undergo an verification campaign in accordance with the ECSS standard (European Cooperation for Space Standardization, 1998). The final step in the research is to validate the impact of the enhanced radiation TPS with a flight test.

Bibliography

Abney, E. J. and McDaniel, M. A. (2005). High angle of attack aerodynamic predictions using missile datcom. *AIAA paper*, 5086:2005.

Abraham, L. H. (1962). *Structural design of missiles and spacecraft*. McGraw-Hill.

Ames Research Staff (1953). Equations, tables, and charts for compressible flow. Technical report, National Advisory Committee for Aeronautics.

Anderson, J. D. (2000). *Hypersonic and high temperature gas dynamics*. Aiaa.

Baranowski, L. (2013). Equations of motion of a spin-stabilized projectile for flight stability testing. *Journal of Theoretical and Applied Mechanics*, 51(1):235–246.

Benton, E. R. (1964). Supersonic magnus effect on a finned missile. *AIAA Journal*, 2(1):153–155.

Bergman, T. L. and Incropera, F. P. (2011). *Fundamentals of heat and mass transfer*. John Wiley & Sons.

Blake, W. B., Rosema, C., Doyle, J., Auman, L., and Underwood, M. (2011). Missile datcom, user's manual - 2011 revision. Technical report, U.S. Army Aviation & Missile Research, Development and Engineering Center.

Blosser, M. L. (2000). *Advanced metallic thermal protection systems for reusable launch vehicles*. PhD thesis, University of Virginia.

Böhrk, H. (2014). Transpiration cooling at hypersonic flight-aktiv on shefex ii. In *11th AIAA/American Soc. of Mechanical Engineers Joint Thermophysics and Heat Transfer Conference*, page 2676.

Buursink, J. (2005). *On the development of a cooled metallic thermal protection system for spacecraft*. PhD thesis, Delft University of Technology.

Buursink, J. and Sudmeijer, K. J. (2004). Experimental studies of an enhanced radiation cooling system. *Space*, pages 28–30.

Chapman, A. J. (1984). *Heat Transfer*. Macmillan Publishing Company.

Chapman, D. R., Wimbrow, W. R., and Kester, R. H. (1952). Experimental investigation of base pressure on blunt-trailing-edge wings at supersonic velocities. Technical report, National Advisory Committee for Aeronautics.

Cohen, N. B. (1961). *Boundary-Layer Similar Solutions and Correlation Equations for Laminar Heat-Transfer Distribution in Equilibrium Air at Velocities up to 41,100 Feet Per Second*. National Aeronautics and Space Administration.

Colwell, G. and Modlin, J. (1992). Heat pipe and surface mass transfer cooling of hypersonic vehicle structures. *Journal of thermophysics and heat transfer*, 6(3):492–499.

Cornelisse, J. W., Schoyer, H. F. R., and Wakker, K. F. (1979). *Rocket propulsion and spaceflight dynamics*. London: Pitman.

Curry, W. H. and Uselton, J. C. (1967). Some comments on the aerodynamic characteristics of the tomahawk sounding rocket. In *AIAA Sounding Rocket Vehicle Technology Specialist Conference*, pages 119–31.

Dormand, J. R. and Prince, P. J. (1980). A family of embedded runge-kutta formulae. *Journal of computational and applied mathematics*, 6(1):19–26.

Eggers, T., Dittrich, R., and Varvill, R. (2011). Numerical analysis of the skylon spaceplane in hypersonic flow. In *17th AIAA International Space Planes and Hypersonic Systems and Technologies Conference*, page 2298.

Etkin, B. (1972). *Dynamics of Atmospheric Flight*. John Wiley and Sons, Inc.

European Cooperation for Space Standardization (1998). Space engineering/verification. Technical report, ECSS-E-10-02A, 17 November.

Grillenberger, A. and Markgraf, M. (2011). Flight test results of a novel integrated gps receiver for sounding rockets. In *20th Symposium on European Rocket and Balloon Programmes and Related Research*, volume 700, pages 179–184.

Jacobson, I. D. and Yaggy, P. F. (1973). Magnus characteristics of arbitrary rotating bodies. Technical report, DTIC Document.

Kelly, H. N. and Blosser, M. L. (1992). Active cooling from the sixties to nasp. In *Current Technology for Thermal Protection Systems*, volume 1, pages 189–249.

Lord Mirostrain sensing (2017). *3DM®-CV5-10, Inertial Measurement Unit (IMU)*.

Lozino-Lozinsky, G. and Timoshenko, V. (1999). Lessons learned from the bor flight campaign. In *Aerothermodynamics for space vehicles*, volume 426, pages 675–683.

Martin, J. C. (1957). On magnus effects caused by the boundary-layer displacement thickness on bodies of revolution at small angles of attack. *J. Aeronaut. Sci*, 24(6):421–429.

Milton, J. E. (1974). Methods for calculating magnus forces on slender bodies of revolution. Technical report, FLORIDA UNIV EGLIN AFB GRADUATE ENGINEERING CENTER.

Mooij, E. (2015). *R-entry Systems (AE4870B) - Lecture Notes*. Delft University of Technology, Faculty of Aerospace Engineering.

Mulder, J., van Staveren, W., van der Vaart, J., and de Weerdt, E. (2013). *Flight Dynamics (AE3302) - Lecture Notes*. Delft University of Technology, Faculty of Aerospace Engineering.

Murphy, C. H. (1963). Free flight motion of symmetric missiles. Technical report, DTIC Document.

Murphy, C. H. (1981). Symmetric missile dynamic instabilities. *Journal of Guidance, Control, and Dynamics*, 4(5):464–471.

Naeije, M. C. and Mooij, E. (2016). *Lecture Notes AE4870-A: Rocket Motion*. Delft University of Technology.

National Oceanic and Atmospheric Administration (1976). *US standard atmosphere*. National Oceanic and Atmospheric Administration.

Nielsen, J. N. (1960). *Missile Aerodynamics*. Mc Graw Hill Book Co, Inc. New York.

Oh, S., Kim, S., Lee, D., Kim, S., and Ahn, S. (2009). Magnus measurements of spin-stabilized projectile using design of experiments. In *AIAA Atmospheric Flight Mechanics Conference*, page 5844.

Platou, A. S. (1965). Magnus characteristics of finned and nonfinned projectiles. *AIAA Journal*, 3(1):83–90.

Press, W. H. (2007). *Numerical recipes 3rd edition: The art of scientific computing*. Cambridge university press.

Quinn, R. D. and Gong, L. (2000). *A method for calculating transient surface temperatures and surface heating rates for high-speed aircraft*. National Aeronautics and Space Administration, Dryden Flight Research Center.

Rosema, C., Doyle, J., Auman, L., Underwood, M., and Blake, W. B. (2011). Missile datcom user's manual-2011 revision. Technical report, ARMY AVIATION AND MISSILE RESEARCH DEVELOPMENT ENG CTR REDSTONE ARSENAL AL SYSTEM SIMULATION AND DEVELOPMENT DIRECTORATE.

Siouris, G. M. (2004). *Missile guidance and control systems*. Springer Science & Business Media.

Sooy, T. J. and Schmidt, R. Z. (2005). Aerodynamic predictions, comparisons, and validations using missile datcom (97) and aeroprediction 98 (ap98). *Journal of spacecraft and rockets*, 42(2):257–265.

Stainless Structurals (2017). *Stainless Steel Structural Shapes: 304 and 304L Austenitic (Chromium-Nickel)*.

Sturek, W. B., Kayser, L. D., Nietubicz, C. J., Reklis, R. P., Opalka, K. O., and Dwyer, H. A. (1978). Computations of magnus effects for a yawed, spinning body of revolution. *AIAA Journal*, 16(7):687–692.

Sudmeijer, K. J. (2005). An enhanced radiation cooling system for re-entry vehicles, principle and mathematical modeling. In *AAAF 4th International Symposium on Atmospheric Reentry, Vehicles and Systems*.

Sudmeijer, K. J., Buursink, J., and Lopes, C. (2003). Enhanced radiation cooling system for metallic tps. In *Hot Structures and Thermal Protection Systems for Space Vehicles*, volume 521, pages 259–266.

Tauber, M. E. (1989). A review of high-speed, convective, heat-transfer computation methods. Technical report, ASA Ames Research Center.

Tumino, G. (2003). European development and qualification status and challenges in hot structures and thermal protection systems for space transportation concepts. In *Hot Structures and Thermal Protection Systems for Space Vehicles*, volume 521, pages 39–43.

Vallado, D. A. (2001). *Fundamentals of astrodynamics and applications*, volume 12. Springer Science & Business Media.

Volckaert, M. (2007). The re-entry module of sta and its application to a deimos sample return mission. Master's thesis, Delft University of Technology.

Wagner, W., Saul, A., and Pruss, A. (1994). International equations for the pressure along the melting and along the sublimation curve of ordinary water substance. *Journal of Physical and Chemical Reference Data*, 23(3):515–527.

Weihs, H., Turner, J., and Longo, J. M. (2008). Key experiments within the shefex ii mission. In *59th International Astronautical Congress 2008 (IAC 2008)*, volume 11, page 7499.

Zipfel, P. H. (2000). *Modeling and simulation of aerospace vehicle dynamics*. Aiaa.

A

T-Minus Dart characteristics

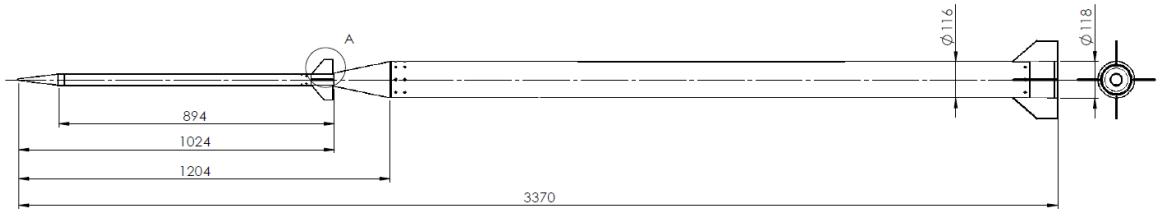

Figure A.1: T-Minus Dart boosted configuration (dimensions are in millimetres)

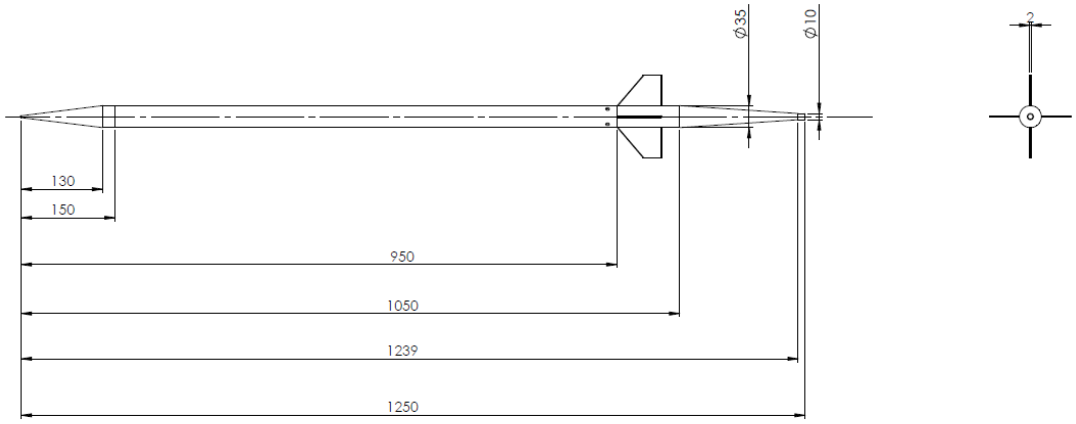

Figure A.2: T-Minus Dart coasting configuration (dimensions are in millimetres)

B

Missile Datcom input files

B.1. Input file for the T-Minus DART boosted configuration

```
CASEID Dart
* Use meters and degrees in this simulation
* Data for simulation of dart
DIM M
DERIV RAD
*
$FLTCON NMACH=14.,$
$FLTCON MACH=0.1, 0.2, 0.3, 0.4, 0.5, 0.6, 0.8, 1.0, 1.2, 1.5, 2.0,
3.0, 4.0, 5.0,$
$FLTCON REN=5000000.,11000000.,16000000.,22000000.,27000000.,32000000.,
50000000.,60000000.,68000000.,75000000.,80000000.,70000000.,
40000000.,20000000.,$
$FLTCON NALPHA=9.,$
$FLTCON ALPHA=-15.0,-10.0,-5.0,-2.5,0.0,2.5,5.0,10.0,15.0,$
$FLTCON BETA=0.,$
*
* Reference area
*
$REFQ XCG=1.2, SREF=0.010568, LREF=0.116, LATREF=0.116, RHR=20.00,$
$REFQ BLAYER = NATURAL,$
*
* Body:
$AXIBOD XO=0.0, NX=5.0, $
$AXIBOD X=0.0,0.013,1.025,1.205,3.158, $
$AXIBOD R=0.0,0.0175,0.0175,0.058,0.058, $
$AXIBOD LNOSE = 0.13,$
$AXIBOD DNOSE = 0.035,$
$AXIBOD LCENTR = 3.028,$
$AXIBOD DCENTR = 0.116,$
* The Canards
$FINSET1 SECTYP=0.,NPANEL=4.00,$
$FINSET1 XLE=0.820,0.860$
$FINSET1 SSPAN=0.0175,0.0655,$
$FINSET1 CHORD=0.070,0.03,$
$FINSET1 PHIF=0.0,90.0,180.0,270.0,$
$FINSET1 ZUPPER =0.028, 0.06,$
$FINSET1 LMAXU = 0.05, 0.13,$
$FINSET1 LFLATU = 0.94, 0.86,$
```

```
*The Fins
$FINSET2 SECTYP=0.,NPANEL=4.00,$
$FINSET2 XLE=2.698,2.848$
$FINSET2 SSPAN=0.058,0.119,$
$FINSET2 CHORD=0.33,0.180,$
$FINSET2 PHIF=0.0,90.0,180.0,270.0,$
$FINSET2 ZUPPER =0.015, 0.027,$
$FINSET2 LMAXU = 0.03, 0.05,$
$FINSET2 LFLATU = 0.96, 0.94,$
*
* Generate variables
*
PART
DAMP
PRESSURES
SOSE
SPIN
BUILD
PLOT
SAVE
NEXT CASE
```

B.2. Input file for the T-Minus DART coasting configuration

```
CASEID Dart
* Use meters and degrees in this simulation
* Data for simulation of dart
DIM M
DERIV RAD
*
$FLTCON NMACH=14.,$
$FLTCON MACH=0.1, 0.2, 0.3, 0.4, 0.5, 0.6, 0.8, 1.0, 1.2, 1.5, 2.0, 3.0, 4.0, 5.0,$
$FLTCON REN=5000000.,11000000.,16000000.,22000000.,27000000.,32000000.,
50000000.,60000000.,68000000.,75000000.,80000000.,70000000.,
40000000.,20000000.,$
$FLTCON NALPHA=9.,$
$FLTCON ALPHA=-15.0,-10.0,-5.0,-2.5,0.0,2.5,5.0,10.0,15.0,$
$FLTCON BETA=0.,$
*
* Reference area
*
$REFQ XCG=0.20, SREF=0.000962, LREF=0.035, LATREF=0.035, RHR=20.00,$
$REFQ BLAYER = TURB,$
*
* Body:
$AXIBOD X0=0.0, $
$AXIBOD TNOSE=0.00,$
$AXIBOD LNOSE=0.130,$
$AXIBOD DNOSE=0.035,$
$AXIBOD BNOSE = 0.,$
$AXIBOD LCENTR = 0.920,$
$AXIBOD DCENTR = 0.0.35,$
$AXIBOD TAFT = 0.,$
$AXIBOD LAFT = 0.200,$
$AXIBOD DAFT = 0.010,$
* The Fins
$FINSET1 SECTYP=0.,NPANEL=4.00,$
$FINSET1 XLE=0.820,0.860$
$FINSET1 SSPAN=0.0175,0.0655,$
$FINSET1 CHORD=0.070,0.03,$
$FINSET1 PHIF=0.0,90.0,180.0,270.0,$
$FINSET1 ZUPPER =0.028, 0.06,$
$FINSET1 LMAXU = 0.05, 0.13,$
$FINSET1 LFLATU = 0.94, 0.86,$
*
* Generate variables
*
PART
SPIN
DAMP
HYPER
PLOT
SAVE
NEXT CASE
```

B.3. Input file for the VS40

```
CASEID VS40-PT02
* Data for simulation of VS40
DIM M
DERIV RAD
*
$FLTCON NMACH=14.,$
$FLTCON MACH=0.1, 0.2, 0.3, 0.4, 0.5, 0.6, 0.8, 1.0, 1.2, 1.5, 2.0, 3.0, 4.0, 5.0,$
$FLTCON REN=5000000.,11000000.,16000000.,22000000.,27000000.,32000000.,
50000000.,60000000.,68000000.,75000000.,80000000.,70000000.,
40000000.,20000000.,$
$FLTCON NALPHA=9.,$
$FLTCON ALPHA=-15.0,-10.0,-5.0,-2.5,0.0,2.5,5.0,10.0,15.0,$
$FLTCON BETA=0.,$
*
* Reference area
*
$REFQ XCG=3.8, SREF=0.79643, LREF=1.007, LATREF=1.007,$
*
* Body:
$AXIBOD X0=0.0, $
$AXIBOD NX = 10.,$
$AXIBOD X = 0.0, 0.00263, 0.01044, 0.02314, 0.04031, 0.06133,
0.08548, 0.11192, 1.4467, 9.5206,$
$AXIBOD R = 0.0, 0.0287, 0.05517, 0.08034, 0.10271, 0.12149,
0.13605, 0.14585, 0.5035, 0.5035,$
$AXIBOD LNOSE = 1.4467,$
$AXIBOD DNOSE = 1.007,$
$AXIBOD LCENTR = 8.0739,$
$AXIBOD DCENTR = 1.007,$
*
*
*The Fins
*
$FINSET1 SECTYP=0.,NPANEL=4.00,$
$FINSET1 XLE=8.26930,8.26930,$
$FINSET1 SSPAN=0.5035,1.4035,$
$FINSET1 CHORD=1.25130,1.25130,$
$FINSET1 LER=0.0050,0.0050,$
$FINSET1 ZUPPER = 0.0385,0.0385,$
$FINSET1 LMAXU = 0.34,0.34,$
$FINSET1 LFLATU = 0.65,0.65,$
$DEFLCT DELTA1 = -0.8, -0.8, -0.8, -0.8,$
*
*Generate variables
DAMP
PART
PRESSURES
SOSE
SPIN
BUILD
PLOT
SAVE
NEXT CASE
```

C

Experiment components overview

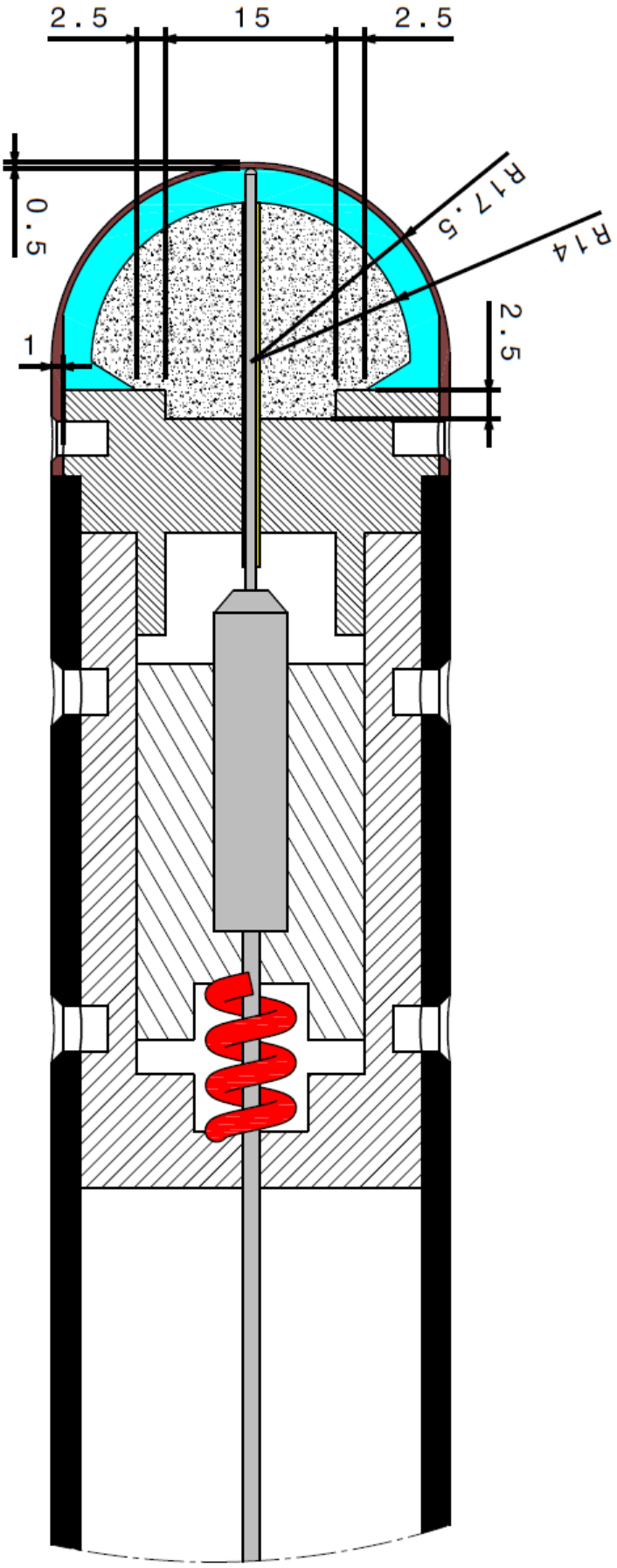

Figure C.1: Experiment overview with thermocouple, all dimensions in mm

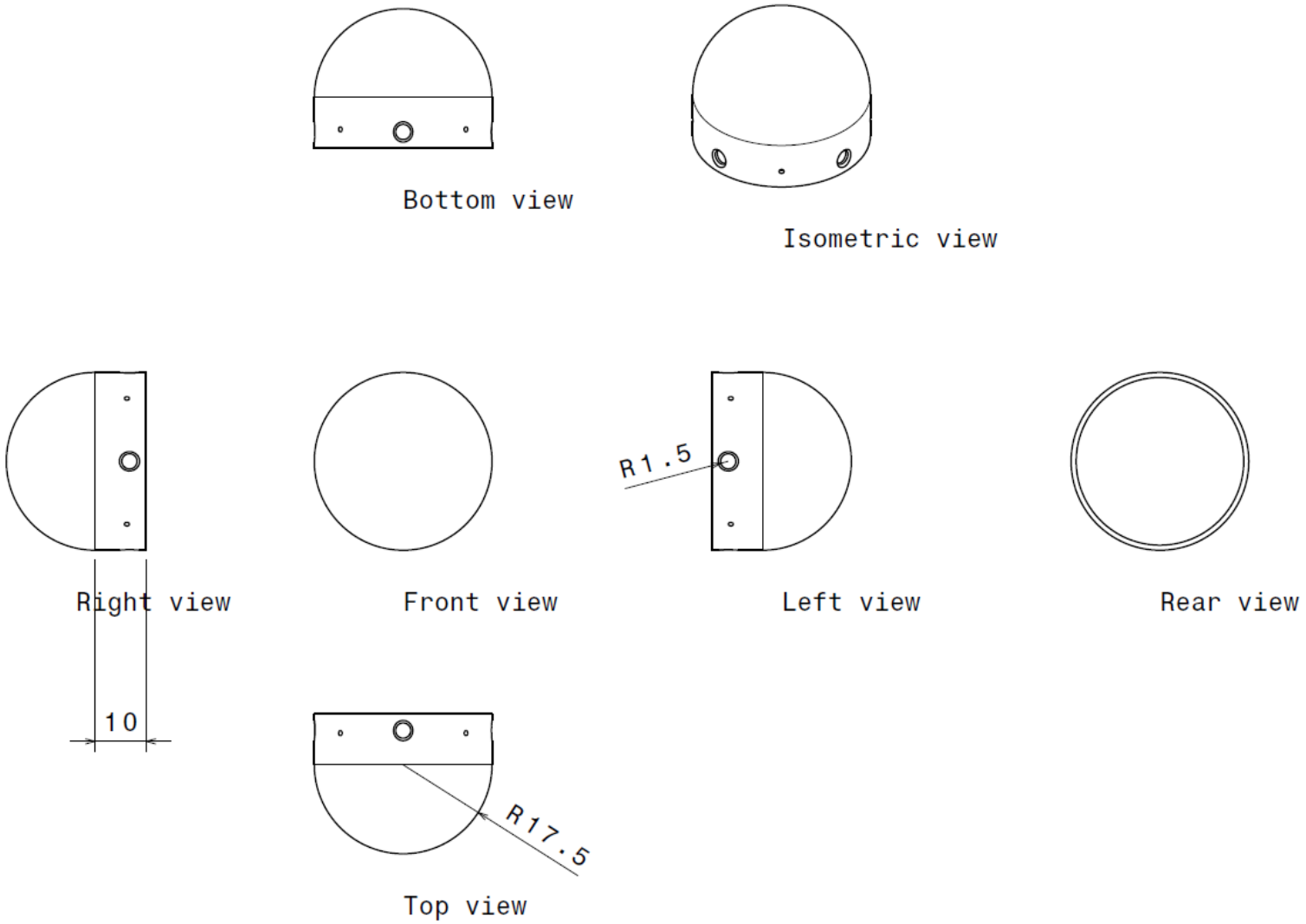

Figure C.2: Outer shell, all dimensions in mm

Figure C.3: Insulation sphere, all dimensions in mm

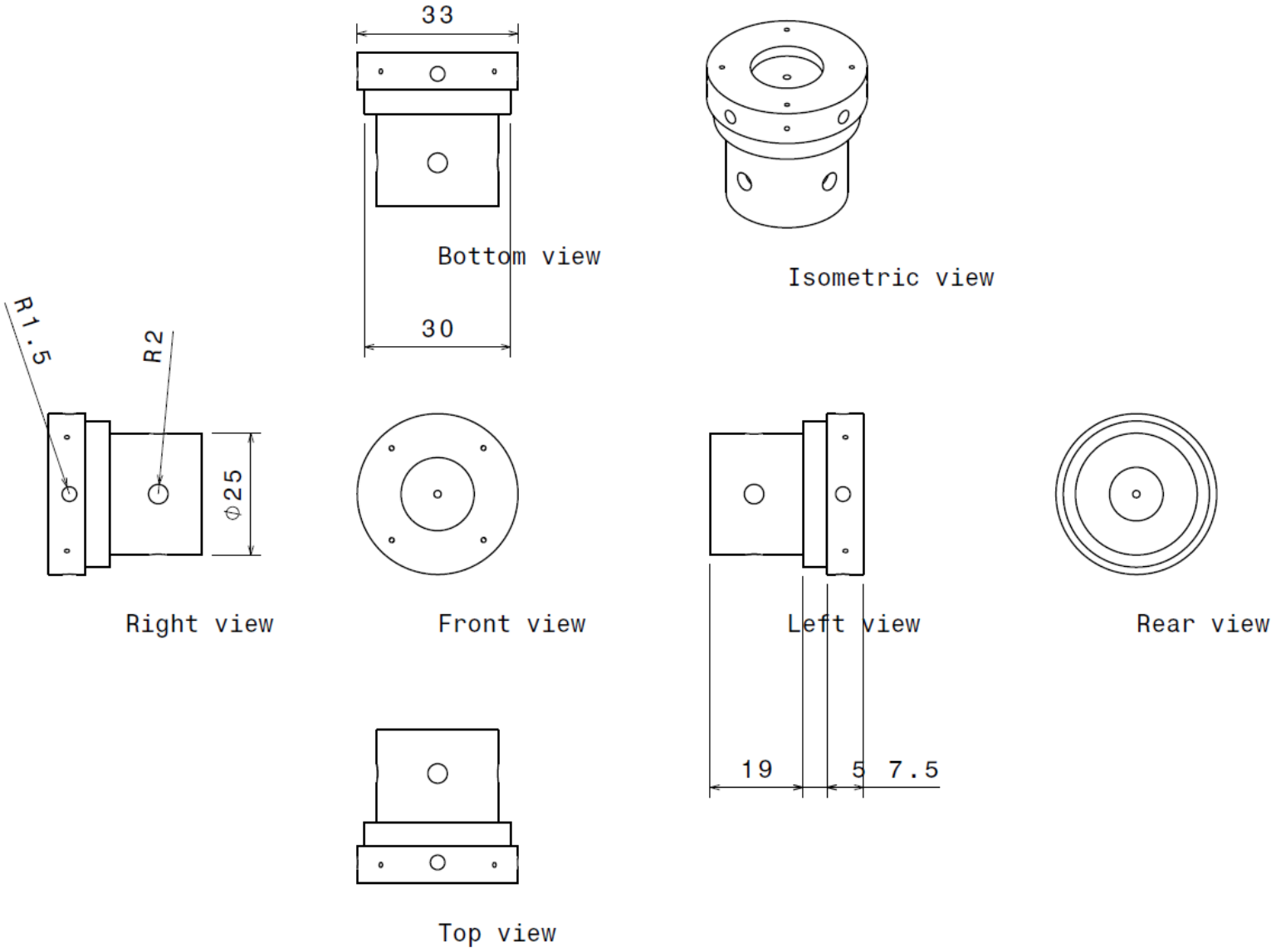

Figure C.4: Bracket 1, all dimensions in mm

Figure C.5: Bracket 2, all dimensions in mm